Effect of Preheating Condition on Strength of AA6060 Aluminium Alloy for Extrusion

Cheng Meng

A thesis submitted in partial fulfilment of the

Master of Engineering

School of Engineering

Auckland University of Technology

March 2010

ABSTRACT

Fletcher Aluminium is a New Zealand company that manufactures aluminium extrusions for the building market. Their extrusion process involves using a hydraulic ram to force heated raw supplied material, in the form of large diameter cylindrical logs, through a die land that is the desired product shape. The final quality of the extruded product is influenced by the extrusion temperature, ram pressure and extrusion speed.

The speed of extrusion at Fletcher Aluminium is limited by the extrusion ram pressure because the extrusion machine is operating at the pressure limit of the compressor. Currently the company requires an increase in the extrusion speed, while maintaining quality requirements where these improvements are desired without upgrading the compressor. The press pressure is required to overcome friction and the flow stress of the billet, which is dependent on the precipitates and solutes conditions and their strengthening effects in the billet. However, the preheating temperature and extrusion speeds need to be sufficiently low enough to avoid hot tearing.

This research starts to increase the ram speed by decreasing the Mg_2Si content for precipitation strengthening. Heat treatment may be used to dissolve Mg_2Si content by billet preheat to a temperature at or exceeds solvus temperature (T_{Solvus}). However, a higher (than T_{Solvus}) billet temperature may have two conflicting effects. First, a higher temperature in general reduces the flow stress thus lowering the required pressure. On the other hand, at temperature higher than T_{solvus}, Mg_2Si should completely dissolve, resulting in solid solution strengthening thus increasing the flow stress.

The objective of the study is to quantify the strengthening contributions from solute atoms (Mg / Si) and precipitates (Mg_2Si) on the as-received and heat treated test samples using room temperature mechanical testing and phase diagram analysis. The selected heat treatment conditions fully enclose the preheating temperature and time range currently used in Fletcher Aluminium production. Simulations of the extrusion were conducted by hot compression testing (Gleeble test), to measure the combination of strengthening effects during deformation at elevated temperatures.

The room temperature tests have shown that hardness, yield strength (YS) and ultimate tensile strength (UTS) are minimised at approximately 405°C. The minimum point is shown to be caused by the combination of strengthening and softening due to solid solution and precipitation strengthening. The higher values of hardness, YS and UTS at lower and higher preheating temperatures are mainly due to precipitation and solution strengthening respectively. The findings show that, the solution of Mg_2Si gradually increases as the temperature increases at temperatures exceeding 405°C.

Hardness, YS and UTS were compared in order to determine the correlation between each mechanical property. A correlation exists, but it is not simple to translate between each mechanical property. The relationship between hardness and stress observed for 8% permanent strain was also investigated; there was no improvement in correlation.

The elevated temperature tests show that initial flow stress and peak flow stress reduces linearly with temperature increases, which means higher testing temperature results lower precipitation and solid solution strengthening effects. Additionally, the constants of the Gleeble – Holomon equation were numerically calculated and are similar to published values. The Gleeble – Holomon equation was combined with Felthams equation in order to provide a relationship between extrusion velocity and extrusion temperature.

ACKNOWLEDGEMENTS

This work has been carried out at the Auckland University of Technology, Department of Mechanical Engineering in collaboration with Fletcher Aluminium. I would to take this opportunity to thank the following individuals for their contribution towards the success of this project.

Firstly, I would like to thank my supervisor, Dr. Zhan Chen, who gave me patient guidance throughout the whole project process. His enthusiastic and professional attitude gave me a big motivation to carry out this project. Special acknowledgements go to the second supervisor Dr. Timotius Pasang. The author is grateful for their help during this research.

I also would like to acknowledge Fletcher Aluminium for their contributions to this work over the past years. I would like to thank Mr. Sen Chen, Product Development Manager and Mr. Bill Hayward, Metallurgist at Fletcher Aluminium for their expertise and assistance to complete the experiment for the project.

I would like to Thank Heat Treatment New Zealand Limited for allowing the use of their Vickers micro-hardness tester.

I would also like to thank Ross Reichardt, Mark Masterton and Bradley Scott who provided expertise and assistance required to complete the experiments for the project.

Finally, I would like to thank my parents for their encouragement and much needed emotional support. Without whose support this report would not have been possible.

CONTENTS

FIGURES

TABLES

NOMENCLATURE

σ_E	=	Engineering strength, MPa
σ_T	=	True strength, MPa
ε_E	=	Engineering strain
ε_T	=	True strain
n	=	Strain hardening exponent
K	=	Strength coefficient
r	=	Strain hardening exponent
V_{ram}	=	Ram speed, m/min
V_{exit}	=	Extrusion speed, m/min
P	=	Extrusion pressure, kN/m^2
$\dot{\varepsilon}$	=	Strain rate, s^{-1}
Q	=	Apparent activation energy for deformation, KJ/mol
R	=	Universal gas constant, 8.314 KJ/mol·K
T	=	Temperature, K
A, K	=	Material constants, s^{-1}
YS, σ_{YS}	=	Yield strength, MPa
UTS, σ_{UTS}	=	Ultimate tensile strength, MPa
YS_t	=	Total yield strength
σ_o	=	Yield strength of pure aluminium, MPa
σ_{Si}	=	Yield strength of eutectic Si particles, MPa
σ_{Fe}	=	Yield strength of eutectic Fe phase particles, MPa
$\sigma_{SS,Si}$	=	Yield strength of Si in solid solution, MPa
$\sigma_{SS,Mg}$	=	Yield strength of Mg in solid solution, MPa
$\sigma_{PPT,Si}$	=	Yield strength of pure aluminium, MPa
$\sigma_{PPT,Mg-Si}$	=	Yield strength of Mg-Si precipitates, MPa
σ_i	=	Intrinsic strength, MPa

σ_{SSS}	=	Yield strength of solid solution strengthening, MPa
σ_{PPT}	=	Yield strength of precipitation strengthening, MPa
Z	=	Temperature – compensated strain rate

ATTESTATION OF AUTHORSHIP

I hereby declare that this submission is my own work and that, to the best of my knowledge and belief, it contains no material previously published or written by another person (except where explicitly defined in the acknowledgements), nor material which to a substantial extent has been submitted for the award of any other degree or diploma of a university or other institution of higher learning.

Name: _____

Date: _____

Chapter 1 Introduction of Extrusion Process

In this chapter the general features of aluminium extrusion and the relevant processes are introduced first. The chapter then describes the limiting feature in an extrusion manufacturing in plant before outlining the objective of this research.

1.1 Aluminium Extrusion

Aluminium extrusion is the major manufacturing activity of Fletcher Aluminium, a company located in Auckland, New Zealand. Fletcher Aluminium manufactures extrusion products for both Fletcher's building business and for the NZ general commercial and domestic building market.

Extrusion was invented in 1886, by Hall and Heroult [1]. It is a forming operation that uses a hydraulic ram to force heated raw supplied material, in the form of large diameter cylindrical logs, through a die land that is the desired product shape. The quality of the extruded product is influenced by the extrusion temperature, ram pressure and extrusion speed. A schematic representation of the extrusion process is shown in Figure **1.1**.

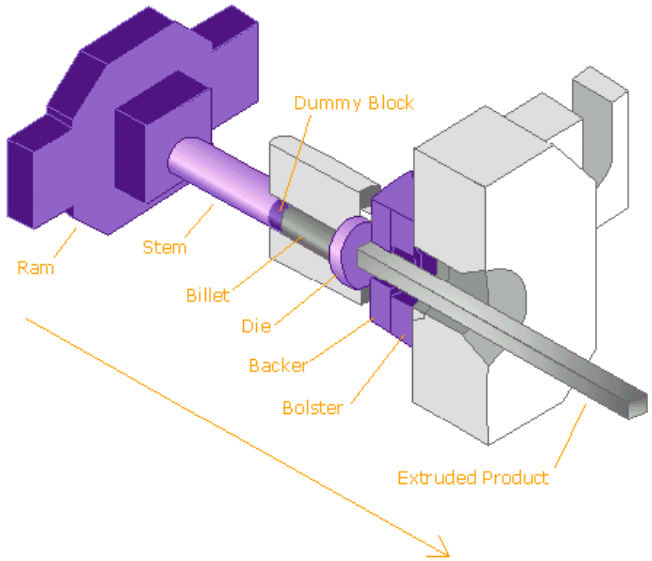

Figure 1.1: Representation of an extrusion process [2]

Aluminium AA6xxx heat treatable series alloys are the most widely used for the production of extruded sections. Today more than 80% of the manufactured extruded

aluminium products used worldwide are based on the AA6xxx series alloys due to its high extrudability [3, 4]. Indeed, almost 90% of the production at Fletcher Aluminium consists of AA6060 alloy. These alloys are heat treatable aluminium alloys that find their greatest use in applications requiring medium to high strength, very good hot formability, excellent corrosion resistance and good surface finish. Several typical extrusion applications include aerospace, automotive transportation, building, architectural, furniture, shipping, and electrical components. Foremost, the largest single product group consumer is the building industry.

The entire Fletcher Aluminium extrusion production process is presented schematically in Figure 1.2 which involves many production steps that ensure the extruded product is the correct shape, strong, aesthetically pleasing and protected from corrosion.

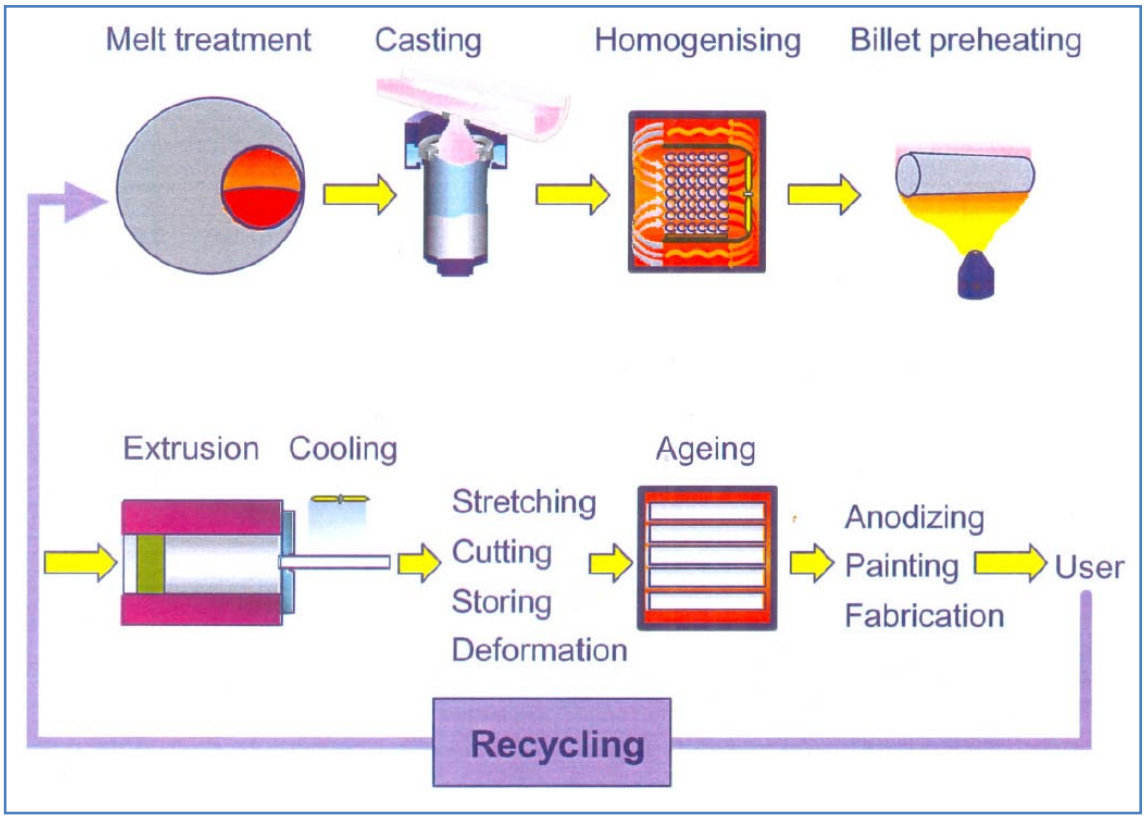

Figure 1.2: Process of Extrusion [2]

The AA6060 billet is produced using the direct-chill (DC) casting system where Aluminium, Magnesium, Silicon and other elements are combined, melted, poured into a mould and solidified. The billet is homogenised in a furnace, then forced air cooled using large electrical fans. Homogenised billets are then provided to the Fletcher Aluminium manufacturing process, where they are reheated in the gas burner heating furnace. The hot billets are then inserted into the container of the extrusion compressor

and pressed through a die with a shaped opening. The extruded profiles are stretched, cut, then stacked properly for the final thermal treatment of artificial age-hardening. Extrusions are then provided with anti-rust treatment, packaged, and shipped to customers.

At each production step, there are complicated, temperature dependent, thermo-mechanical, metallurgical and chemical events which each affect the production rate and extrusion quality. The following sections discuss these effects for direct chill casting, billet homogenization, billet pre-heating and extrusion. A typical temperature and time profile of AA6xxx extrusion from casting to ageing is presented in Figure **1.3**.

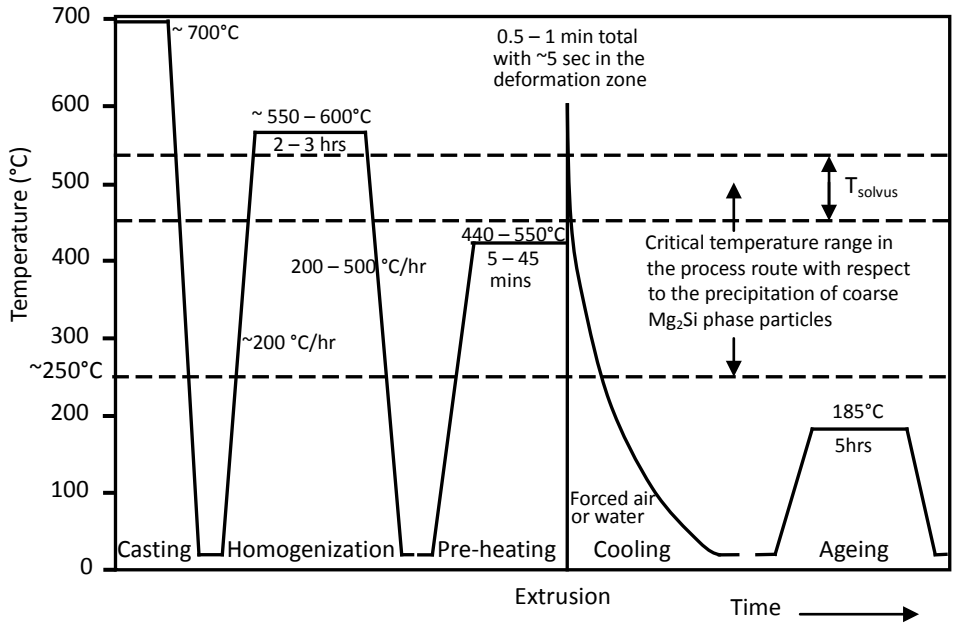

Figure 1.3: Typical temperature/time profile for the production of AA6xxx extrusions [redrawn from Schikorra's diagram [2])

1.2 AA6xxx Alloys and Supplied AA6060 Billet Materials

AA6xxx is an Aluminium/Magnesium/Silicon alloy series which is commonly used for heat treatable aluminium extrusions. In general, this group of alloys can be extruded with ease, are tough and durable after heat treatment, and are resistant to corrosion after anodising.

Magnesium and silicon are the main alloying elements and combine to form the stochiometric compound, magnesium silicide (Mg_2Si) when the weight ratio of magnesium to silicon is 1.73:1. The Mg_2Si makes AA6xxx series alloys heat treatable

and capable of achieving medium strength [5, 6]. The strength of the alloy is dependent on many aspects such as the role of Mg_2Si precipitates, the amount of Mg and Si in solid solution, and the size and distribution of Mg_2Si precipitate particles [7]. The chemical composition of AA6060 is provided in Table 1.1.

Table 1.1: AA6060 alloy chemical composition limits (Weight percent) [5]

AA No.	Si	Fe	Cu	Mn	Mg	Cr	Zn	Ti
6060	0.3-0.6	0.1-0.3	0.1	0.1	0.35-0.6	0.05	0.15	0.1

Magnesium and Silicon elements are partly dissolved in the primary α-Al matrix, and to a certain extent are present in the form of intermetallic phases. A range of different intermetallic phases may form during the cooling period, depending on alloy composition and cooling method. Relative volume fraction, chemical composition and morphology of structural constituents exert significant influence on their useful properties [8].

The weight percentage of Mg_2Si is determinable from the chemical composition of the material using the stoichiometric chemical equation, where a summary of chemical compositions for supplied materials is presented in Table **4.1** (page 43). The supplied AA6060 materials possess 0.36% Mg, which can be substituted into Eq. 1.1 below [6].

$$\%Si \text{ required for } Mg_2Si = Mg / 1.73 \qquad (1.1)$$

$$\%Si \text{ required for } Mg_2Si = 0.36\% / 1.73 = 0.21\%$$

Consequently, stoichiometric Mg_2Si for the supplied alloys exists at 0.21% Si. However, the as-received alloys provided by the suppliers contain ~0.52% Si which is a significantly larger proportion of Si than stoichiometric requirement of 0.21% Si. The excess quantity of Si will cause iron and manganese to combine with a portion of the silicon and aluminium to form Al(FeMn)Si phase. The formation of Al(FeMn)Si will then reduce the amount of silicon available to form Mg_2Si. Analysis of the chemical equation produces Eq. 1.2 below [6].

$$\%Si \text{ available for } Mg_2Si = \%Si - 1/4(Fe+Mn) \qquad (1.2)$$

$$\%Si \text{ available for } Mg_2Si = 0.52\% - 1/4\,(0.18\% + 0.06\%) = 0.46\%$$

$$\%Si\ excess = 0.46\% - 0.21\% = 0.23\%$$

Consequently, the as-received alloys have ~ 0.23% excess silicon available to react and form Mg_2Si to improve the hardening, and it will be explained in Section 2.2.

1.3 Direct-Chill (DC) Casting Process

The melted combination of elements is solidified into a log to allow transportation of the raw material. The material must be rapidly cooled to give uniformity in composition across the billet diameter and to give small uniformly distributed micro-constituents. Constancy of chemical composition and microstructure is important to ensure properly heat treated extrusions, since they will affect hot workability and mechanical properties.

The majority of the extrudable AA6xxx aluminium alloy large-scale ingots are produced using the direct-chill (DC) casting method [5]. A schematic diagram of the direct-chill (DC) casting process is shown in Figure **1.4**.

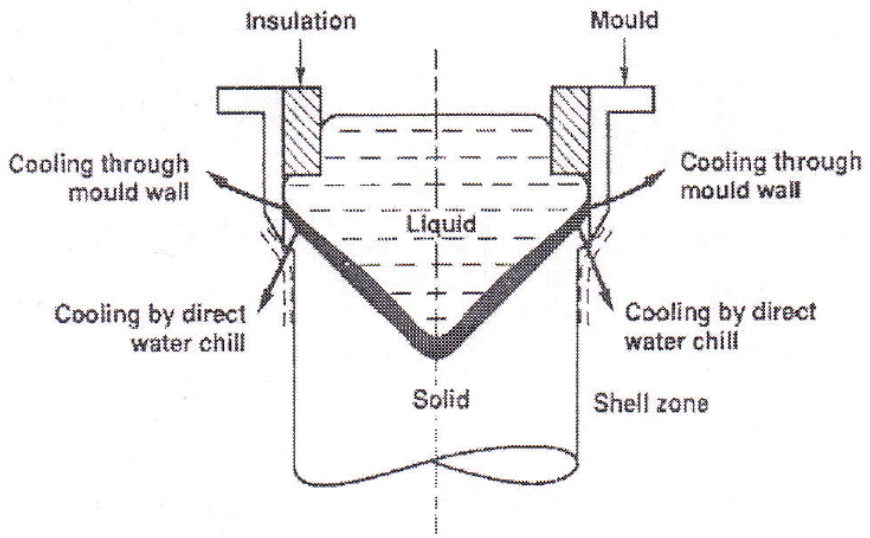

Figure 1.4: A typical illustrated casting process [9]

The DC casting process involves feeding molten metal through a bottomless water-cooled mould; a solid shell forms around the outer surface, which becomes sufficiently thick that the casting takes the shape of the mould and acquires sufficient mechanical strength to support the molten core in the centre. The molten aluminium is then cooled in such a way that the outside solidifies before the metal exits the mould.

1.4 Homogenization Process

Homogenization is a heat treatment process used to modify the microstructure of the cast ingot in order to improve hot workability and the mechanical properties of the extrusions. This process involves heating the billet to between 550°C and 600°C for a soak time of two hours as shown in Figure **1.5**. The purpose of homogenization is to, as much as possible, dissolve the soluble constituents and to disperse them uniformly throughout the cross section. Homogenized billets can be extruded faster than as-cast billet, produce a superior surface finish and higher tensile properties.

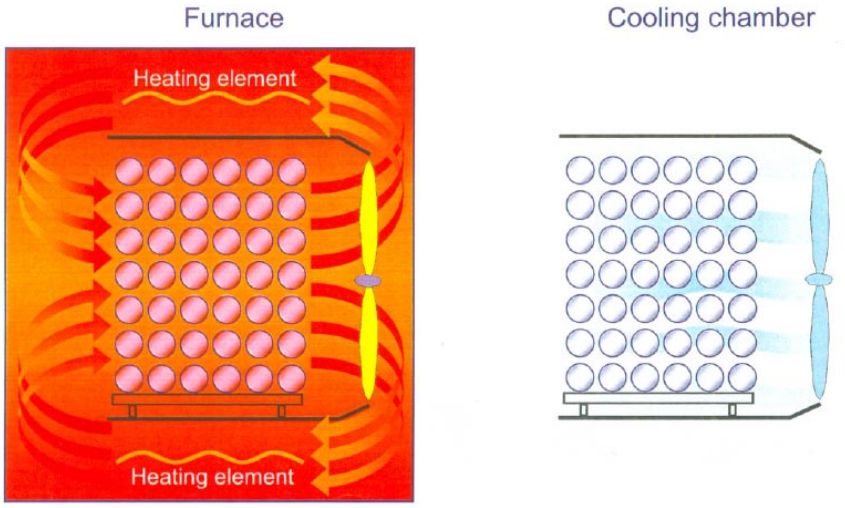

Figure 1.5: The homogenization process at aluminium smelter [2]

There are two mechanisms which influence high temperature deformation within AA6xxx aluminium alloys. The first mechanism concerns the soluble Mg_2Si phase where the ability of this phase to get into solution has a large effect on the deformation properties during extrusion such as softening the material and avoiding eutectic melting reactions. The second mechanism is the presence of the AlFeSi intermetallic phase whcih restricts hot workability when presents as hard and brittle plate-like precipitates β–AlFeSi. Therefore for AA6xxx series aluminium alloys, homogenization serves two purposes: (a) It evens out micro-segregation of the fast diffusing species Mg and Si so ensuring solution of coarse Mg_2Si precipitates. (b) It modifies the structure of the AlFeSi particles which are an insoluble phase in these alloys. This change of morphology is represented in Figure 1.6 [5].

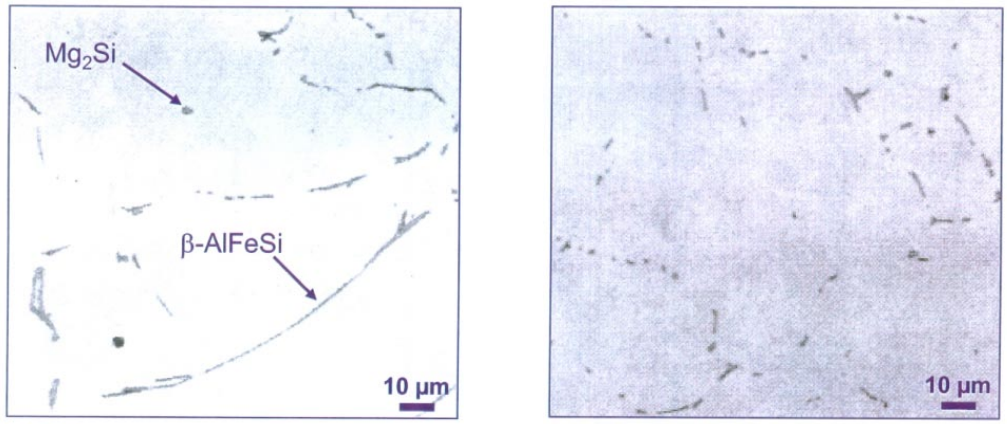

Figure 1.6: Microstructure in an AA6060 Alloy, (a) as-cast state, (b) after homogenization [5]

The Fe-bearing intermetallic particles, including β-Al_5FeSi (β) and α-Al(Fe,Mn)Si (α) are typically found in AA6xxx alloys and significantly influence formability. The brittle plate-like monoclinic β phase is associated to poor hot workability. This unfavourable effect can be improved by performing a long homogenization treatment at high temperature, by which the β phase transforms to the more rounded, metastable, and cubic α phase.

1.5 Preheating Process

Figure **1.7** shows the billet being loaded into the gas fired furnace for preheating. The preheating process softens the billet material by reheating billets to the extrusion temperature (typically 400°C). The temperature is monitored by a thermocouple probe where the preheating process is currently 40 minutes long and the preheat temperature setting varies between 380 – 450°C depending on the profile to be extruded.

Figure 1.7: Loading billet to preheat furnace [10]

The main purpose of preheating is to lower the strength and to increase the plasticity of the billet before extrusion. Preheating is also used to transform any remaining β-AlFeSi into α-AlFeSi and to further dissolve remaining Mg_2Si after the homogenization process.

1.6 Extrusion Process

Immediately after preheating, the billet is then pushed into the container. Figure **1.8** shows a typical billet being loaded on to the extrusion press. The die is located at one end of the container and the metal to be extruded is pushed towards it, hence moving relative to the container. As the material flows through the die, the temperature of the metal increases and stabilizes. This process is typically conducted at a relatively high temperature, which could rise up to 565°C depending on the preheating temperature and extrusion speed. The lower flow stress at elevated temperature permits larger section reductions to be achieved, lowering the power requirements and processing times. Hot tearing, which is melting of precipitates on the surface of the extrusion, can occur when the temperature exceeds 610°C [10]. Therefore, the exit temperature must always exceed the solvus temperature and be well below the liquidus temperature.

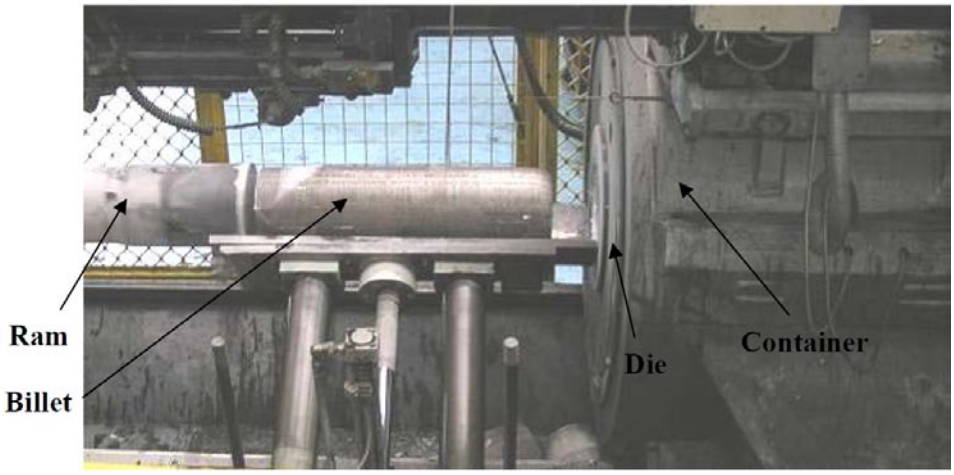

Figure 1.8: Billet being loaded on to the extrusion press [10]

Figure 1.9 shows a typical profile extrusion process at the die exit (after extrusion), and its subsequent air cooling to prevent the precipitation of Mg_2Si particles after extrusion. The cross sectional shape is achieved at this point although the material is ductile and prone to rust.

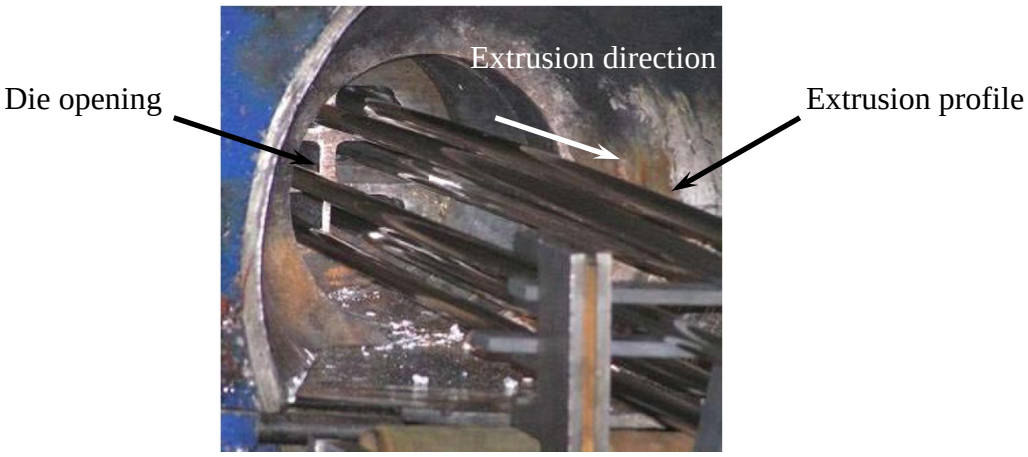

Figure 1.9: Metal flowing (extrudate) at the exit door [10]

The speed that the extrusion product exits the die is dependent on the rate that the ram moves forward. Figure **1.10** is a smoothed pressure-displacement trace that is typical of all aluminium alloys within which, Sheppard identifies six principal extrusion stages [11]. Region A shows that the load in extrusion initially increases very rapidly as the billet upsets to fit the container. There is a further increase in pressure (region B) until the extrusion begins. In this process, the structure is heterogeneous with progressively increasing dislocation and subgrain density mainly concentrated in the die region. In C, peak pressure region, a peak appears because a greater dislocation density is required to reach steady state extrusion than is required to maintain it [11].

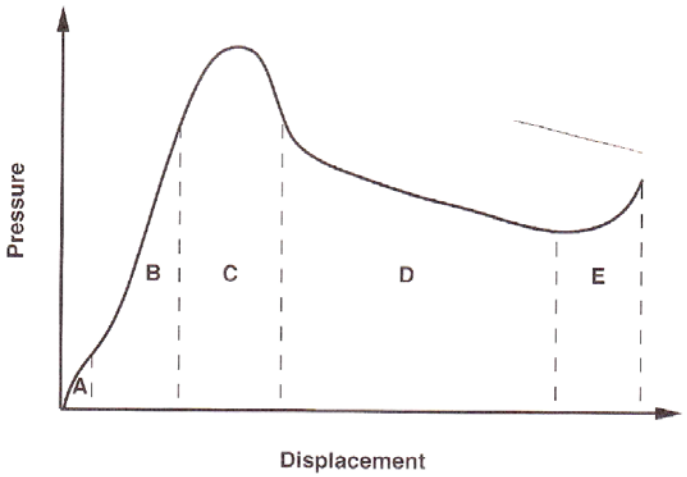

Figure 1.10: Evolution of the load during extrusion [11]

After the peak pressure has been reached, the extrusion pressure falls as the billet length decreases. In the extrusion, the process is characterised by the absence of friction between the billet surface and the container. The macrostructural and microstructural changes are complex and contain second phases, which include precipitates and solutes that hinder dislocation movement.

1.7 Fletcher Aluminium Extrusion & Limiting Press Pressure

Many production steps are required to extrude aluminium alloys, from the initial raw material in the form of large diameter cylindrical logs, to the final products of differing complexity, strength and surface finish. There are complex thermo-mechanical, metallurgical or chemical events and phenomena in each step where understanding these phenomena in detail allows greater control of the different parameters for high production rate and extrusion quality. Figure **1.11** illustrates the essential principle of the direct extrusion process.

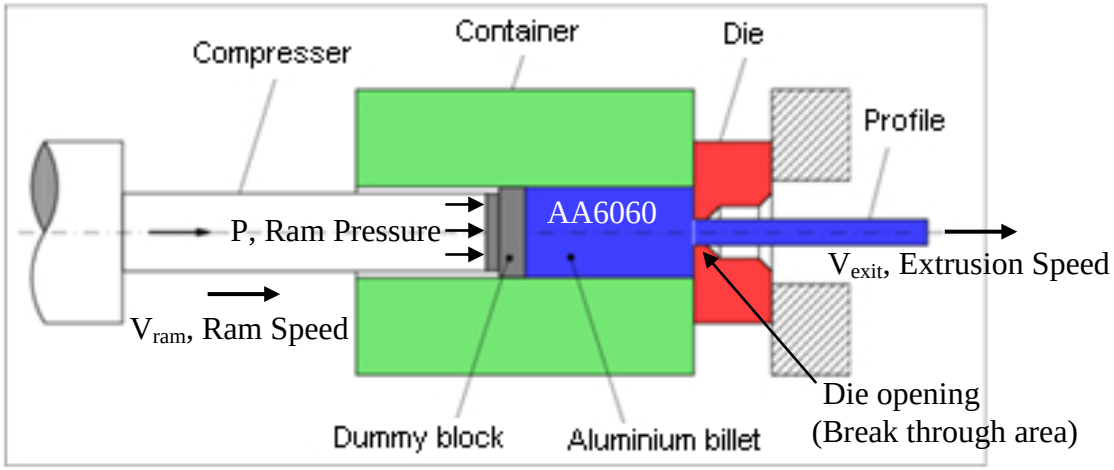

Figure 1.11: Schematic illustration of direct extrusion

Operating parameters such as ram speed, ram pressure and preheat temperature are controlled by manufacturers. Typical operating parameters were collected from many extrusion runs at Fletcher Aluminium and are shown in Table **1.2**. The details of the extrusion processing parameters are also presented in Appendix K.

Table 1.2: Data Collected at Fletcher Aluminium for AA6060 Extrusion Run

Parameter	Value
Material	AA6060 (Hydro & RTA)
Diameter of Billet	202 mm
Billet Cross Section Area	32031 mm^2
Extrude Cross Section Area	594 mm^2
Compression Ratio	53.92
Preheat Temperature	380 ~ 450 ºC
Preheat Time	40 mins
Average Extrusion Speed	20 m/min
Average Ram Speed	3 m/min

Under the present operating conditions, the limiting factor for productivity in the current extrusion process in Fletcher Aluminium is the capacity (maximum force) of the extrusion press. Ideally, if capacity of the press is not limited, when the extrusion starts by pressing the billet through the die opening, the pressure rapidly increases to a break through (high) pressure; therefore allowing extrusion at a preset speed. However, if insufficient ram force is provided, the ram speed will reduce.

Figure 1.12 shows the pressure – time characteristic curve for the Fletcher extrusion cycle. The ram speed is observed to reduce suddenly as the ram pressure approaches peak pressure where the limiting pressure value is initially reached, and the extrusion speed must then remain low for a significant period of time. In this case, the maximum press force (peak pressure) cannot be attained due to a lack of sufficient power of the compressor, where this insufficient capacity of the extruder can shorten the die and machine life.

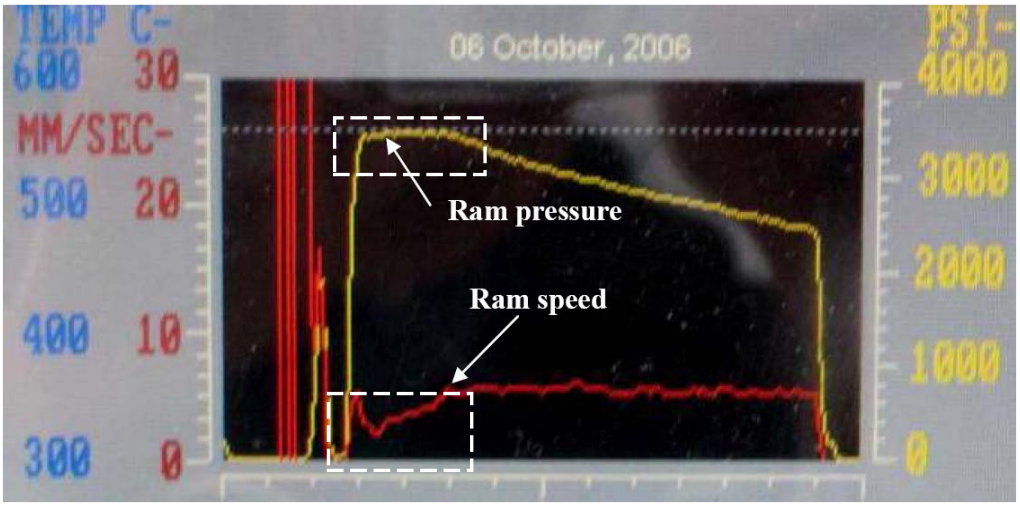

Figure 1.12: Ram speed and ram pressure curves obtained from Fletcher Aluminium

The magnitude of the extrusion pressure necessary to overcome the flow stress of the billet and friction is dependent on the strengthening contributions from solute atoms (Mg / Si), precipitates (Mg_2Si) and their total effects on softness of the billet. Additionally, the break through pressure increases with extrusion speed (strain rate). The constraints due to the maximum capacity of the machine require that, to improve productivity (and also improve die life), the billet preheating temperature must provide the lowest possible extrusion pressure.

Extrusion pressure does not linearly reduce with the increase of billet temperature, as will be explained. Additionally, there is an allowable maximum temperature of the extrudate when it exits the die. Hot tearing occurs, when the value of the die exit temperature is higher than that allowable value, and results in rejected product. Thus preheating temperature cannot be too high and extrusion speed needs to be lower than a certain value as deformation heat is generated during extrusion.

The chemical balance for solution of Mg_2Si in AA6xxx series aluminium alloys is presented in Eq. 1.3. The reaction tends to the left constituents when the solvus temeperature is exceeded, where T_{solvus} is Si% and Mg% dependent. In general, T_{solvus} is between 380°C and 430°C for AA6060 within the compositional specification of the alloy.

$$Al + 2Mg^{2+} + Si^{4-} \leftrightarrow Al + Mg_2Si \qquad (1.3)$$

Mg_2Si precipitates are generated during the air cooling process after homogenization. Reducing Mg_2Si is expected to soften the billet material and therefore increase the ram speed. Heat treatment may be used to dissolve Mg_2Si content by billet preheating to a temperature at or exceeding the solvus temperature (T_{solvus}). However, a billet temperature higher than T_{solvus} may have two conflicting effects. First, a higher temperature in general reduces the flow stress thus lowering the required pressure. On the other hand, at temperature higher than T_{solvus}, Mg_2Si should completely dissolve, resulting in solute solution strengthening thus increasing the flow stress. In this study, the exact resulting effect from the two will be investigated.

1.8 Objectives

The objective of the study is to quantify the strengthening effects on the as-received and preheated billet materials using room temperature mechanical testing and phase diagram analysis. The heat treatment temperatures are selected to fully enclose the preheating temperature range currently used in Fletcher Aluminium production; equivalently the test time exceeds the preheating time currently used in Fletcher Aluminium.

In this context, the following are the main aims of this research:

- To quantify strengthening contribution from solute atoms (Mg / Si) on as-received and preheated test samples.
- To quantify strengthening contribution from precipitates (Mg_2Si) on as-received and preheated test samples.
- To establish a relationship between total strengthening effect on strength of the test materials and preheating conditions (preheating temperature and time).
- To verify the relationship between hardness and tensile test results.

Additionally, the effects of strengthening are also to be investigated at elevated temperatures. Simulations of the extrusion will be conducted at elevated temperatures, by hot compression testing (Gleeble test), to measure the total strengthening effect of the billet material during deformation at elevated temperatures.

Chapter 2 Extrudability of Aluminium Alloys

Chapter 1 gave a brief introduction to extrusion, limiting pressure in Fletcher Aluminium. This chapter reviews the literature on extrudability of AA6060 aluminium alloys, formation of precipitates, phase transformations of Mg_2Si precipitates at different heating temperatures, dissolution of Mg and Si, strengthening effects (solid solution and precipitation strengthening), and the modelling analysis of the strengthening effects.

2.1 Extrudability

Extrudability is an extrusion process attribute, which includes the ability of any press to actually extrude a section, the ability of the alloy to be extruded at high speeds to ensure productivity, and the ability to develop aesthetically pleasing surface finishes [5]. It is improved by selecting processing parameters that increase the processing ability of the materials. The influence of billet preheating temperature upon extrudability is frequently presented in the form of an 'extrusion limit diagram' [12] where an example is shown in Figure **2.1**.

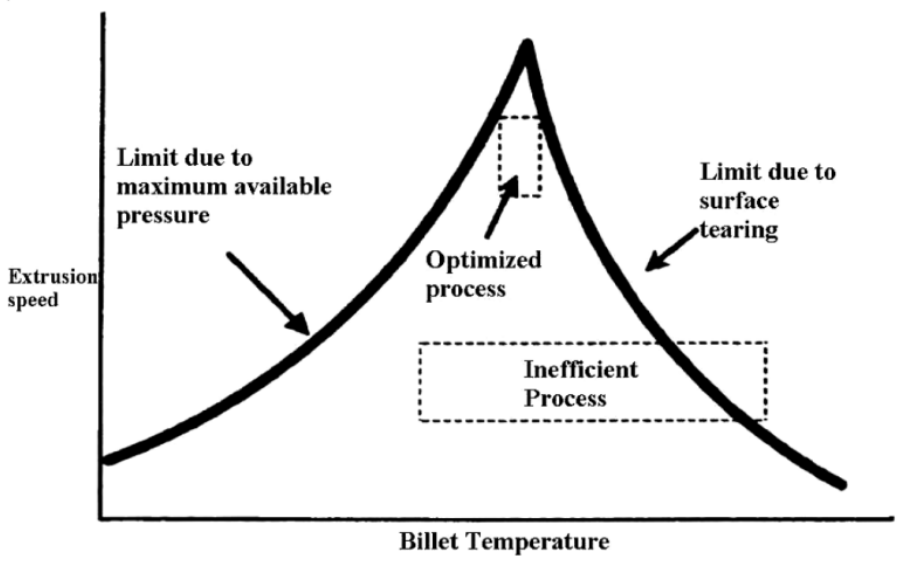

Figure 2.1: Example of simple extrusion limit diagram [12]

The left hand side of the diagram shows a reduction in extrudability as temperature decreases, which is caused by the attainable speed reaching a maximum due to

limitations in the available pressure. The right hand side of the diagram indicates reductions in the deformation heat necessary to reach critical temperatures that result in extrusion surface defects.

Formation of the alloying elements also has significant effects on the extrudability. In AA6060, precipitation of Mg_2Si must be minimised as an increase in Mg_2Si content within AA6060 results in a loss of hot workability [5]. Researchers have shown that, as the level of Mg_2Si precipitation at the grain boundaries increases, its fracture toughness and formability decreases [13-15]. Additionally, the extrudability also decreases with increasing amounts of Mg and Si in solid solution [5].

Hot tearing is a production defect which damages the surface of the extrusion product that is caused by incipient melting of Mg_2Si precipitates. Due to more heat generated during extrusion, the critical temperature for hot tearing is reached at a lower extrusion speed. If coarse secondary Mg_2Si particles do not dissolve during extrusion, a drastic reduction in extrudability occurs, which is due to incipient melting of these coarse particles.

2.2 Phase Transformations in AA6xxx Alloys

The primary alloy strengthening precipitate is magnesium silicide (Mg_2Si). Thermal cycles throughout the extrusion process promote the growth or dissolution of second phase particles. Many investigations have been performed in order to establish the precipitation sequence in the AA6xxx series aluminium alloys [16, 17]. Also the determination and characteristics of every phase has been thoroughly studied.

Figure **2.2** shows the quasi-binary Al-Mg-Si alloy phase diagram. The amount of Mg_2Si that is present depends on the amount of elemental Mg and Si that is in the alloy. Mg_2Si dissolves into solid solution when the temperature is increased from room temperature to (a temperature within the alpha region). Phase transformations reach an equilibrium state when the temperature is maintained for a sufficient time within the alpha region. If the temperature is subsequently reduced below the solvus line, there will be a reduction in the solubility of Mg_2Si, and excess Mg_2Si will tend to precipitate [16].

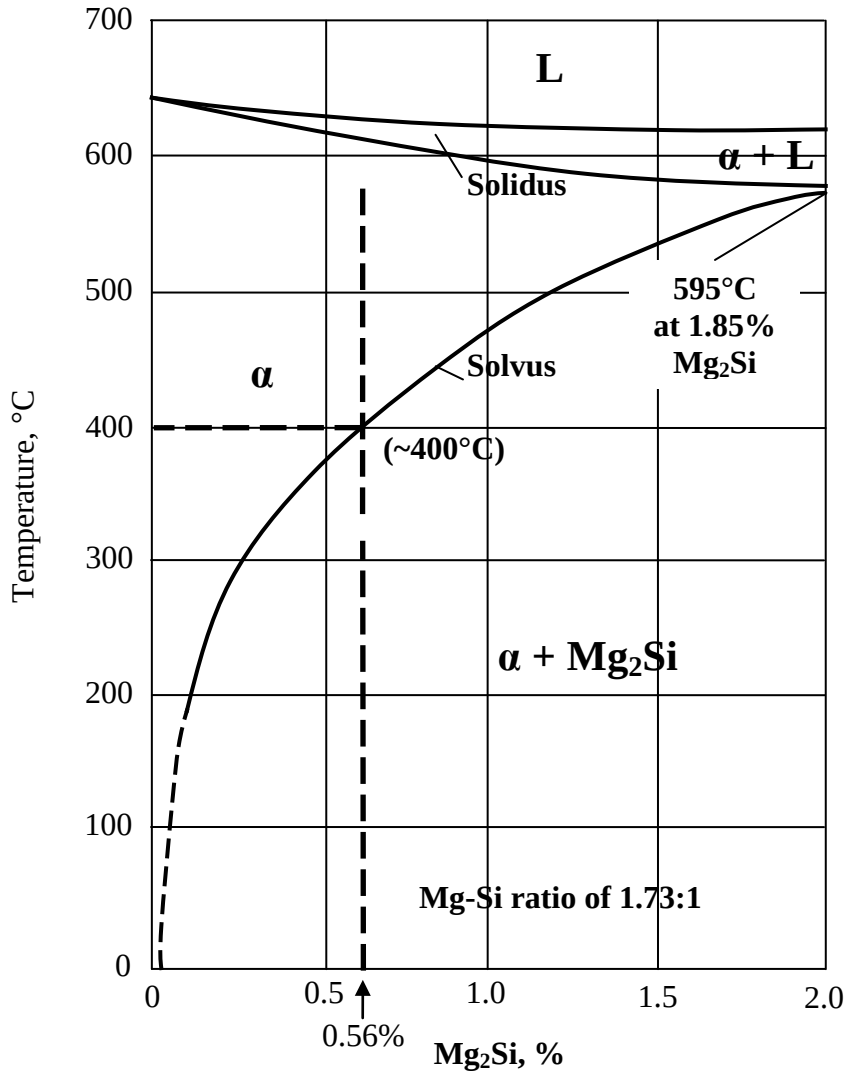

Figure 2.2: Quasi-binary phase diagram for Al-Mg-Si alloy indicating important transition zones [redrawn from Rashid's diagram [16]]

The Mg content of the supplied alloys varies between 0.35% and 0.36%; it would require 0.20% to 0.21% Si to fulfil the stoichiometric requirements for Mg_2Si. The Mg_2Si would then constitute ~0.56 weight percent of the alloy as indicated in Figure **2.2**. The vertical line in Figure **2.2**, showing the Mg_2Si content range around 0.56%, intersects with the solid solubility line at about 400°C. Kwon et. al. [17] have shown that the main precipitate Mg_2Si phase start to dissolve into the matrix at temperatures above 400°C for AA6061 and AA6083 aluminium alloys.

Many alloys are not of balanced (stoichiometric) compositions, either by design or due to limited chemistry control. Such alloys are described as having "excess Mg" or "excess Si". Wright [18] suggested that excess Mg reduces the maximum solubility of Mg_2Si, without substantially changing the temperature of maximum solubility.

Additionally, excess Si lowers the temperature of maximum solubility and also reduces maximum solid solubility. Wade [19] has concluded that excess Si actually increases Mg_2Si solid solubility in the lower temperature ranges. Figure **2.3** displays the interpretations of the roles of excess Mg and excess Si. Therefore, precipitation of the Mg_2Si phase occurs in the temperature range approximately from room temperature to 380°C for the supplied excess Si alloys.

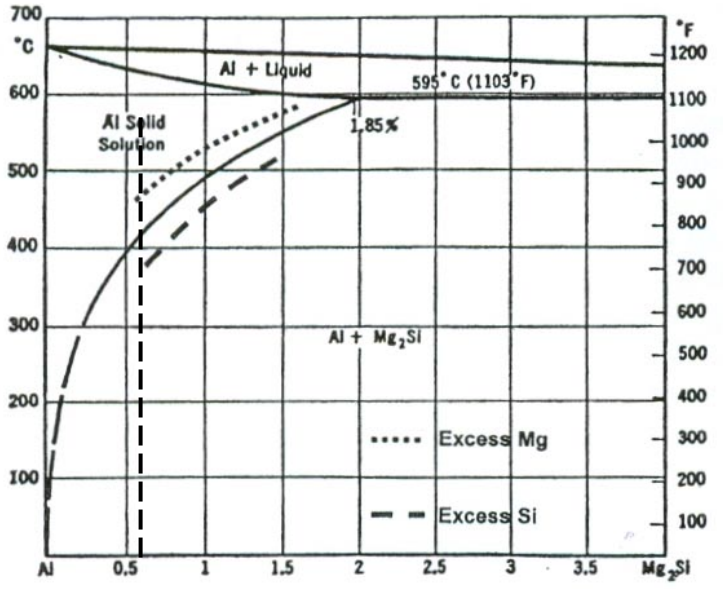

Figure 2.3: The effect of excess Mg and excess Si on solvus of the Al-Mg2Si pseudo-binary phase diagram [19]

2.2.1 Precipitate Phases

Comprehensive overviews of the available literature on heat treatment of AA6xxx alloys have been made by Altenpohl [20]. The strength of an AA6xxx series alloy is controlled by the precipitates, the dimensions of which are at the nanometer level. The precipitation sequence during cooling of AA6xxx material from a solid solution condition is shown below:

$$SSS\ atomic\ clusters \rightarrow GP \rightarrow \beta'' (Mg_5Si_6)\ needles \rightarrow \beta' (Mg_{1.7}Si)\ rods \rightarrow \beta (Mg_2Si)\ plates \quad (2.1)$$

A summary of the precipitation phases formed during heat treatment are presented in Table **2.1**. Each phase has a unique chemical composition and structure and resultantly each provides unique contributions to material strength and hot workability. Extrudability is the most favourable attribute of AA6063 is billet, and is maximised when the Mg_2Si precipitate should be in the β' phase [20]. The precipitation of the

correct phase of Mg_2Si is important in controlling the kinetics of precipitate dissolution because equilibrium β-Mg_2Si tends to form relatively coarse precipitates bounded by mobile, high energy boundaries which do not hinder the dissolution kinetics of this phase significantly.

Table 2.1: Precipitation phases in Al-Mg-Si alloys

Phase	Formula	Unit-cell	Morphology / Typical size	Ref.
GP	Si/Mg ≥ 1	Unknown	Spherical / 1-2 nm	
β"	Mg_5Si_6	Monoclinic C2/m		
		a = 1.516 nm	Needles	
		b = 0.405 nm	4 x 4 x 35 nm^3	
		c = 0.684 nm		
		β ~ 105.3°C		[20]
β'	$Mg_{1.8}Si$	Hexagonal	Ribbons /	
		a = 0.705 nm	Several μm long	
		C = 0.405 nm		[20-22]
β	Mg_2Si	fcc (CaF2 - type)	Plates or cubes /	
		a = 0.639 nm	Up to 10-20 μm diameter	[20, 23]
Si		fcc (diamond type)	Thin plates /	
		a = 0.543 nm	Up to 10-20 μm diameter	[22]

Initially, mono-atomic clusters of Mg and Si form from solid solution, followed by a growth of Mg-Si clusters [24, 25]. The first significant precipitate to form is the intermediate metastable precipitate GP (Guinier Preston) zone. It is a metallic phase [26] with Al, Mg and Si, ordered on the FCC aluminium grid. The GP zones are strongly coherent within the aluminium matrix. Maximum precipitation hardening occurs at the β" phase [4, 24], which has a monoclinic structure with an ideal composition Mg_5Si_6. The cell dimensions and atomic coordinates of the Mg_5Si_6 structure are shown schematically in Figure **2.4**, where two monoclinic unit cells are displayed.

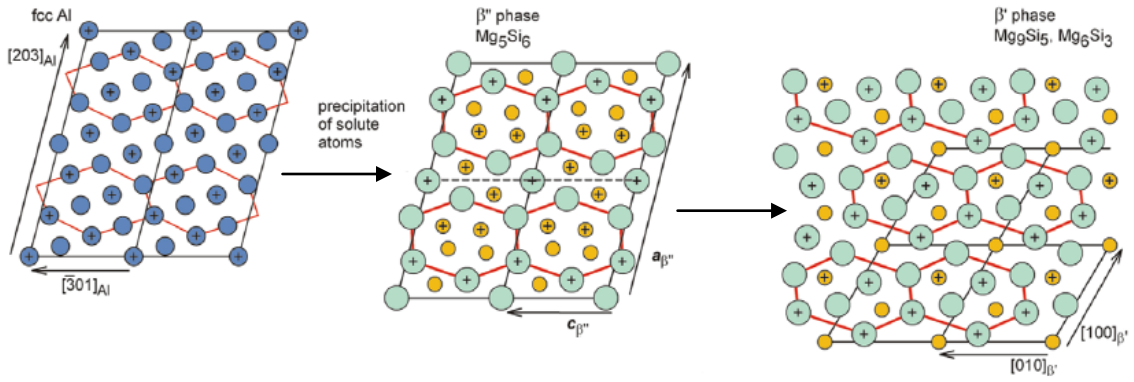

Figure 2.4: Various precipitate phases and phase transitions that occur during the precipitation sequence [22]

Andersen and Hoier [27] found that below 85°C no meta-stable phase is present, but the alloying elements formed atomic clusters. Heating above 125°C leads to the transformation of GP zones into β''. The rod-like β' phase has been identified with the composition $Mg_{1.8}Si$ as displayed in Figure **2.4** [22]. At temperatures above 200°C, nucleation of the β' phase predominately takes on the β'' phase, as this phase dissolves. The density of the β' phase is less than the density of the β'' phase and it coarsens quickly with the heating time. The β' is not an equilibrium phase therefore at temperatures above 300°C, the β' phase dissolves quickly. Finally, the stable β phase is the cubic anti-fluorite Mg_2Si phase that is present in over-aged samples.

2.2.2 Phase Transformation of Mg_2Si

There is little intrinsic resistance to dislocation glide in aluminium, and it is very soft in the absence of defects such as other dislocations, solutes, second-phase particles and grain boundaries. Alloying elements provide resistance to dislocation, where strengthening effects are shown in Figure **2.5**.

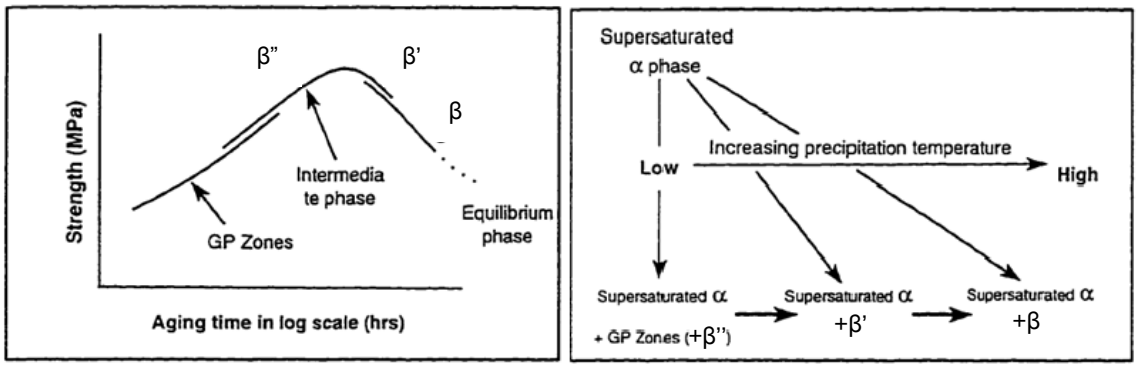

Figure 2.5: Precipitation sequence showing changes in precipitate phases with (a) aging time and (b) aging temperature [16]

β'' and β' are metastable phases of Mg_2Si that may be present in the microstructure, in addition to the stable β phase. These phases will precipitate under certain conditions of time and temperature. Hardening in such alloys occurs mostly due to precipitation of metastable β'' precipitates. The strengthening process is accelerated as the temperature is increased as shown in Figure **2.5** (b). Over aging results in a reduction in strength due to continued particle growth and the development of β' and β phases.

Figure **2.6** shows a schematic T-T-T (time-temperature-transformation) diagram indicating the precipitation sequence during cooling of dilute Al-Mg-Si alloys of the AA6063 type, and shows that the Mg_2Si precipitate can take two forms, one occurring in an upper temperature range (β) and the other in a lower range (β'). In contrast, the β' metastable phase, which forms at lower temperature, tends to be bounded by partially coherent interfaces and due to nature of their low mobility, limit the rate of precipitate dissolution [22].

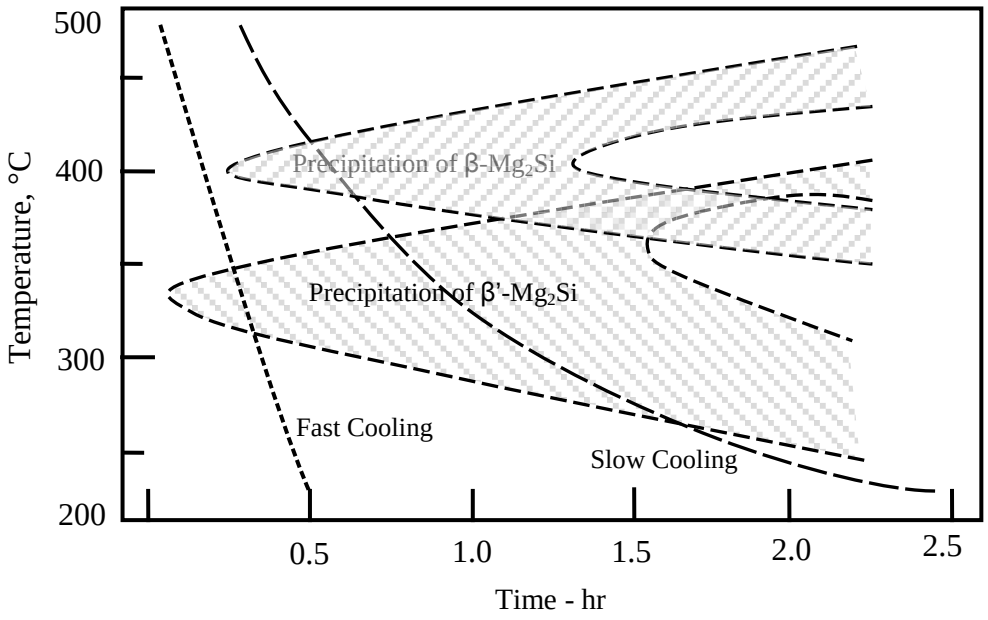

Figure 2.6: Schematic T-T-T curves for Mg2Si precipitation in AA6063 [redrawn from Sheppard's diagram [5]]

Quantitative information concerning the presence or absence of Mg_2Si precipitates and the Mg and Si solute content in an extrusion billet, is used to assess extrusion behaviour as a function of prior thermal history and composition. The precipitation times for each precipitate during the heat treatment are shown in Table **2.2**.

Table 2.2: Details of the heat treatments [28]

Sample code	Quench and precipitation temperature (°C)	Precipitation time (s, x 10^3)
WQ	Room temperature	-
β''	185	21.6 – 86.4
β'	250	3.6 – 21.6
β	367 – 450	14.4 – 48

Zajac et al. [29] suggested that, in homogenized AA6063 billets, the Mg_2Si particles can precipitate as β-phase blocks in a cubic array on holding at 400 – 500°C or as meta-stable β'-phase platelets of hexagonal crystal structure on holding at 300 – 400°C.

2.2.3 Microstructure of Second Phase Particles at Elevated Temperatures

All physical and mechanical material properties primarily depend on the structure of the materials. Frequently, desirable properties are attained by altering the microstructures of alloys by heat treatment. Myhr et al. [30] investigated microstructure evolution during multistage thermal processing on AA6005 from room temperature to elevated temperatures using Transmission Electron Microscopy (TEM) to capture the surface images shown in Figure **2.7**. The AA6005 material was solution heat treated at 530°C for 30 minutes, water quenched, then artificially aged at 185°C for 2 hours to create base samples. The base samples were then reheated to various temperatures (315°C, 390°C and 450°C).

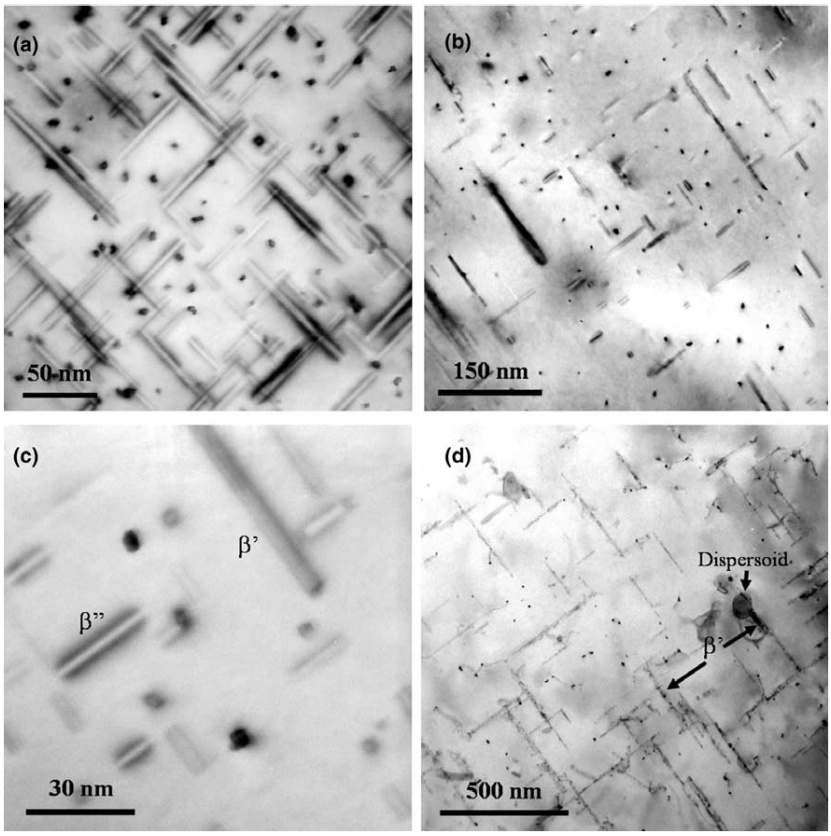

Figure 2.7: TEM bright field images of microstructure observed in aged AA6005 alloy [30] (a) Artificial aging; (b) 10 second holding time, reheating temperature 315°C; (c) Close up of precipitate shown in b (d) 10 second holding time, reheating temperature 390°C

Figure **2.7** (a) shows the TEM micrograph of the hardening precipitates that are present in the base material when reheating the AA6005 after artificial ageing where the majority are β'' particles. A base sample reheated to 315°C is shown in Figure **2.7** (b) and (c) where the microstructure of the base sample consists of a mixture of coarse, rod-shaped β' particles and fine β'' particles. Therefore, transformation from β'' to β' precipitates occurs to an increasing extent with increasing temperature. β' phase precipitates are the dominating micro-structural constituent for the base sample reheated to 390°C shown in Figure **2.7** (d). At higher temperatures, the β' precipitates become increasingly unstable and start to dissolve, until they eventually disappear at about 450°C, leaving behind a particle-free aluminium matrix with all Mg and Si in solid solution [30].

2.3 Strengthening effects by Heat Treatment

Heat treatment is used to modify the properties of metals and alloys by changing the microstructure. The main strengthening mechanisms in aluminium alloys are solution strengthening and precipitation strengthening; in many cases one of these mechanisms is dominant. Physically based models of strength development in precipitation-hardening alloys have been constructed using a range of approaches. The main elements in such models are the description of the thermodynamics (equilibrium and metastable equilibrium), the kinetics of transformations and the relation between strength and microstructure, which is determined by the interaction between dislocations and elements in the microstructure. The heat treatments required to achieve the strengthening effects are shown in Figure **2.8**.

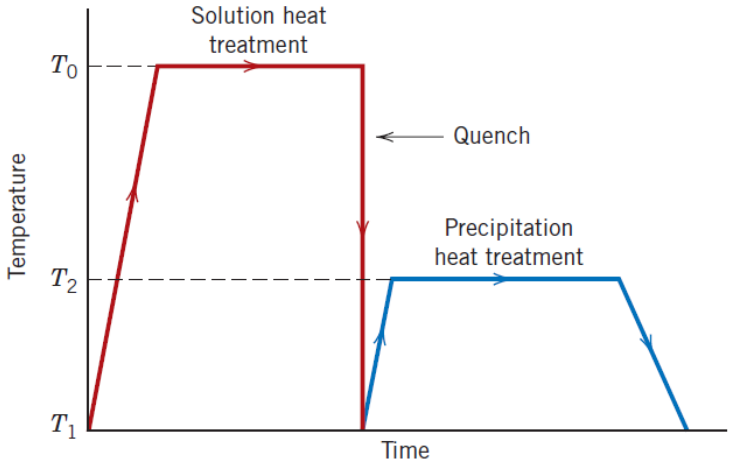

Figure 2.8: Schematic temperature versus time plot showing solution and precipitation heat treatments [31]

2.3.1 Solid Solution Strengthening (SSS)

Solid solution strengthening dissolves all the phases into one homogeneous phase where the solubility of an element in the matrix depends strongly on the temperature. The solubility of alloying elements in a matrix, is very slow at room temperature, and increases with temperature. Solution heat treated alloys' possess improved strength because impurity atoms that dissolve into solid solution normally impose lattice strains on the surrounding host atoms. Therefore, dislocation movement is restricted by the lattice strain field interactions between dislocations and the impurity atoms [32].

Precipitates for AA6xxx aluminium alloys are usually made up of Mg_2Si and Si. At the start of the treatment the solutes are in patches of highly concentrated alloying elements

(precipitates) of different size that provide barriers to flow of the material during deformation. These precipitates dissolve into the material as the temperature of the alloy approaches or exceed T_{solvus}. The phase transformations encountered during solution heat treatment are shown in Figure **2.9**.

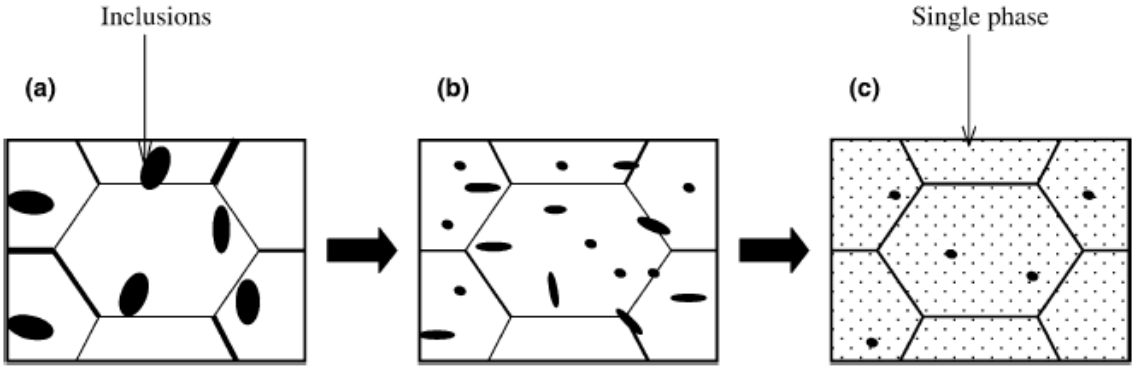

Figure 2.9: Schematic diagram showing the microstructure evolution for the material, (a) before SHT; (b) intermediate SHT; (c) after SHT [32]

2.3.2 Precipitation Strengthening (PPT)

Precipitation hardening heat treatment is a sequential process which involves three major steps: solution heat treatment, quenching, and aging. The mechanical properties achieved in the alloys depend on control of temperature and duration during these processes. After quenching from the solidus state, precipitation is achieved by reheating the alloy below the solvus line at a suitable temperature for a suitable time. In this process solute atoms diffuse to form small precipitates. The maximum amount of precipitates which can be formed is given by equilibrium amount. Further exposure at the aging temperature will lead to growth of the particles or coarsening of precipitates which will reduce the effect of precipitation strengthening.

Precipitation of a second phase (solute rich particles) from the matrix is normally used to increase strength, hardness and other mechanical properties. These second phases are metastable and therefore transformed into equilibrium phase with time. The structure during strengthening consists of particles dispersed in a ductile matrix which impede dislocation motion. A stronger material will result from the fine dispersion of these particles.

A dislocation is a linear or one-dimensional defect around which some of the atoms are misaligned [31]. The internal strains around the precipitates provide obstacles to dislocation motion and the density of these precipitates is such that dislocations cannot

pass through these precipitates. Thus additional stress is needed for this shearing resulting in an increase in the strength of the alloy. The shearing of precipitate by a dislocation is shown in Figure **2.10**.

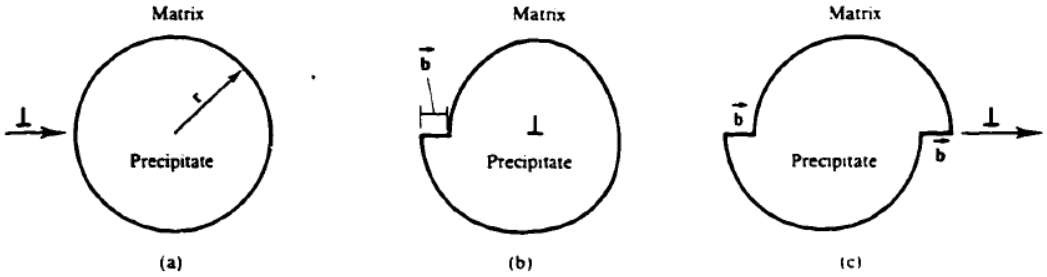

Figure 2.10: Shearing of precipitate by dislocation [33]

Interactions between dislocations and precipitates are schematically shown in Figure **2.11**. The mechanical properties (yield strength and work hardening rate) are dependent on the movement of dislocations through an array of precipitates. The movement of dislocations in precipitation hardening materials strongly depends on the morphology of particles in the matrix such as size distribution, shape of particles and volume fraction [34, 35].

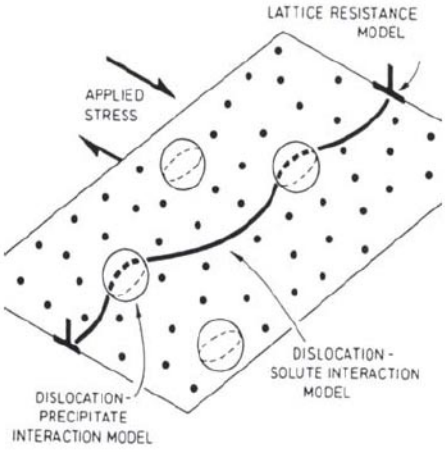

Figure 2.11: A schematic illustrating the interaction of dislocation line with precipitates [34]

Second phase coarsening is a process where the interphase surface area and the number of second particles per unit volume of the system, decrease with time at elevated temperatures. The kinetics of phase coarsening in microstructures is controlled by

induced multiparticle diffusion. The enhanced solubility of fine particles mean that smaller particles shrink and disappear, while the larger ones grow and increase the overall size of the dispersed phase particles [36, 37]. Figure **2.12** shows this behavior schematically.

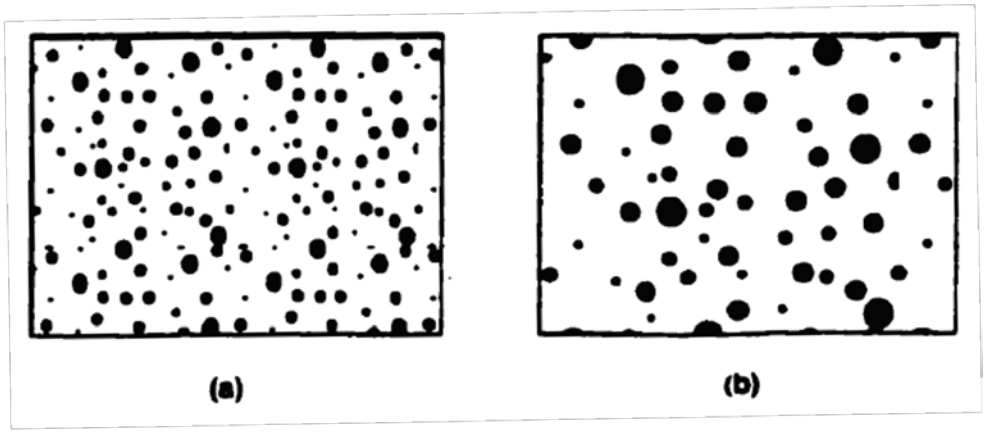

Figure 2.12: (a) Initial microstructure; (b) Final microstructure of coarsening particles [36]

Slow cooling after homogenization and preheating the billet to the temperature below the T_{solvus} result in nucleation and growth of Mg_2Si precipitates in the grain, along the grain boundaries and on the iron-rich particle surfaces. Inter-granular deposits of Mg_2Si increase the billet extrudability, but melted Mg_2Si particles encourage surface defects on the final product [38].

2.3.3 Cooling Rate Effect after Homogenization

Mg_2Si dispersion for AA6xxx during heat treatment changes the microstructure of the alloy significantly. Figure **2.13** shows the thermal cycle of water quenched and air cooled sample material, after homogenization. At a heating condition of 465°C, approximately 2 hours is required for complete dissolution of Mg_2Si [5]. The as-received billet material is homogenized at 580°C for 2 hours followed by air cooling to room temperature. Heating at a temperature of 580°C ensures the temperature of the billet core will exceed 465°C, and therefore that Mg_2Si will dissolve at the billet core.

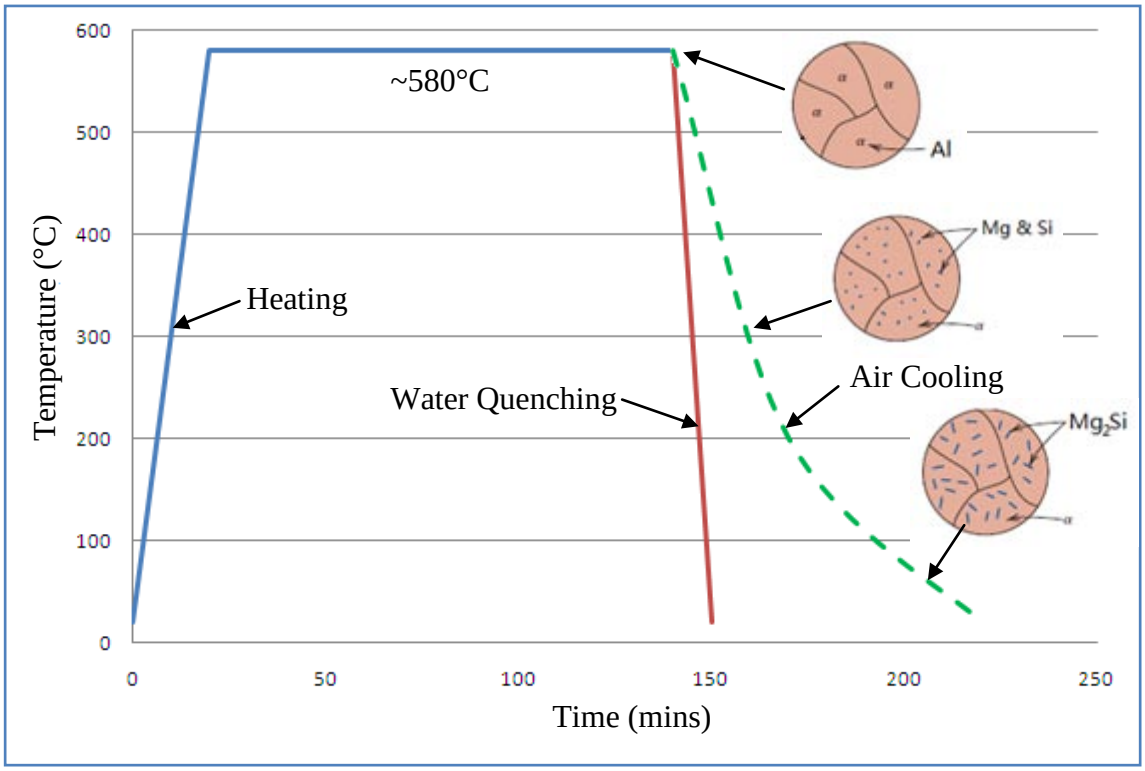

Figure 2.13: Thermal cycle of entire homogenization process with micro-structural illustrations at points during air cooling

The cooling rate after homogenization influences the alloy microstructure. A rapidly cooled water quenched billet inhibited precipitation of either form of Mg_2Si [39-41], which is indicative of all magnesium and silicon being retained in solid solution; the material structure will be the same as the top most phase diagram in Figure **2.13**. The water quenched billet material is difficult to extrude due to a large amount of solution strengthening, but has less surface quality defects than slowly cooled variants. This can be inconsequential provided that the machine is powerful enough.

Slower continuous cooling than the cooling generated by water quenching, causes precipitation of β, β' and β''. The cooling profile is very critical as it affects the proportion of β, β' and β'' phases. Slower cooling caused precipitation of both β' and β. At high temperatures, above 400°C, Mg_2Si precipitates as a cubic β-phase and below 400°C as meta-stable β'-phase. The proportion of β and β' particles depend on the cooling sequence[40, 41]. An air cooled as-received billet will form Mg_2Si precipitate, as per observations by Ricks et al. [39] and Zajac et al. [40], which leads to the formation of predominantly β' phase particles with the absence of any β phase Mg_2Si in the microstructure. The formation of Mg_2Si is observed in the progression of phase diagrams displayed in Figure 2.13. Comparing the particle structures at different

temperatures during the cooling, it may be seen that the β'-Mg_2Si particles tend to be finer and their density higher at the lower temperature. This means that the higher density β'-Mg_2Si particles at lower temperature will generate more precipitation strengthening which will increase the alloy strength. However, the material needs to be in its softest condition during extrusion. Therefore, in order to avoid any Mg_2Si re-precipitation, fast cooling is needed after homogenization. The preheating step to the extrusion temperature must also be correctly controlled for the same reasons.

2.4 Material Strength Modelling

Material state analysis is based on thermodynamics, kinetics and dislocation mechanics. The methodology described by Shercliff and Ashby [42] uses a combination of sub-models to predict yield strength (YS) after various heat treatments. Included in the model are expressions for:

- The decrease in solute concentration and growth in volume fraction of precipitates during the low temperature range of precipitation
- The effect of heating temperature on the equilibrium volume fraction of precipitates
- The coarsening of precipitates
- The strengthening contribution from solute atoms
- The strengthening contribution from precipitates

The total yield strength (σ_{YS}) of a precipitation hardened AA6060 alloy is reported to be the sum of the yield strength of pure aluminium (σ_O) and the contributions to the yield strength due to the eutectic Si particles (σ_{Si}), eutectic Fe-phase particles (σ_{Fe}), Si in solid solution ($\sigma_{\mathrm{SS,Si}}$), Mg in solid solution ($\sigma_{\mathrm{SS,Mg}}$), Si precipitates ($\sigma_{\mathrm{PPT,Si}}$) and Mg-Si precipitates ($\sigma_{\mathrm{PPT,Mg-Si}}$) [43]:

$$\sigma_{YS} = \sigma_o + \sigma_{Si} + \sigma_{Fe} + \sigma_{SS,Si} + \sigma_{SS,Mg} + \sigma_{PPT,Si} + \sigma_{PPT,Mg-Si} \qquad (2.2)$$

Changes in the Si concentration, of a binary Al-Si alloy, from 0.16 to 0.17 wt.% are known to increase YS in the heat treatment condition by not more than 1 MPa [44]. Although $\sigma_{\mathrm{SS,Si}}$ may vary with heating temperature and time, these effects are expected to be minimal. Even though fine-scale Si clustering and Si precipitation is expected to occur in the alloys under some pre-heating conditions [45], it is not known to what

degree such Si clustering and precipitation may influence YS. Rather than estimating an unmeasured effect, it is assumed that $\sigma_{SS,Si}$ is negligibly small, especially in relation to the very large strengthening contribution due to Mg-Si type precipitates, in order to simplify the equation [46]. Eq. 2.2 can be simplified since σ_{Si}, σ_{Fe} and $\sigma_{SS,Si}$ are expected to remain relatively unchanged during pre-heating. Consequently, Eq. 2.2 may be simplified to:

$$\sigma_{YS} = \sigma_i + \sigma_{SS,Mg} + \sigma_{PPT,Mg-Si} \qquad (2.3)$$

Where σ_i is the intrinsic strength, which is the sum of σ_o and the strengthening contributions that remain constant during heat treatment. Possible differences in pre-heating characteristics between dendritic and eutectic regions are considered negligible since the α-Al phase is homogenized throughout during solution treatment.

The contributions of strengthening to heat treated test alloys can be considered to be independent [47]. The relationship in equation Eq. 2.3 is then designed assuming the grain size effect is negligible for this alloy system [48].

$$\sigma_{YS} = \sigma_{sss} + \sigma_{ppt} + \sigma_{intrinsic} \qquad (2.4)$$

Where σ_{sss} is due to solid solution strengthening, σ_{ppt} is the yield strength contribution due to precipitation strengthening and $\sigma_{intrinsic}$ is the default strength without treatment.

The intrinsic yield strength is the sum of all yield strength contributions that have negligible change during heat treatment. It is approximated as the yield strength of pure Aluminium ($\sigma_{intrinsic}$) where its yield strength is measured to be approximately 15 MPa [49, 50].

Precipitates provide obstacles to dislocation motion, and have a form dependent on heat treatment history [47]. The precipitate strength thermal response, is modelled according to the theories for strengthening mechanisms, as well as the micro-structural and mechanical behavior of the alloy.

Chapter 3 Room and Elevated Temperature Testing

Vickers hardness testing, tensile testing and the hot deformation test (Gleeble test) are implemented in the study to provide information about supplier material properties. The state of the art in these material testing methods are presented in the following sections.

3.1 Vicker Hardness Test

The hardness test is a common mechanical test used to estimate the mechanical strength of metallic materials [21, 51, 52]. Hardness values obtained from hardness tests are a measure of the material resistance to permanent or plastic deformation, where larger hardness values are associated with greater resistance to deformation [9, 53]. The Vickers hardness test was selected to measure the hardness of the preheated AA6060 alloys in this study.

Vickers hardness testing involves pressing an indenter into the surface of the test material using a controlled force, removal of the indenter, then measurement of the indentation size (see Section 4.3). Factors which contribute to hardness measurement errors include vibration during hardness testing, a hard surface layer of the sample, elastic back deformation (Figure **3.1**), certain instrumental errors, the limit of resolution of the optical system and sliding (dislocation) processes around the edge of indentation.

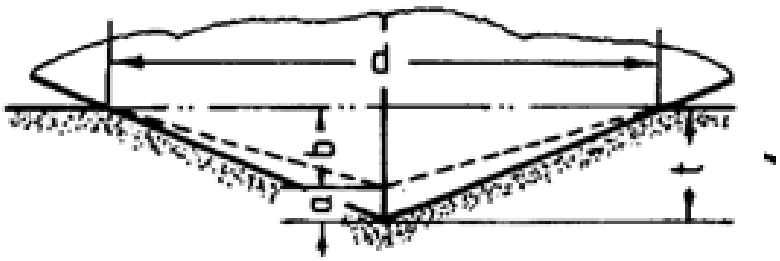

Figure 3.1: Simplified geometry of the cross section of a Vickers impression [54]

On the removal of the indenter, size and shape changes of the impression are recognized to occur as a result elastic recovery. In the micro-hardness test, the influence of elastic deformation is noticeable. Some researchers [21, 54, 55] have proposed a variation in hardness value due to variation in the elastic recovery of the indentation diagonals

during unloading. They suggest that when the load is removed, elastic recovery leads to an apparent increase in hardness. An illustration of such an effect is given in Figure **3.1** which shows the simplified geometry of the cross-section of a Vickers impression. Cai et al. [54] studied the influence of elastic recovery on the hardness results and suggested that the elastic depth recovery of the indentation is much larger than that of the diagonal after load removal. Additionally they found that a unique relationship between hardness and tensile strength does not exist.

Shen et al. [51] have investigated the hardness – strength correlation, and focused on composites containing relatively smaller particles. AA2080 was selected for their tests as the indented region is large as compared to the size and spacing between the particles. Figure **3.2** shows the microstructure of the depressed region caused by indentation of a hardness tested AA2080 composite. As the indenter moves downward during the test, it encounters resistance from a material with an increasingly greater concentration of hard particles.

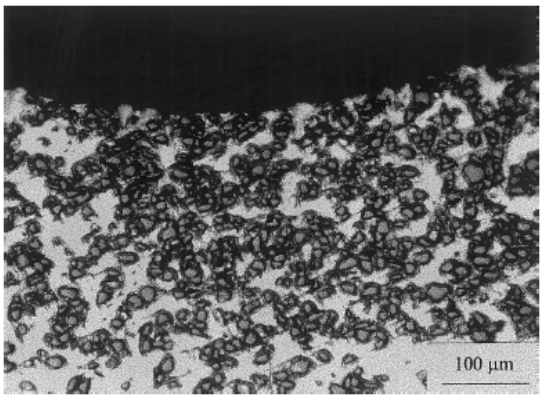

Figure 3.2: Optical micrograph near the indentation site [50]

3.2 Tensile Test

Tensile properties indicate how the material will react to forces being applied in tension. A tensile test is a fundamental mechanical test to measure the applied load and the elongation of the sample over some distance. Figure **3.3** shows a typical (engineering) stress versus (engineering) strain curve. Two important strength values measured from a tensile test are yield strength and ultimate tensile strength, where each is indicated in Figure **3.3**. Yield strength (YS) is the stress at which material strain changes from elastic deformation to plastic deformation causing it to deform permanently. It is measured as the stress necessary to produce a small-specified amount of plastic deformation.

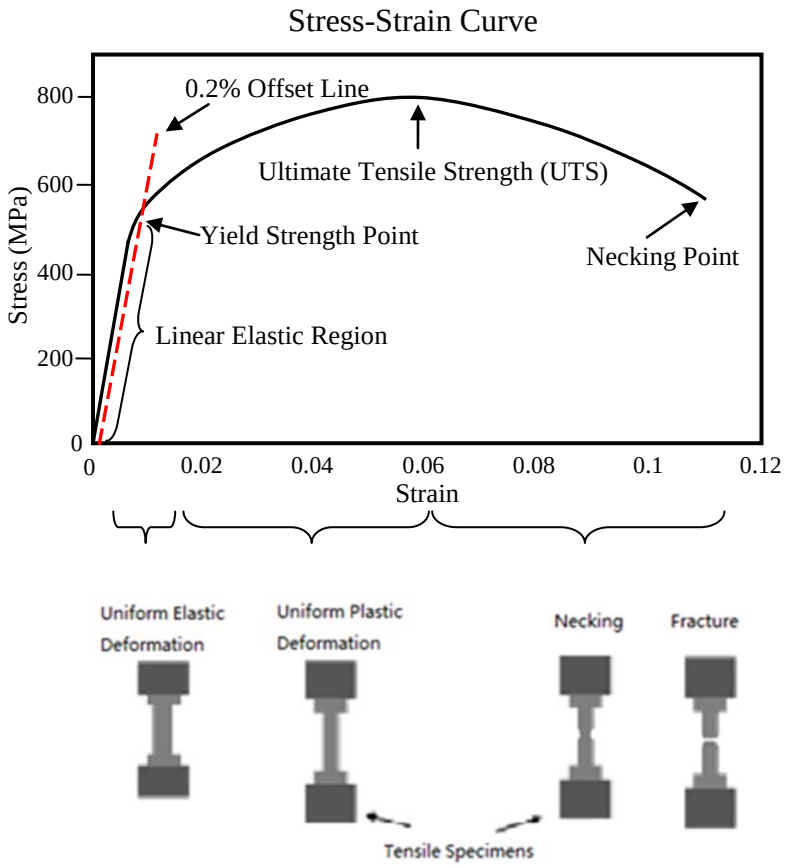

Figure 3.3: A typical stress – strain curve [redrawn from Oliver's diagram [55]]

The yield strength obtained by an offset method is commonly used for engineering design and specification applications. The offset method involves drawing a line parallel to the stress-strain line and intersecting with the point on the strain axis (0.002). This line will intersect the stress-strain line slightly after it begins to curve, and that intersection is defined as the yield strength with a 0.2% offset as illustrated in Figure **3.3**. Ultimate tensile strength (UTS) is indicated by the maximum stress of a stress-strain curve and also indicates when necking will occur. It is used to specify a material and for quality control purposes as the UTS is easy to determine and reproducible.

Table **3.1** (page 33) lists the yield strength and ultimate tensile test values for AA6060 for various heat treatment conditions. Large differences in yield strength and ultimate tensile strength are observed for the three AA6060 samples showing that mechanical strength is extremely dependent on the heat treatment process.

Table 3.1: Mechanical properties of AA6060 after various heat treatment processes [55]

(MPa)

	Solutionised & naturally aged		Artificially aged only		Solutionised & artificially aged	
AA6060	YS	UTS	YS	UTS	YS	UTS
	68	131	110	151	215	240

True stress versus true strain plots use stress and strain values that are compensated for the change in cross sectional area due to necking of the sample. Engineering stress, engineering strain data and instantaneous diameter measurements obtained from uniaxial tensile tests of cylindrical samples, are used to calculate true stress versus true strain plots. The relationship between true stress and true strain for a heat treated sample used in the study is shown in Figure **3.4**. A plot of true stress-strain data on logarithmic coordinates shows a linear region where plastic deformation occurs; the gradient of this region is known as the strain hardening exponent.

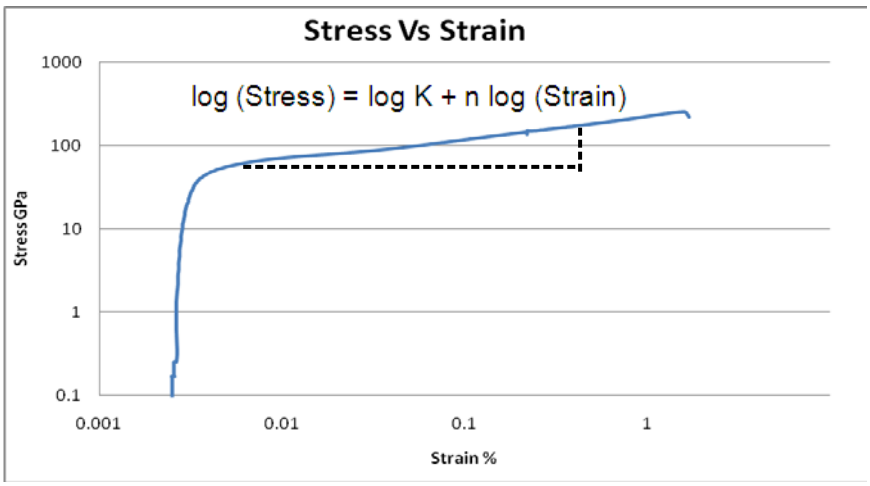

Figure 3.4: True Stress – True Strain Curve on Logarithmic Scale

True stress-strain curves are used for metal forming analysis during elastic and permanent deformation. The true stress-strain curve can be easily calculated by measuring the cross section reduction and the corresponding load. The true stress and true strain are determined from the measurement of the engineering stress – strain relationship according to the following formula [31]:

$$\sigma_T = \sigma_E(1 + \varepsilon_T) \quad (3.1)$$

$$\varepsilon_T = ln(1 + \varepsilon_E) \quad (3.2)$$

where σ_T is the true stress, σ_E is the engineering stress, ε_T is the true strain and ε_E is the engineering strain. The strain behaviour is summed by a power law [5, 53, 56]:

$$\sigma_T = K \cdot {\varepsilon_T}^n \quad (3.3)$$

Where σ_T is the true stress, ε_T is the true strain, K is strength coefficient and n is the strain hardening exponent. The values of stress during uniform deformation are almost on a straight line,

$$log\,\sigma = log\,K + n\,log\,\varepsilon \quad (3.4)$$

whose slope is equal to the strain hardening exponent (n), and is simply called the n value.

The value of the strain hardening exponent (n value) describes the amount of uniform plastic strain the material can undergo during a tensile test before strain localization, or necking, sets in leading to failure [57]. Materials that have higher n values have better formability (including extrudability) than those with low n values. The strain-hardening exponent, n, is zero for perfectly plastic solids, and 1.0 for elastic solids. Most metals have n in the range of 0.1 to 0.5 [21]. As metals work harden, their remaining capacity for work hardening decreases. Therefore, high strength tempers of a given material typically would have lower n values than lower strength of the same alloy.

The work-hardening characteristics of aluminium alloys vary considerably with temperature [58]. The work hardening of alloys depends on the precipitation distribution, precipitate sizes and the solute level left in the metal matrix. Zajac et al. [59] reported that the work hardening exponent is a function of particle size and is attributable to dislocation accumulation at the particles. Additionally, Zajac has shown that above a critical particle diameter (6 μm), dislocations accumulate at the particle as geometrically necessary dislocations which lead to a complex dislocation structure that is responsible for an increase of the work hardening exponent.

Figure **3.5** shows the stress – strain curves for different n values. Higher n values mean greater hardening effects which cause higher stress increments as the strain increases.

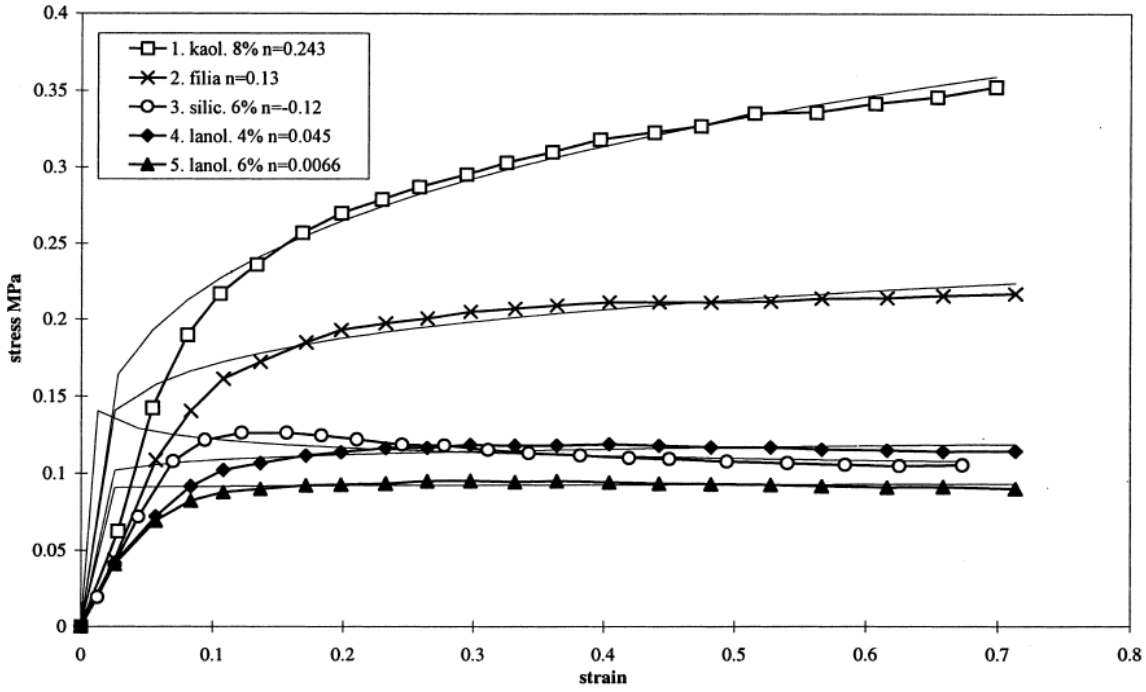

Figure 3.5: The characteristic stress-strain curves [60]

Friis et al [61] investigated solutionized and work hardened test samples and showed strengthening contributions due to solid solution strengthening and work hardening. Although, the results indicate that the presence of solute in solid solution has a stronger effect on the work hardening of the materials during deformation than the presence of non-coherent second phase particles. Improved work hardening is provided by dissolved particles within the cooled material which contribute to the formation of strain fields which act as obstacles for dislocation motion [61]. Schematic representations of the precipitate orientation in the aluminium matrix and the resulting triangular array of obstacles on the slip plane are shown in Figure **3.6**.

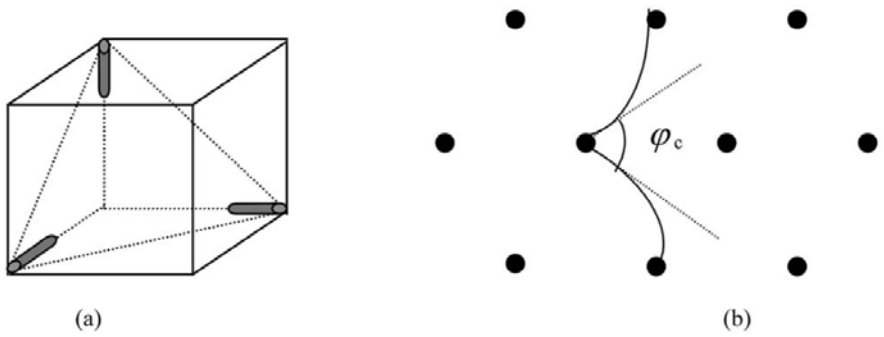

Figure 3.6: (a) Orientation relationship between the precipitates and matrix; (b) Dislocation-obstacle interaction in a triangular array of obstacles [50]

3.3 Hardness and Tensile Parameter Relationships

The correlation between various hardness scales and tensile strength has been compiled for a variety of metals and alloys [62]. Establishing a correlation between hardness and tensile parameters is beneficial as it provides a method to quickly estimate material properties, and is therefore important in quality control. Many researchers have attempted to develop mathematical relationships between hardness and tensile properties. However, results reported in the literature are inconsistent. Tiryakioglu et al. [63] and Rometsch [47] studied hardness – YS relationships in aluminium alloy (Al-7wt.% Si-Mg) with different temperature and found a curvilinear relationship between Rockwell, Brinell hardness and yield strength. They suggested that the tensile stress at a strain of 8% correlates well with the Vickers and Brinell hardness than the correlations between yield strength and hardness as shown in Figure **3.7** and Figure **3.8**.

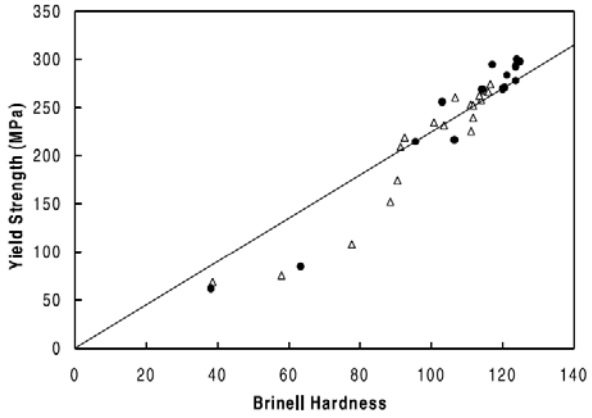

Figure 3.7: Plot of yield strength against Brinell hardness [47]

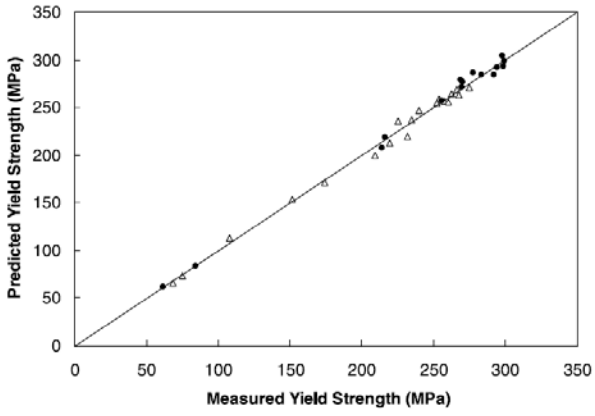

Figure 3.8: Stress as a function of hardness (better correlation) [47]

However, Shen et al. [51] proposed that there is no linear correlation because of variations due to different modes of testing (tensile versus compressive) and differences

in local material deformation (concentrated deformation at tip of hardness tester versus uniform stress field of tensile test specimen).

3.4 Hot Deformation Test (Gleeble Test)

Increasing the amount of alloying elements such as Si, Mg, Mn and Fe is expected to result in an increase of the material strength. However, the principal basis of precipitation strengthening also lowers the hot workability [64, 65]. The most important mechanism for microstructural control is to provide suitable properties during hot deformation.

Fabrication of aluminium alloys is usually at elevated temperatures (hot worked) since it provides lower flow stresses and higher ductility as a result of dynamic recovery [66]. The extrusion process is complex, and involves the interaction between the process variables and the materials' high-temperature properties. Extrusion productivity is influenced by many different factors where theoretical process variables are the extrusion ratio R, the ram speed V_R, and the extrusion temperature T. Normally, the extrusion ratio is fixed by customer specification therefore the temperature and the speed are the only controllable factors. The primary change is high temperature flow stress during the extrusion process.

Control of the billet hot workability during extrusion may be improved through knowing the link between the hot deformation behaviour of billet materials and the microstructural evolution occurring during preheat treatment. It may be investigated using a series of hot compression tests and varying the deformation temperature and strain rate. The hot deformation characteristics of the alloy are influenced by various parameters shown in Eq. 3.5 [67].

$$\sigma = \sigma\,(T, \varepsilon, \dot{\varepsilon}, \textit{fitting parameters}) \qquad (3.5)$$

The Zener-Hollomon parameter (Z value) describes the effect of strain rate ($\dot{\varepsilon}$) and temperature (T) on stress and microstructure during hot deformation of metallic materials. Industrial production can use this relationship in process to predict parameters affecting extrudability. In Eq. 3.6, the definition of the Zener-Hollomon parameter is given [5, 65, 66];

$$Z = \dot{\varepsilon}\, exp\left(\frac{Q}{R\,T}\right) = A\big(sinh(\alpha\,\sigma)\big)^{n} \qquad (3.6)$$

In which Z is the temperature-compensated strain rate, Q is the activation energy for deformation, R is the universal gas constant (R = 8.314 J/mol K), ἐ is the mean equivalent strain rate, α is the stress multiplier. A, α, n and Q are materials constants. The mean equivalent strain rate is specific to the extrusion geometry and the temperature, T, varies during the extrusion. The activation energy is regarded as a material constant in the hot deformation range. In this study, the strain rate uses a constant value, therefore the flow stress affected by varying of the strain rate will not be considered.

Table 3.2: Values of Zener-Hollomon parameters

Alloys	**Temperature (°C)**	**Ln Z**	**Ref.**
AA6060	300 – 500	34 - 26	[68]
AA6061	300 – 500	31 – 23	[64]
AA6063	300 – 500	31 – 23	[69]
AA6063	300 – 500	30 – 22	[70]
AA6082	300 – 500	33 – 25	[5]

The apparent activation energy (Q value) is a physical parameter that indicates deformation difficulty during plastic deformation [66, 71, 72]. The Q value varies with solute content as each dissolved alloying element provides strengthening due to constraints and internal stresses. The total metallic solute results in a variety of Q values for alloys with different chemical compositions. A stationary dislocation in a solid solution can be pinned by the solute atoms if they are able to diffuse to the dislocation. Hence an additional increment of stress will be required to free the dislocation from its original position. In addition, any dislocation moving through a solid solution will encounter friction drag thus raising the energy required for movement. Hence any increase in foreign atoms held in solution will increase the activation energy [66, 73].

A value of 153 kJ/mol for lattice self diffusion in pure aluminium has been established. The constitutive constants are given in Table 3.3. Many reviews and studies on hot working in aluminium alloys report activation energies for Al-Mg-Si during hot working as approximately 150 kJ/mol [64].

Table 3.3: Constitutive constants for Aluminium alloys

	Mg %	Si %	Mg_2Si %	α Mpa	n	Q_{HW} KJ/mol	Ln A	Ref No.
AA1050	–	–	–	0.037	3.84	157	26.69	[5]
AA1100	–	–	–	0.045	5.66	158	24.67	[5]
AA2014	–	–	–	0.0152	5.27	144	24.42	[5]
AA6060HE	0.4	0.35	0.63	0.04	4.8	175	–	[71]
AA6060NS	0.4	0.5	0.63	0.03	5	160	–	[71]
AA6060NH	0.5	0.43	0.79	0.052	4.2	183	–	[74]
AA6060	0.97	0.45	1.23	0.035	4.7	161	–	[68]
AA6061	–	–	–	0.045	3.55	145	19.3	[5]
AA6063	–	–	–	0.04	5.385	142	22.5	[69]
AA6063	–	–	–	0.04	5.4	140	22.5	[70]
AA6082	–	–	–	0.045	2.976	153	19.3	[5]
AA6105	–	–	–	0.04	3.502	145	20.5	[5]
AA7050	–	–	–	0.027	2.86	152	22.85	[5]

3.4.1 Deformation at Elevated Temperature

Recent studies have suggested that the flow stress during hot deformation of AA6xxx aluminium alloy diminishes with rise in deformation temperature, and flow curves are marked by a peak and softening which declines as deformation temperature rises [75-77]. When temperature is increased during the deformation, stress is lowered and extrudability is increased. However, hardening mechanisms in hardenable aluminium alloys are complicated, as the improved mechanical properties are a result of the combination of precipitation hardening and deformation hardening. It is desirable that billets be fabricated into components by traditional mechanical forming process to allow high productivity. Hot compression testing at a variety of heating conditions allows the acquisition of stress-strain curves and analysis of microstructural evolution.

Sheppard [11] investigated the results obtained from torsion and from compression of a number of AA7xxx alloys. As the temperature rises, the two sets of data (Ln Z and flow stress) coincided as shown in Figure **3.9**.

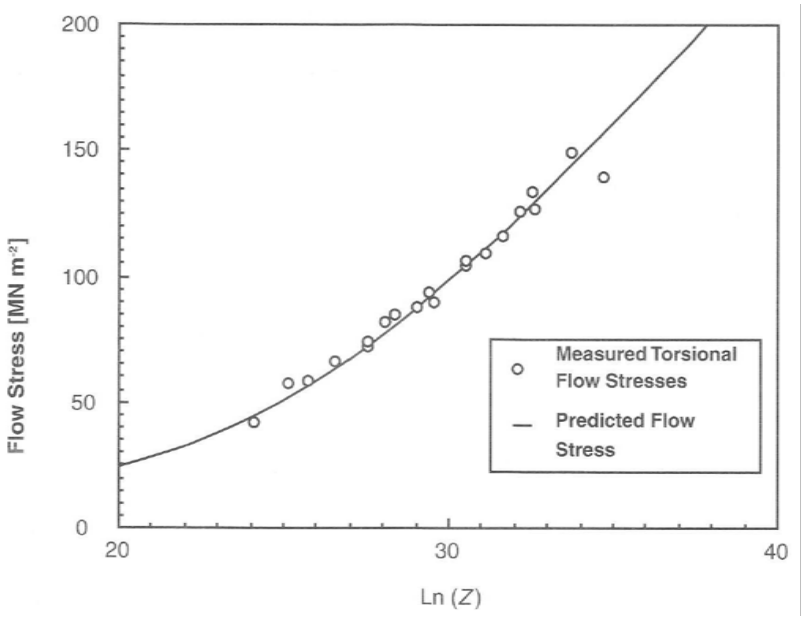

Figure 3.9: Comparison of the Ln Z with flow stress [78]

Alloying produces either a solid solution, or a distribution of second phase particles. Both products increase strength by decreasing the mobility of dislocation motion. Many researchers found that the high alloying elements alloys are indicative of the material's intrinsic ability to resist deformation, and in the alloys dislocation mobility is impeded to a large extent by the second phase particles. Clode and Sheppard [76] compared different hot deformation properties between AA6063 and AA7075 alloys. The loads required to extrude the AA7075 alloys are much greater under the same conditions than those required for AA6063 as shown in Figure **3.10** [5, 64].

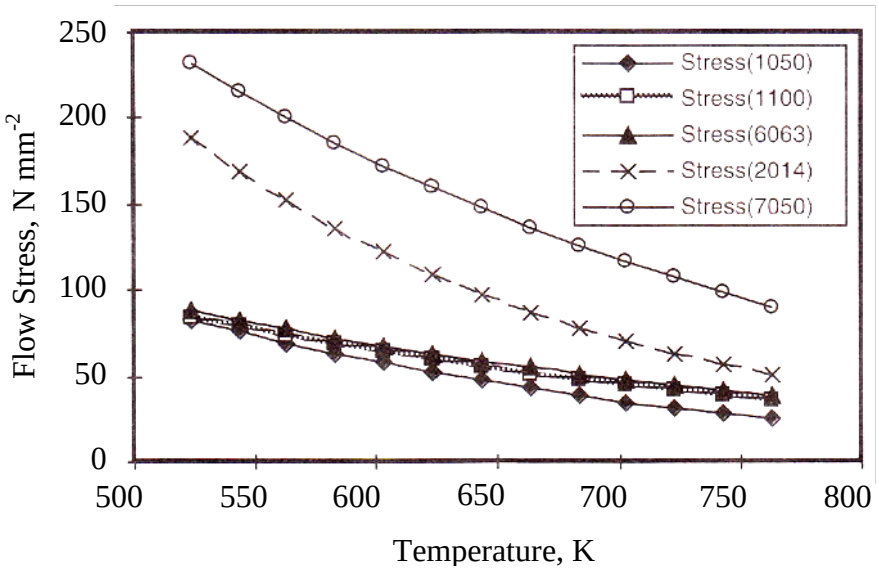

Figure 3.10: Comparison of the temperature response of different alloys [5]

A comparison of the flow stress values obtained from torsion testing on some AA6xxx alloys is shown in Figure **3.11**. They show the same temperature dependence on flow stress, and the specific values are what would be expected. Highly alloyed materials or those alloys containing high Mg contents have a higher flow stress [5, 64].

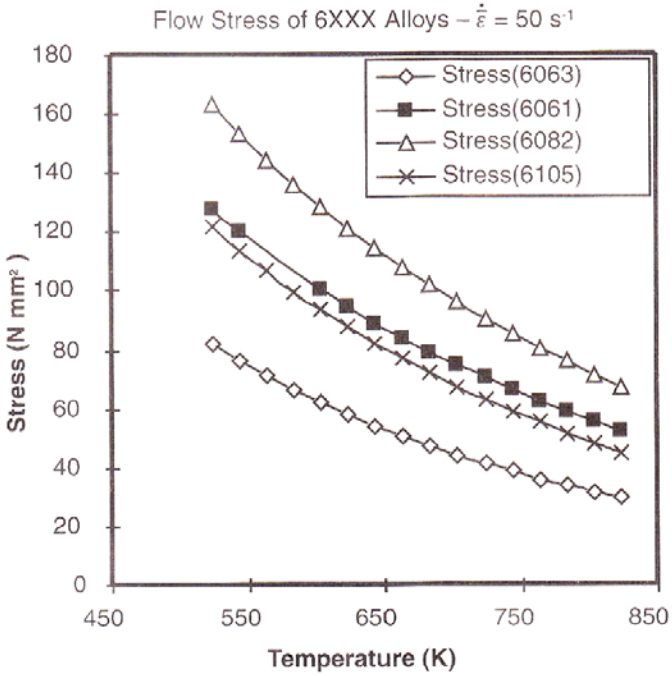

Figure 3.11: Comparison of AA6xxx alloys [5]

During steady state deformation, the work hardening processes occurring in the material are in dynamic balance with the work softening processes. Vacancy diffusion is a softening mechanism that operates on most aluminium alloys during hot working and contributes to dynamic recovery.

3.4.2 Softening Behaviour during Hot Deformation Test

Figure **3.12** show the effects of work hardening and dynamic recovery on the form of the high temperature stress-strain curve. This temperature is normally above the recrystallization temperature of the material [65].

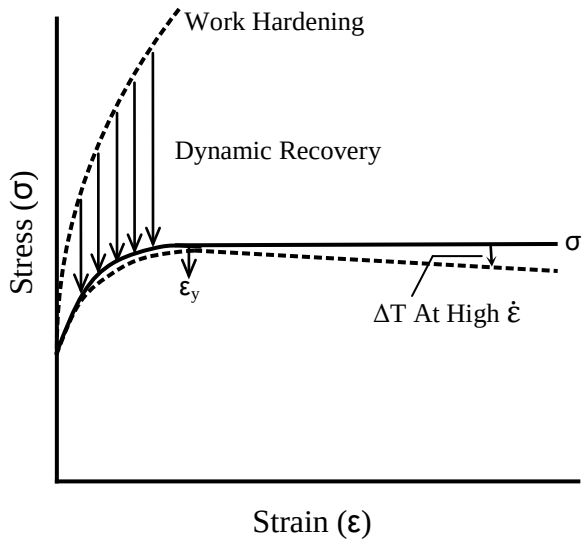

Figure 3.12: Schematic diagram showing the effects of work hardening and dunamic recovery on the form of the high temperature stress strain curve [redraw from Sellars's diagram [65]]

With an increase of strain during deformation, work hardening and dynamic softening occurred simultaneously. As the strain increases during deformation, the grains become thinner and the serrations in opposite elongated boundaries come into contact, shortening the grains and leading to grain refinement with crystallites [66]. The sharp increase in the flow stress is characteristic of dominant work hardening at the beginning of deformation. Hardening and softening reach a balance when deformation reaches a certain strain value and flow stress value attains a stable stress value.

Dynamic recrystallization occurs during hot compression deformation and the grain size is significantly dependent on deformation temperature, strain rate, and Zener-Hollomon parameter Z. Decreasing the Z value, that is increasing deformation temperature, leads to more adequate proceeding of dynamic recrystallization and coarser recrystallized grains [66]. Nengping et al. [72] investigated hot compression tests of AA7150 aluminium alloy performed using the Gleeble-1500 system in the temperature range from 300°C to 450°C and at strain rate range from 0.01 s^{-1} to 10 s^{-1}. The results show that the peak stress level decreases with increasing deformation temperature and decreasing strain rate, which can be represented by the Zener-Hollomon parameter in Eq. 3.6.

Chapter 4 Materials & Experimental Procedures

This research began with an extensive series of heating experiments with a wide range of conditions that cover, and are beyond, the current temperature and heating time ranges used in the pre-extrusion billet heating process. Homogenized AA6060 aluminium billets from two Fletcher Aluminium suppliers were used in these experiments. A large amount of heat treated samples were then prepared for hardness measurement, room temperature tensile testing and high temperature compression testing. Details of these are given in this chapter.

4.1 Test Materials

Commercial grade Al-Mg-Si alloy is currently supplied to Fletcher Aluminium from two suppliers. The majority (95%) of billet material is supplied by Rio Tinto Alcan New Zealand Limited (RTA) and the remaining billet material is sourced from Hydro's Kurri aluminium smelter in Australia (Hydro). Chemical compositions are provided for RTA and Hydro billet material in Table 4.1.

Billets with a diameter of 202 mm are cast and treated in an industrial homogenization furnace by the aluminium smelters. Homogenization treatment of the ingots at the smelter sites is generally performed by soaking at 575 – 580°C for 2 hours, followed by fan induced air cooling to room temperature.

Table 4.1: Specified compositions for RTA & Hydro aluminium alloys

Element	% Composition in RTA	% Composition in Hydro
Al	Remaining	Remaining
Mg	0.36	0.36
Si	0.53	0.52
Fe	0.18	0.17
Mn	0.04	0.06
Cr	0.01	<0.001
Cu	0.01	<0.001
Ti	0.01	<0.001
Zn	0.01	<0.001
Other	0.04	<0.001

4.2 Sampling

Samples oriented parallel to the extrusion direction, were obtained from the mid radial position of homogenised billet material provided by RTA and Hydro. Figure **4.1** shows a cross section view of the as-received billet and the location of the mid radial samples. The microstructure of the homogenized billet changes slightly as a function of radial position due to several thermal history considerations presented in Section 1.1.5.

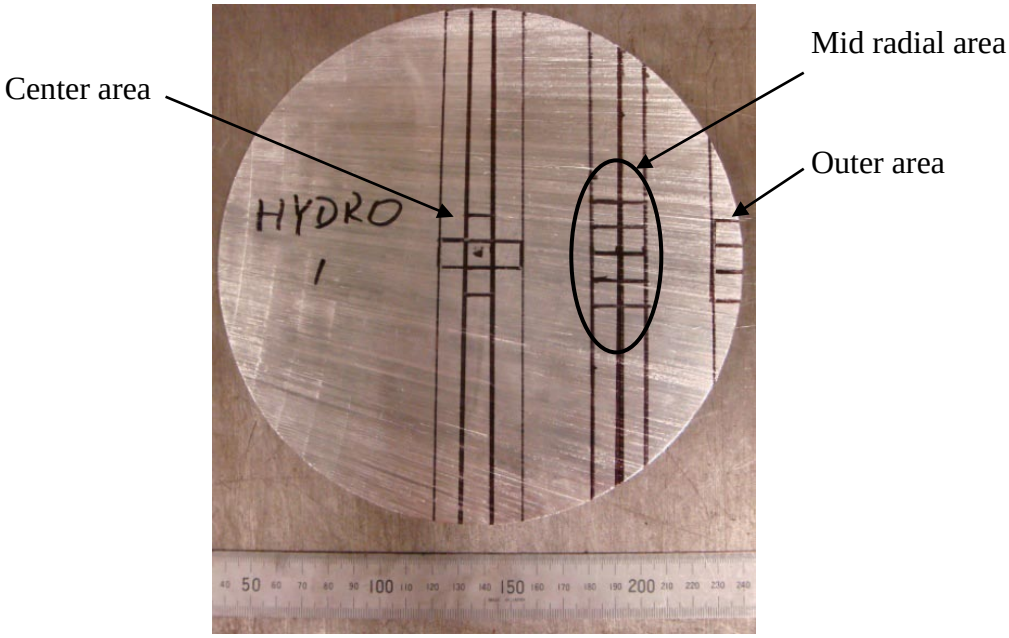

Figure 4.1: Test sample selection from the billet

The test samples extracted from the billet are selected from the mid radial area as it represents the average quality of the material used in the final extruded product. Cuboidal samples (20 X 20 X 120mm) from the mid-radial region were cut from each of the billets, under a flow of lubricant, using a Kasto power hack saw. These were further machined for the various experiments using the quantities and overall dimensions shown in Table **7.1** (Appendix B). Detailed information on the sampling and dimensions used in the manufacture of test samples are presented in the following sections. For Gleeble tests, only samples for RTA were tested as they represent the majority of billets extruded of Fletcher Aluminium (over 90%).

4.3 Hardness Test

Hardness test samples were cut to 10mm X 10mm X 15mm cuboids using a handsaw under a flow of cooling liquid to prevent frictional heating. A hardness test sample, before preheating, is shown in Figure **4.2**.

Figure 4.2: Hardness test sample

4.3.1 Sample Heating

The samples were heat treated at a range of temperatures and times. Heat treatment of the samples was conducted using the furnace shown in Figure 4.3.

Figure 4.3: Furnace in AUT

A container was constructed to allow the measurement of ambient and approximate sample temperatures. Two thermocouples were used to perform these measurements and were located as shown in Figure 4.4(a). Thermocouple A was exposed and suspended in the center of the furnace cavity to monitor the air temperature in the furnace.

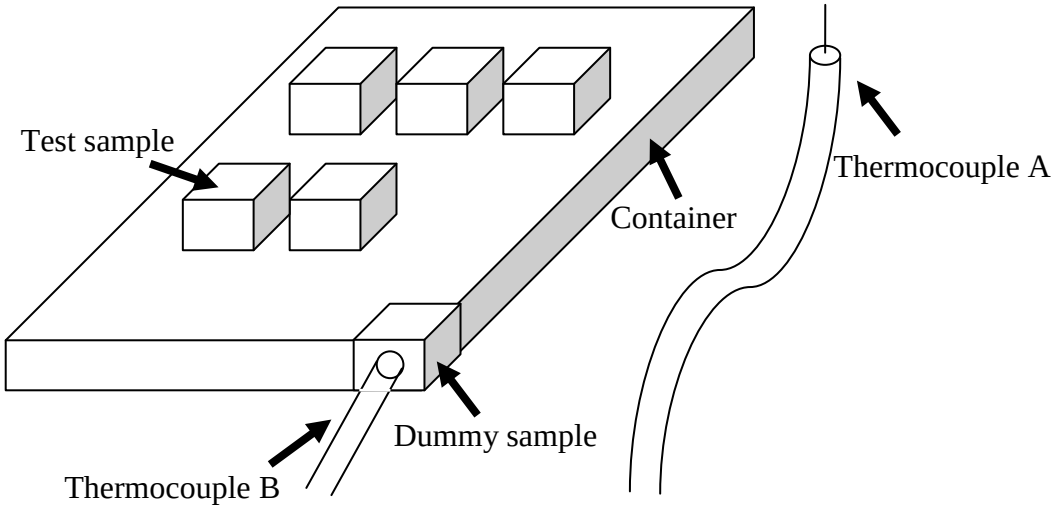

Figure 4.4: Schematic front view of thermocouple A & B in furnace

Thermocouple B was plugged into a "dummy" sample within a carry container as indicated in Figure **4.4**. The dummy sample is used to estimate the internal temperature of the heat treated samples and is made from the same material as the test sample. The thermal cycle of the heating process was recorded with a data logger.

Hardness test samples were heat treated in the furnace as presented below. The furnace was preheated according to thermocouple A, to 330ºC. Five samples were placed into the sample container and the sample container placed upon a meshed bracket in the center of the furnace. The data logger was turned on to record the temperature of the dummy block and the furnace air temperature at 2 second intervals. The samples were left in the furnace for a heating time of 15 minutes. The furnace door was opened, a single sample was removed, the furnace door closed, and the sample rapidly quenched in water. A second sample was removed after 25 minutes, and remaining samples at 40, 60 and 85 minutes where each sample was rapidly quenched upon removal from the furnace. Each sample was then labeled to enable identification. The tests were then repeated for each of the remaining heating time and temperature combinations shown in Table **7.2** and Table **7.3** (In Appendix B) so that samples from thirty-five different temperature/time combinations were produced.

All samples were labelled using three characters: X / X / X. The first letter refers to the alloy supplier, the second number gives the heating temperature and the last number is the heating time. The resulting samples possess different metallurgical microstructures which influence the behaviour of the materials under various loads and heating

...ental cycle Furnace shown in Table **7.2** and Table **7.3** will be used in ... the report when comparing tests.

The ... recorded by thermocouple B for each of the seven furnace heating ... shown in Figure 4.5. There are small drops in the internal temperature ... when the furnace door was opened to obtain a sample. The internal ... recovers towards the set temperature within the first 15 minutes. ... in the time that the sample was removed from the ... by the addition of the temperature depressions.

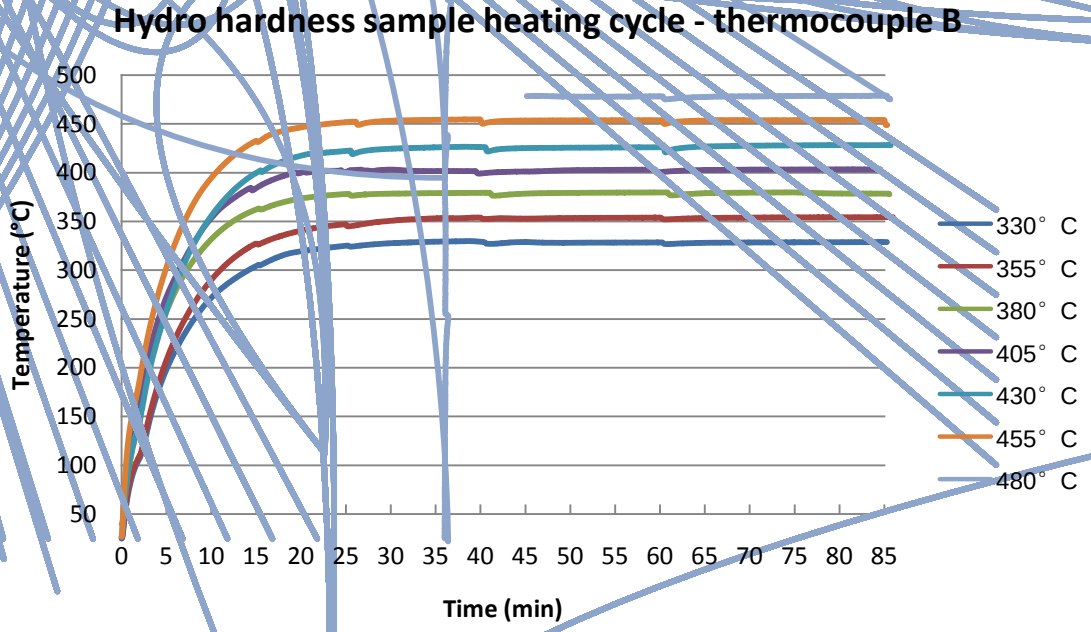

Figure 4.5: Temperature profile for thermocouple B during heating of Hydro samples

Comparison between the heating profiles for each temperature shows that there is no overlap between the heating profiles for each temperature. This strong difference in temperature between samples allows for the investigation on the effect of heating temperature on billet mechanical behaviour.

Figure **4.6** shows a comparison between readings obtained from thermocouple A for the seven heating cycles. The furnace temperature is maintained at a constant temperature though a drop in the furnace temperature of up to 50°C is observed each time a sample is removed. However, the furnace temperature recovers its ambient temperature within one minute of closing the furnace door. Temperature profiles comparing thermocouple A and B readings are presented in Appendix F.

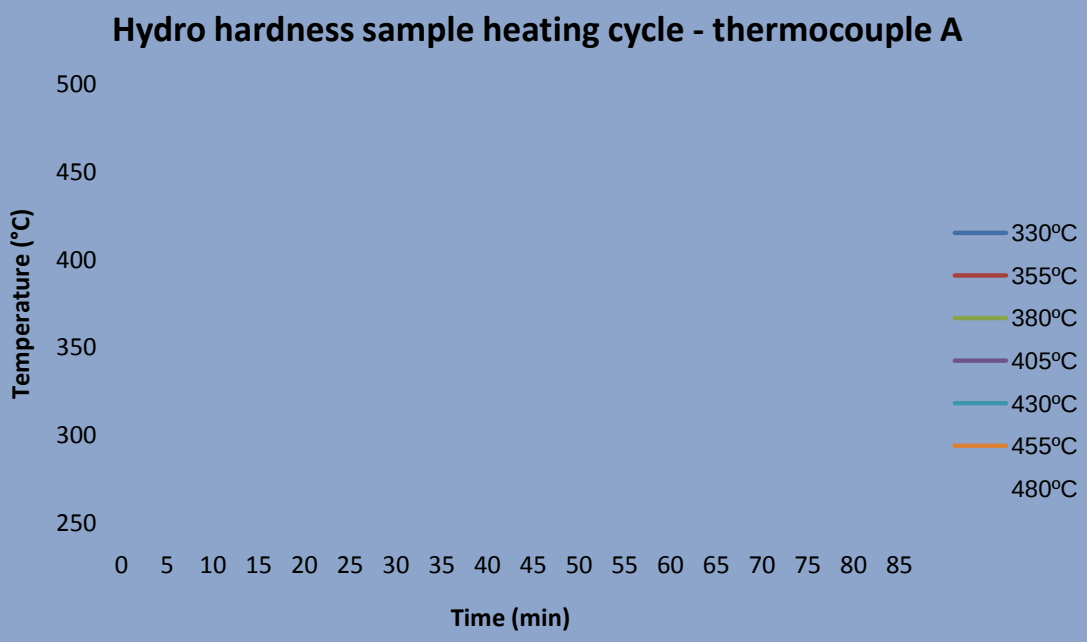
Hydro hardness sample heating cycle - thermocouple A
Temperature (°C)
500
450
400
350
300
250
0 5 10 15 20 25 30 35 40 45 50 55 60 65 70 75 80 85
Time (min)
330ºC
355ºC
380ºC
405ºC
430ºC
455ºC
480ºC

(a) (b)

Hardness tests were performed on both Hydro and RTA heat treated alloys using a Vickers micro-hardness tester. The hardness tester utilized for the tests is presented in Figure **4.8**.

Figure 4.8: Vickers Micro-hardness Tester

The hardness tester applied a load of 200 grams for 10 seconds and permanently dented the sample surface. The pyramid-shaped diamond indentation was measured under a microscope to obtain the dimensions shown in Figure **4.9**, and the two dimensions were averaged. A conversion table was then used to obtain the Vickers Hardness value (HV) from the average reading. Fifteen readings of hardness were obtained from each sample, and an average hardness value calculated.

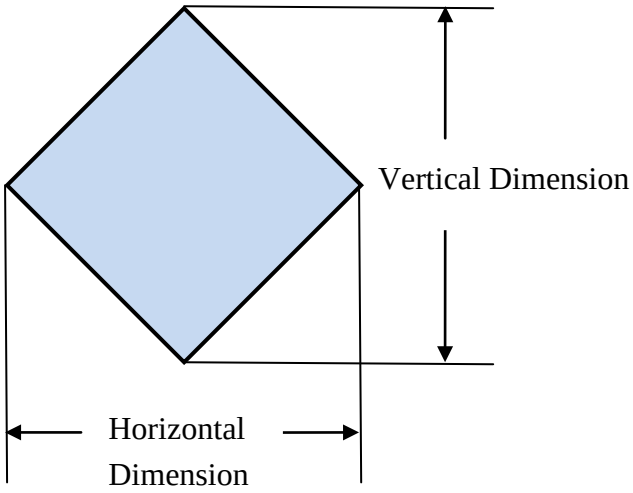

Figure 4.9: Two dimensions of the Vickers diamond indentation

4.4 Tensile Test

The tensile test samples were machined from as-received billet samples obtained from Hydro and RTA at dimensions specified by the ASTM-E8 standard (available in Appendix D).

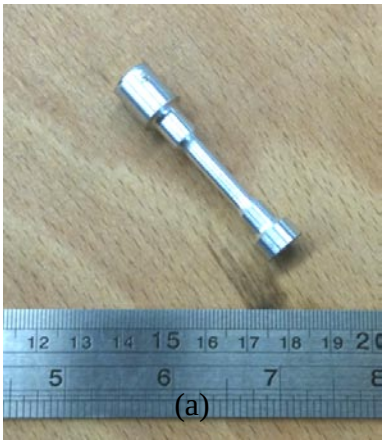

Figure 4.10: Machined tensile test sample

A RTA and a Hydro sample were put aside to determine the 'as received' tensile performance. The remaining tensile test samples were heat treated as per the procedure for hardness testing presented in Section 4.3.1. The temperature profiles obtained for thermocouple A and thermocouple B are presented in Appendix F.

A total of 72 samples were tested using a Tinius Olsen tensile tester shown in Figure **4.11**(a) to determine the mechanical properties of the material. The tensile tester provides measurement of the force and elongation of the tensile sample. Additionally, an extensometer measures the instantaneous diameter as shown in Figure **4.11**(b).

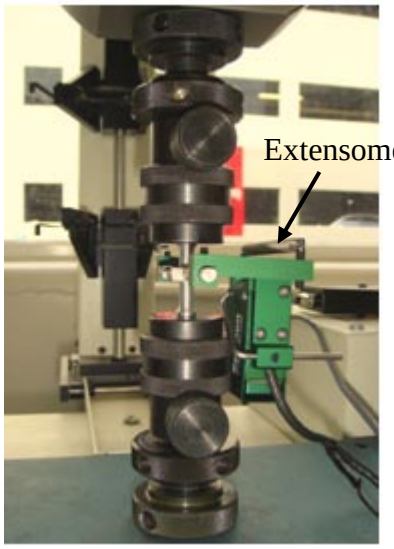

(a) (b)

Figure 4.11: (a) Tinius Olsen tensile tester; (b) Test sample clamping with extensometer

During each test, the sample applied load, elongation and diameter were monitored by a computer using Navigator. A typical 'engineering stress versus engineering strain plot' obtained from the Navigator software is presented in Figure **4.12**.

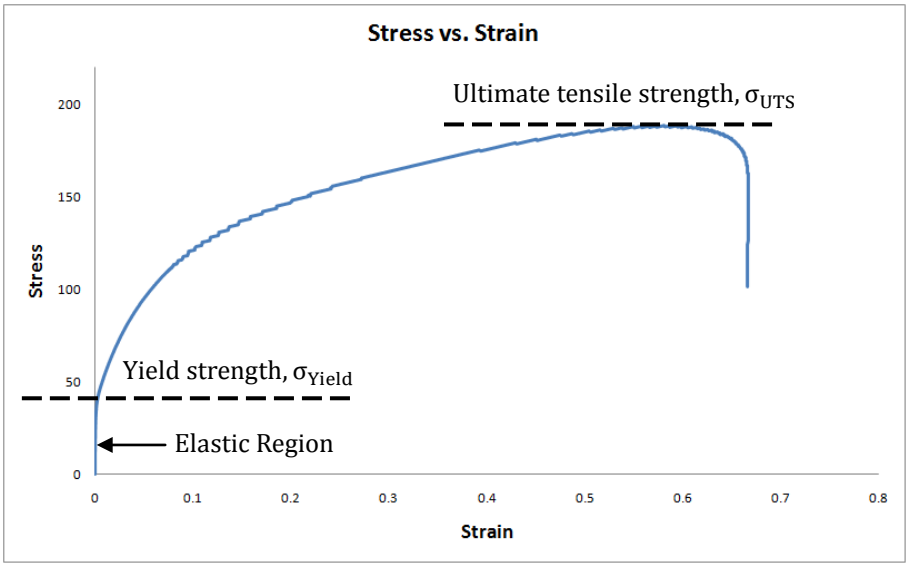

Figure 4.12: Typical stress vs. strain curve in tensile test

The testing involved taking a test sample with a fixed cross-sectional area, and then pulling it with a controlled, gradually increasing force until the sample changes shape or breaks as shown Figure 4.13.

Figure 4.13: Sample after tensile testing

The yield strength is then extracted from the curve using the offset method. A point is found on the strain axis of 0.2%, and then a line with a slope equal to the modulus of elasticity is drawn as presented in Figure **4.14**. The intersection of the line and the curve is recorded as the yield stress. The ultimate tensile stress is measured by obtaining the maximum engineering stress level reached during the tensile test.

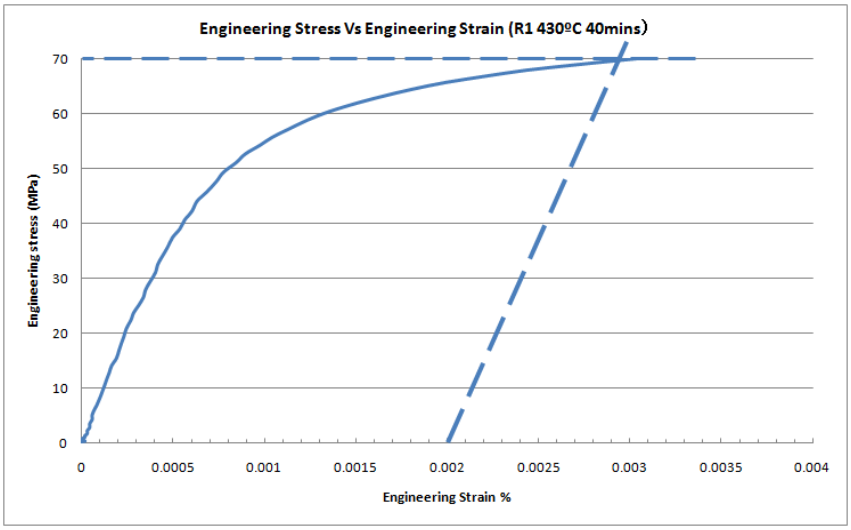

Figure 4.14: A tensile test graph showing measurement of Yield Strength

The true stress and true strain is then calculated using the engineering stress, engineering strain and the instantaneous diameter of the sample as inputs to Eq. 3.1 and

Eq. 3.2. The log of the true stress is plotted against the log of the true strain to determine the strain hardening exponent and intercept (log K). The final length of the sample is then measured (fracture length) to provide an indication of the material ductility.

4.5 Hot Compression Test (Gleeble Test)

Hot compression tests were carried out on the thermal-mechanical simulator, also called Gleeble tester, as shown in Figure **4.15**. This equipment is a computerised testing device that precisely and independently controls thermal and mechanical operation on a sample.

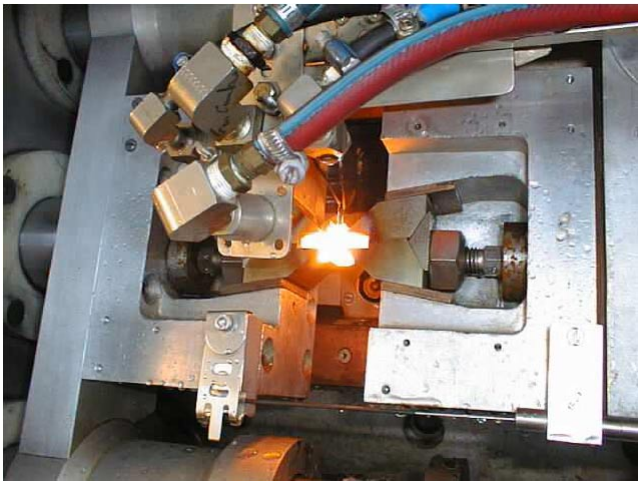

Figure 4.15: Gleeble Test Equipment - Hot deformation area [79]

The test sample is heated by its resistance to the flow of electrical current. Temperature monitoring and control were achieved using thermocouples spot welded to the surface of the sample within the work zone. A schematic drawing of the Gleeble test loading mechanism is illustrated in Figure **4.16**.

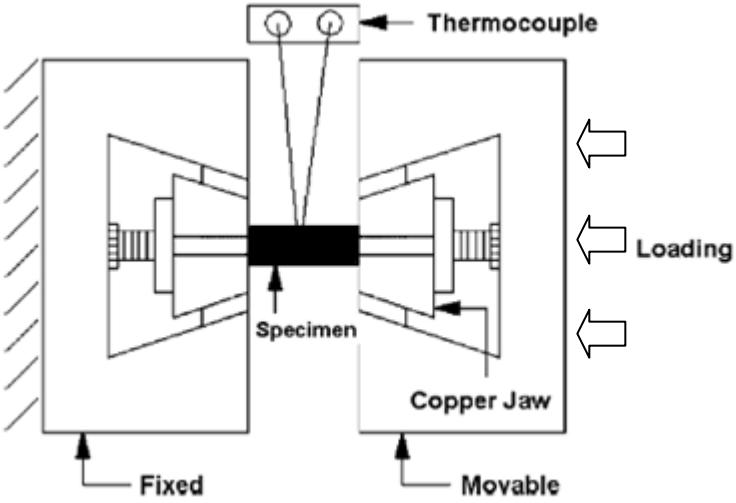

Figure 4.16: Schematic drawing of Gleeble test loading mechanism [79]

The cylindrical samples with 10mm in diameter and 15mm in height were machined from the homogenized test material. Convex depressions 0.2mm deep were machined on both ends of the samples in order to maintain the lubricant during compression tests. Figure **4.17** shows the standard Gleeble test sample. A drawing of the Gleeble test sample is provided in Appendix E.

Figure 4.17: Standard Gleeble test sample

The Gleeble test samples are heat treated following the procedure used for the hardness and tensile test samples (Section 4.3.1). The temperature records for thermocouple A and B are presented in Appendix F.

4.5.1 Strain Rate During Hot Deformation Test

The most common equation used to represent the strain rate $\dot{\varepsilon}$ in terms of the extrusion velocity is proposed by Feltham and is given by [77, 80]:

$$\dot{\varepsilon} = \frac{6 * V_R * D_B^2 * lnR}{D_B^3 - D_E^3} \qquad (4.1)$$

Where D_B and D_E are the billet and extrude diameters, V_R is the ram speed (ms^{-1}), R is the action ratio R = D_B^2/D_E^2 (R = 53.92 in this case).

Tutcher [78] noted that in practice the deformation zone semiangle varied with the extrusion ratio and by extensive optimization of the upper bound solution, established that the Feltham formulae should be modified:

$$\dot{\varepsilon} = \frac{6 * V_R * D_B^2 * (0.171 + 1.86\ lnR) * tan\ (38.7 + 6.9\ lnR)}{D_B^3 - D_E^3} \qquad (4.2)$$

The strain rate during the extrusion process in Fletcher Aluminium as shown in Section 1.1.5 can be determined by the Felthams' equation (V_R = 3m/min)

$$\dot{\varepsilon} = 5.18\ s^{-1}$$

Figure **1.12** shows a minimum production velocity of 0.33 s^{-1}. An average production velocity for the first phase of production is approximately 2 ms^{-1}. The Gleeble testing analysis will use a strain rate of 2 s^{-1} which corresponds to the production speed during this low speed period.

4.5.2 Gleeble Testing

The hot deformation behaviour of the heat treated RTA aluminum alloys was investigated by compression tests in the temperature range 330°C – 480°C and at a constant strain rate of 2 s^{-1} using the Gleeble-3500 system. An explanation of the selection of strain rate parameter is presented in Section 4.5.1.

Samples were re-heated in the Gleeble simulator to the required test temperature at 5°C/s. The testing temperature used for each test sample is the temperature used during the previous heat treatment. Figure 4.18 shows the temperature during the Gleeble tests at various testing temperatures. It is observed that the temperatures rise linearly to the testing temperatures within 90 seconds and remain constant until the end of testing. Each material was tested to a true strain of around unity at nominal strain rate of 2 s^{-1}, and temperatures between 330°C and 480°C. The strain was measured using quartz-tipped extensometer across the diameter of the sample.

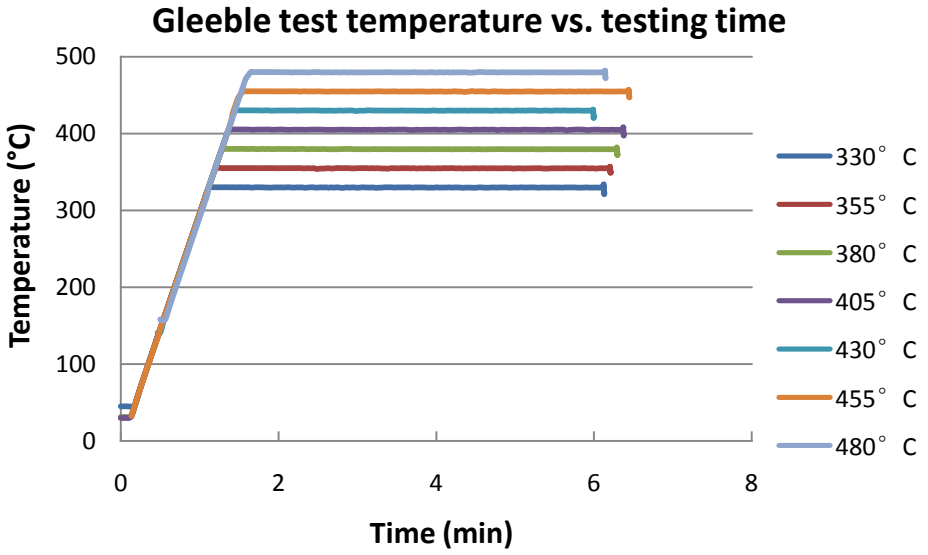

Figure 4.18: Temperature records during Gleeble test

Samples were compressed during the Gleeble test at a strain rate of 2 s^{-1} until each sample was half of its original length. The load and displacement were recorded every second by a computing system during the entire hot compression test. Figure **4.19** shows the deformed the Gleeble test sample.

Figure 4.19: Deformed Gleeble test sample

Load and displacement data obtained for each sample were converted into true stress – true strain curves. The true stress-strain curve of each sample was plotted under different temperatures. A typical stress – strain curve obtained from a Gleeble test is shown in Figure **4.20** where the stress rapidly approaches an initial flow stress and gradually increases to its peak flow stress. Initial flow stress and peak flow stress are determined by the same procedures as the yield strength and ultimate tensile strength obtained in tensile test respectively.

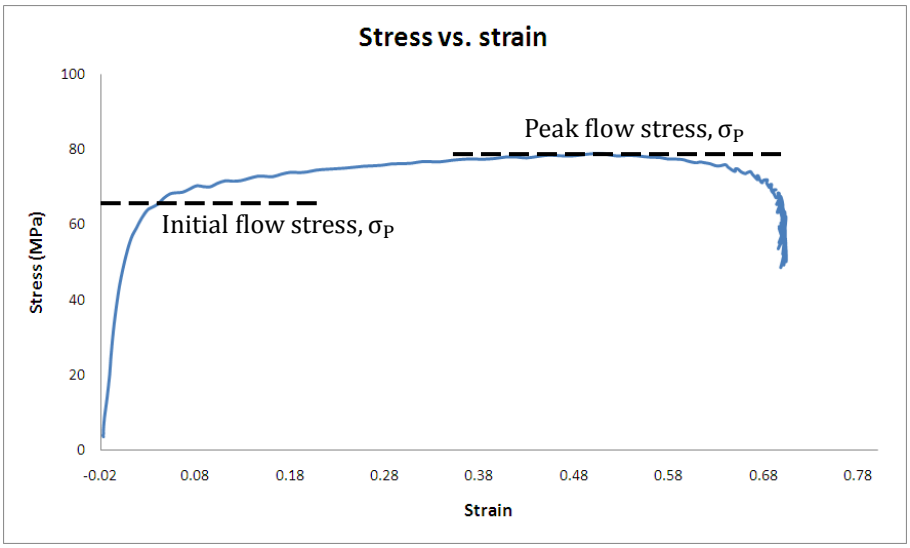

Figure 4.20: Typical stress vs. strain curve in Gleeble test

An introduction into the significance of the Z value is provided in Section 3.4. The peak flow stress, temperature and strain rate are used to determine the Z value. The 'Z'-value represents the compressive deformation capability of samples at elevated temperatures. The Zener Hollomon equation (Eq 3.6) has 3 unknown values; A, n, Q. Approximate values have been obtained from previous trials with a similar material which are provided in Table **4.2** below.

Table 4.2: Assumed Q, A, n values

	***Q* (KJ/mol)**	***A* (S^{-1})**	***n***
Assumed value	145000	2.409 X 10^{8}	3.55

The approximate values and values of strain rate, gas constant, temperature and peak flow stress values obtained from 30 experiments are used to determine optimal values A, n and Q. Iterative software code written by Joseph Robson [81], provided in Appendix J, uses the Nelder-Mead method to find constants which minimized error between the data and the Zener Hollomon equation (Eq. 3.6).

The remaining 5 experimental values are used to validate the values of A, n and Q for the material provided and to calculate Z. Once the results are used to obtain values of Q, A and n. Log (Z) values are determined, these provide an insight to the deformability of the material at different temperatures.

Chapter 5 Experimental Results

The following chapter presents results obtained from room temperature (hardness and tensile) and elevated temperature (Gleeble) testing, for a range of suppliers, heating temperatures and heating times.

5.1 Hardness

Hardness values of samples of billets from the two suppliers heated with different heating temperatures and heating times are presented in this section. The average hardness obtained for each sample is presented in Appendix G.

The hardness curves as a function of temperature are plotted for each heating time (15 – 85 mins). Figure **5.1** and Figure **5.2** present the results of hardness values versus temperature for Hydro and RTA samples respectively.

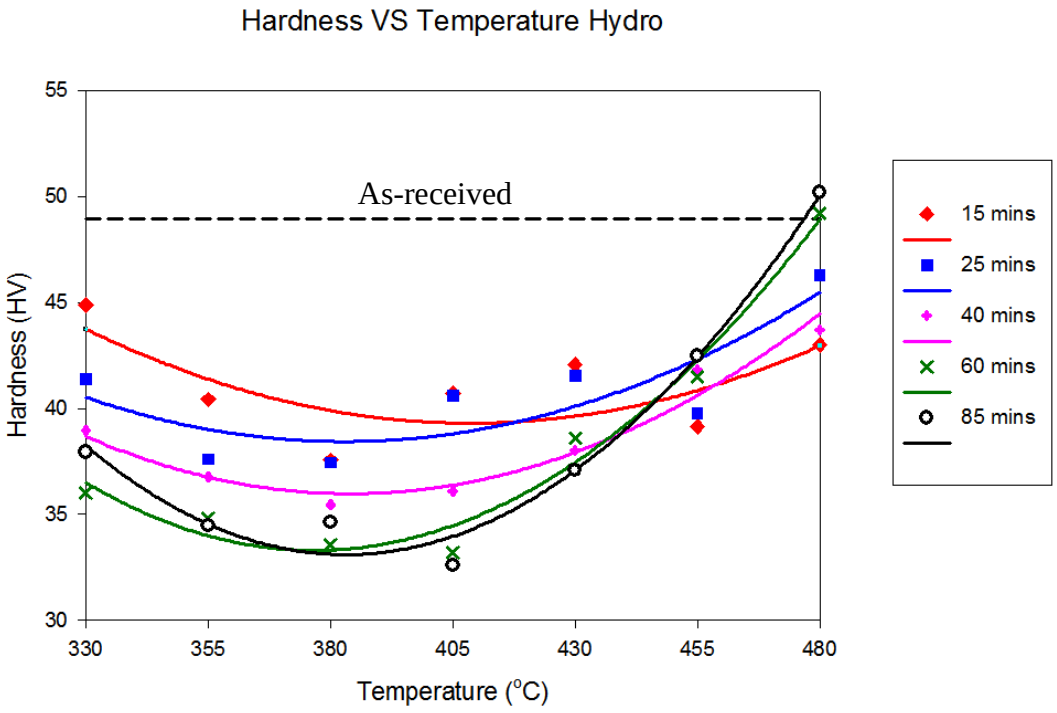

Figure 5.1: Hardness versus heating temperature (Hydro)

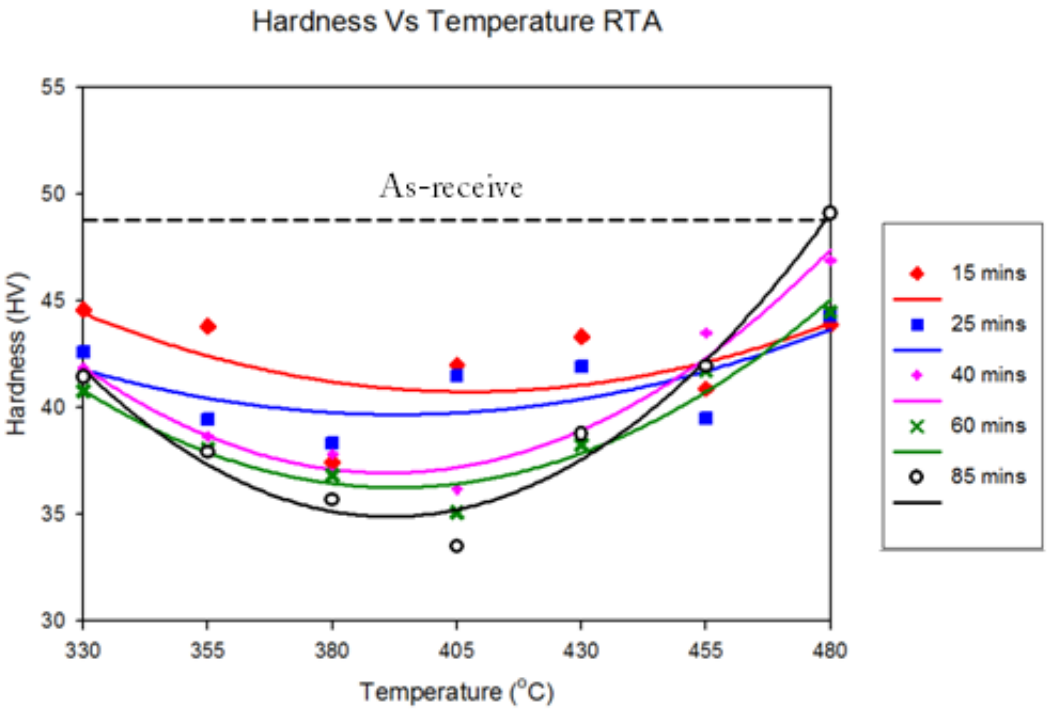

Figure 5.2: Hardness versus heating temperature (RTA)

The hardness value of the majority of heat treated samples is significantly lower than the as-supplied hardness value. Overall, the hardness for both RTA and Hydro first decreases as heating temperature increases, but then increases at temperature increases. The local minimum point is present in the vicinity of 380°C ~ 405°C for each heat treatment time and material. The absolute minimum is approximately 34 HV and is obtained at 405°C and at a long sample heating time (85 mins).

At approximately 455°C, the trends relating hardness to temperature are observed to intersect for both suppliers. At temperatures 330 to 430°C, maximum hardness values are observed at shorter heating times. However, at temperatures exceeding 455°C, maximum hardness value is observed at longest heating time. The hardness value of the material reaches the as received hardness at a heating temperature of 480°C and heating time of 85 minutes. The trends observed, apply to both Figure **5.1** and Figure **5.2**. It is therefore realised that the plots of hardness value for both Hydro and RTA samples are similar.

Figure **5.3** and Figure **5.4** present the results of the hardness analysis using an alternative style; where hardness is plotted as a function of heating time at various heating temperatures.

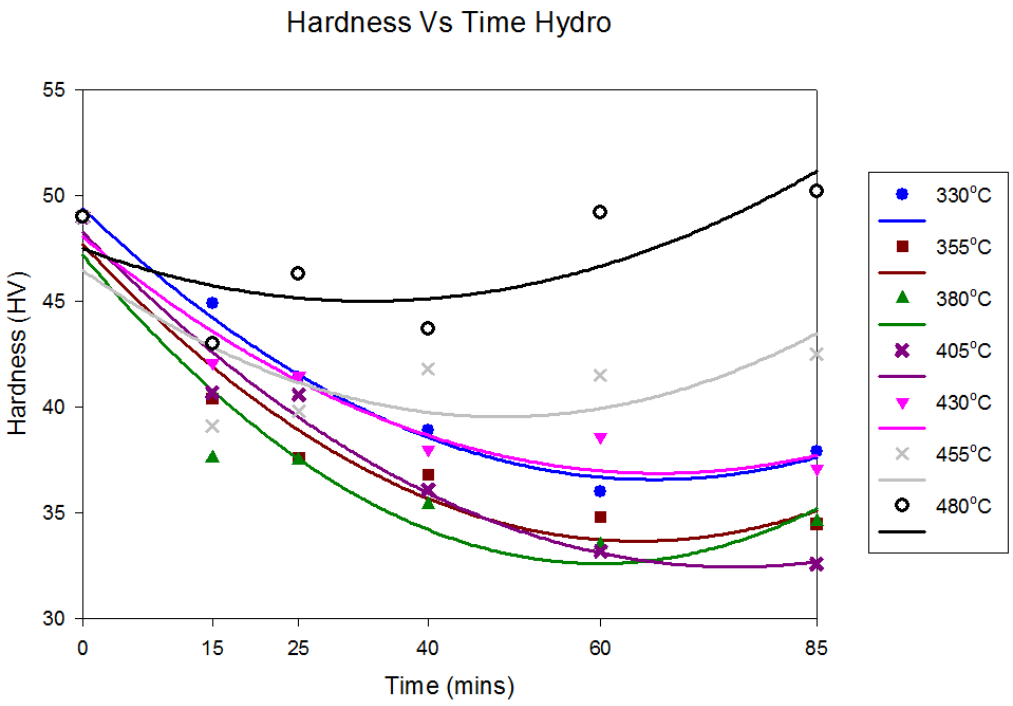

Figure 5.3: Hardness versus heating time (Hydro)

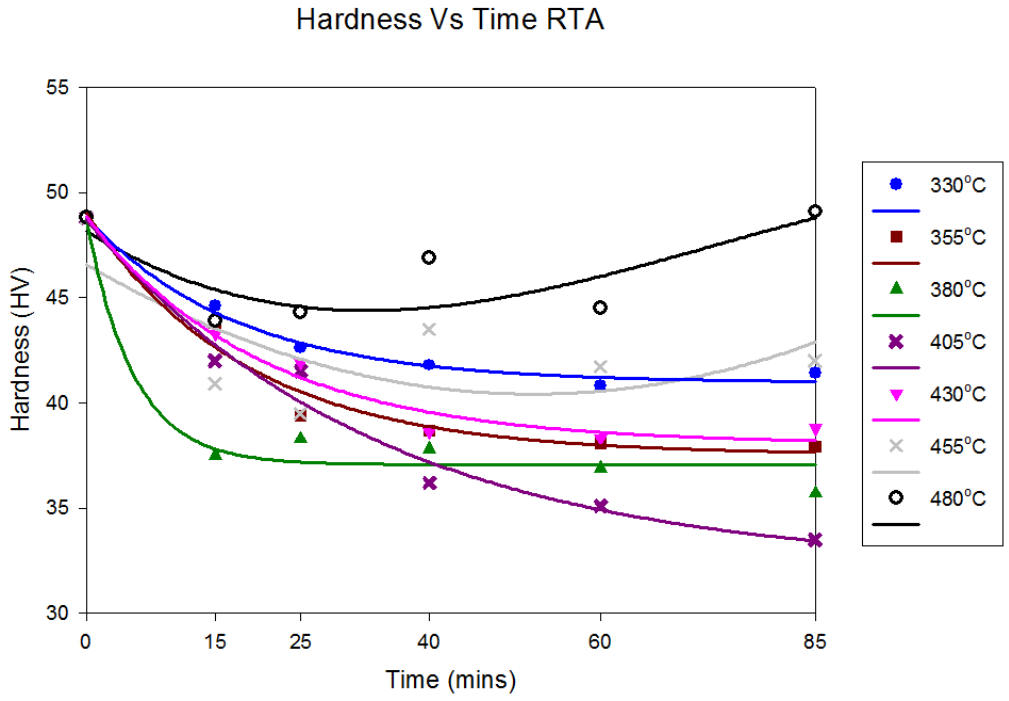

Figure 5.4: Hardness versus heating time (RTA)

The overall trend observed for the hardness versus heating time relationship is an exponential decay at all temperatures (except at $T_{heating}$ = 455 and 480°C).

5.2 Tensile Properties

The following section presents tensile test properties for heat treated and as received samples. Data obtained for yield strength, ultimate tensile stress, strain hardening exponent and elongation coefficients are presented in Appendix H.

Tensile tests were performed on the as-received RTA and Hydro materials to investigate their deformation behaviour and provide a standard with which to compare heat treated measurements. Table **5.1** shows the yield strength, ultimate tensile strength and strain hardening exponent obtained for each material. The two supplied materials have similar mechanical properties.

Table 5.1: Tensile test results of as-received samples

Tensile Property	Hydro	RTA
Yield strength (MPa)	68	64
UTS (MPa)	155	161
Strain hardening exponent	0.26	0.28

5.2.1 Yield Strength

The yield strength calculated from the tensile tests of heat treated samples is presented as a function of heating time and temperature in Figure **5.5** to Figure **5.8** below. Yield strength values for the two materials as a function of heating temperature are presented in Figure **5.5** and Figure **5.6**. Comparisons between these figures show that RTA and Hydro have very similar yield strength values for the same heating condition.

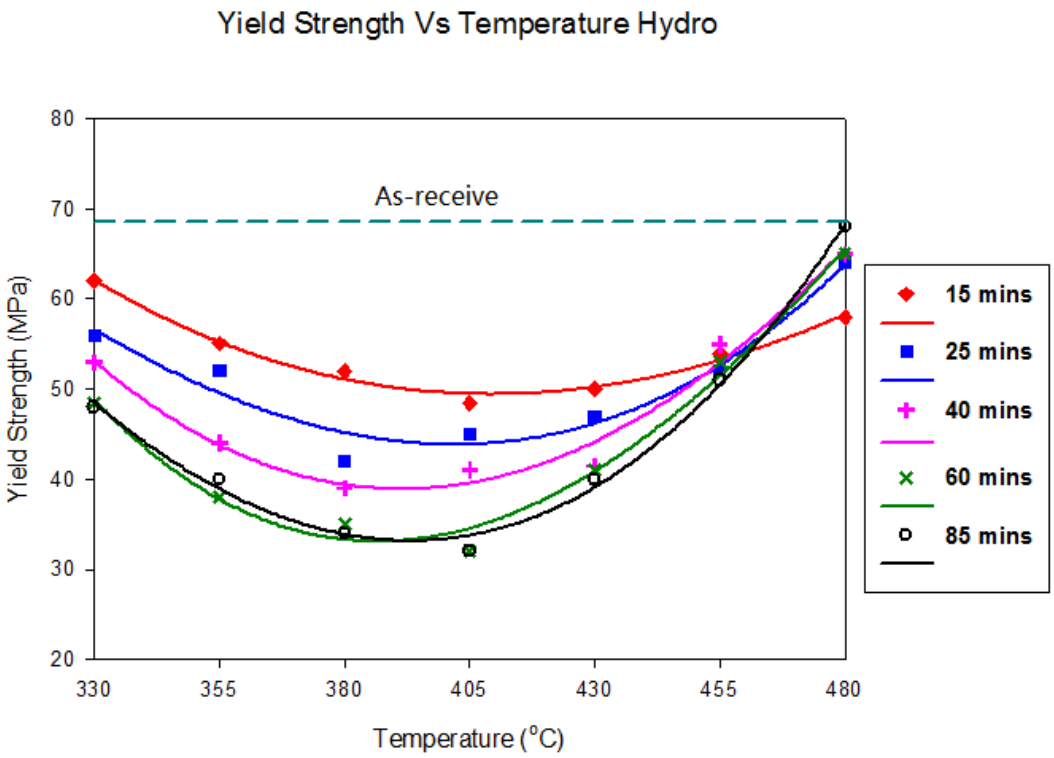

Figure 5.5: Yield strength versus heating temperature (Hydro)

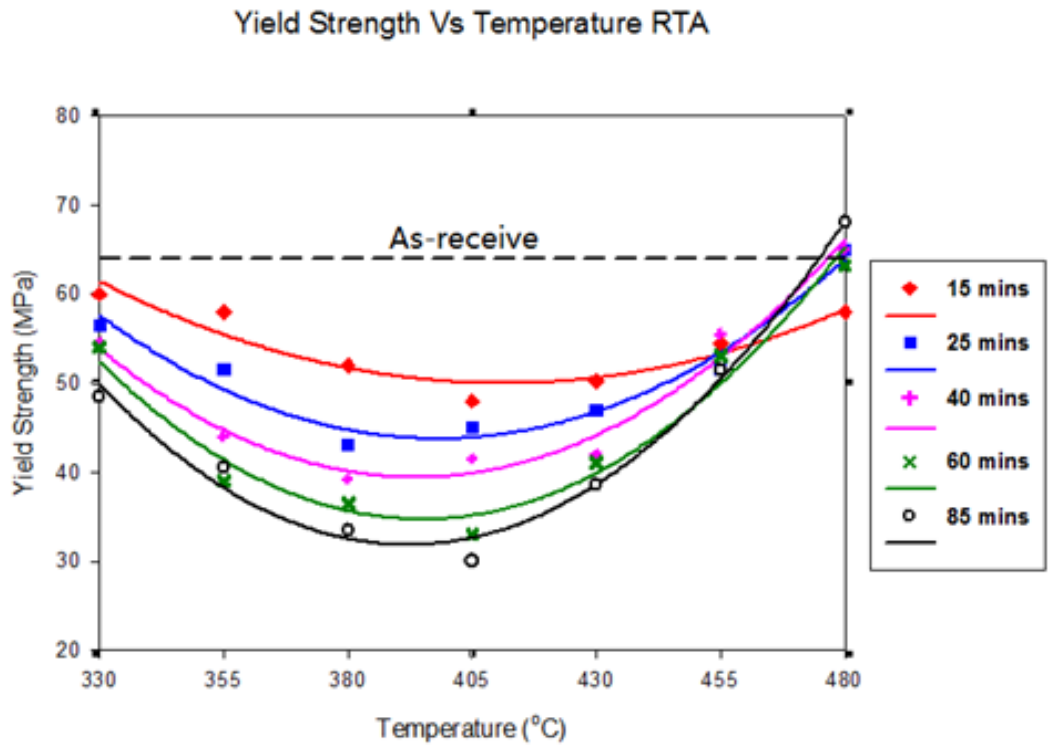

Figure 5.6: Yield strength versus heating temperature (RTA)

Similar to the trend of hardness versus heating temperature described previously (Section 5.1), a local minimum point is present in the vicinity of 380°C ~ 405°C for all the heat treated samples. The absolute minimum is approximately 30 MPa and is obtained at 405°C and at the longest heating time (85 minutes).

At approximately 455°C, the trends relating yield strength to temperature are observed to intersect for both cases. At temperatures below 455°C, maximum yield strength values are observed at the short heating times. At temperatures exceeding 455°C, minimum yield strength values are observed at shorter heating times.

Yield strength for the two materials as a function of heating time are shown in Figure **5.7** and Figure **5.8**. Additional to the observations made in the previous section, it is also observed that the yield strength stabilises at longer heating times.

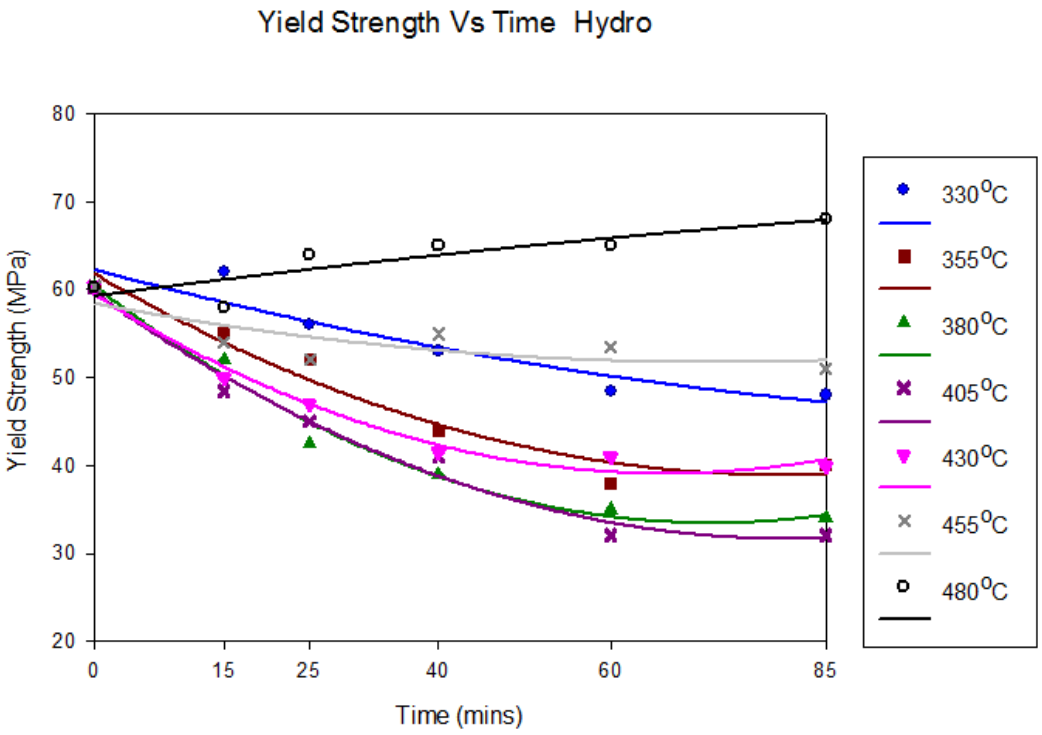

Figure 5.7: Yield strength versus heating time (Hydro)

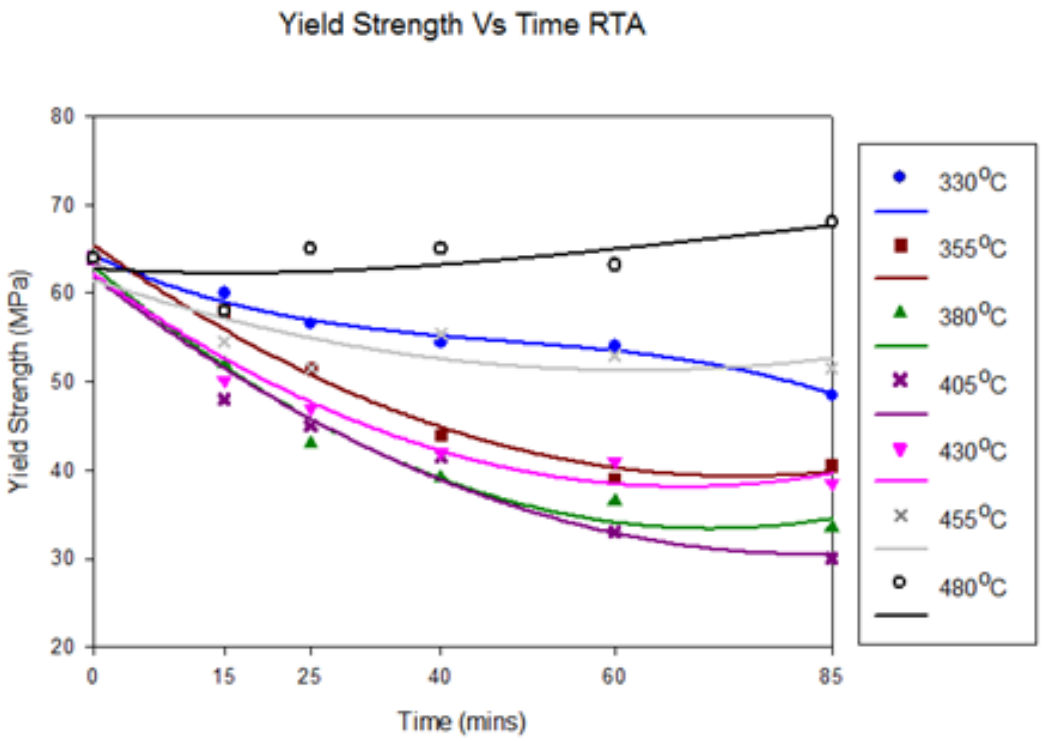

Figure 5.8: Yield strength versus heating time (RTA)

5.2.2 Ultimate Tensile Strength (UTS)

The UTS for both as-received materials are 155 MPa and 161 MPa for Hydro and RTA respectively. The following content will present the plots of UTS values against the heating temperature and heating time. UTS values for the two materials have been plotted against the heating temperature as illustrated in Figure **5.9** and Figure **5.10**.

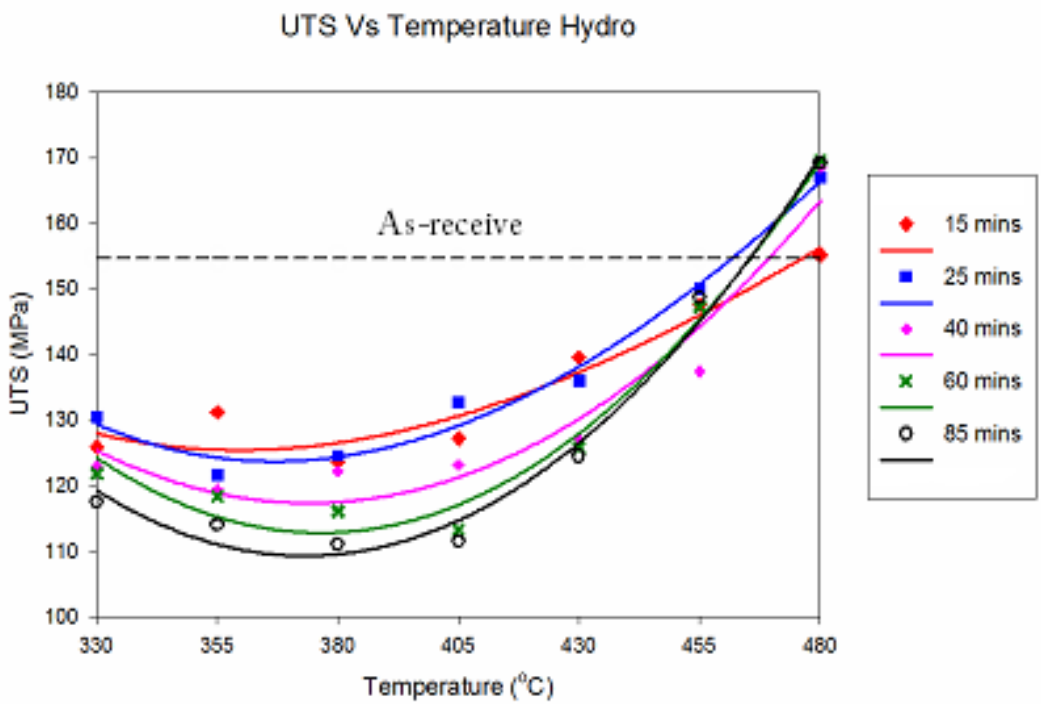

Figure 5.9: UTS versus heating temperature (Hydro)

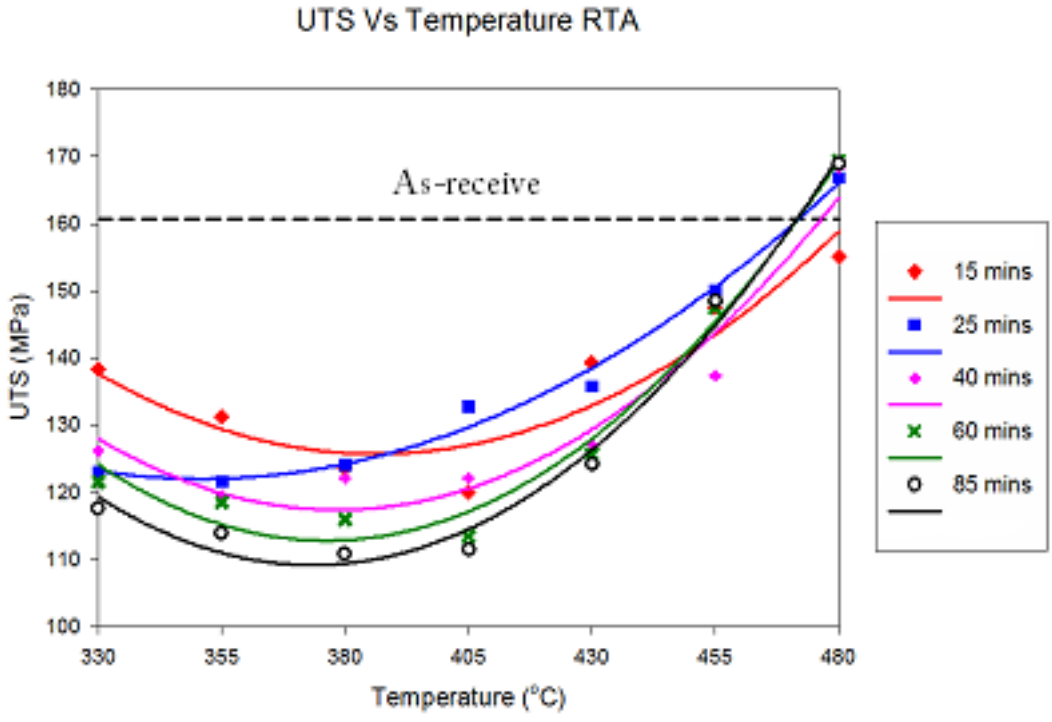

Figure 5.10: UTS versus heating temperature (RTA)

The ultimate tensile strength curves have a parabolic shape with a minimum near 405°C, which is similar to the yield strength curves presented in Section 3.2. However, the

curves differ as the minimum value for UTS is at a lower temperature, and the stress magnitude is significantly larger. The UTS curves for each supplier are nearly identical.

As shown in Figure **5.9** and Figure **5.10**, the absolute minimum UTS of 110 MPa is observed at a heating temperature of 380°C at a heating time of 85 minutes. The minimum is much lower than the as received sample UTS. There is insignificant change in the UTS at heating temperatures between 330°C and 380°C. At temperatures higher than 380°C, an almost linear increase in UTS is observed for increments in heating temperature.

The local maximum UTS values for each profile were obtained at 480°C and the absolute maximum was attained at a heating time of 85 minutes. An UTS of 170 MPa was obtained for all samples heated at 480°C for longer than 15 minutes as shown in Figure **5.11** and Figure **5.12**.

UTS values for the two materials have been plotted against the heating time as illustrated in Figure **5.11** and Figure **5.12**. An exponential decay of UTS is observed at heating temperatures between 330°C and 430°C.

At temperatures near 455°C, despite changes in the heating time, UTS values are constant. At temperatures exceeding 455°C, UTS values increase as a function of heating time.

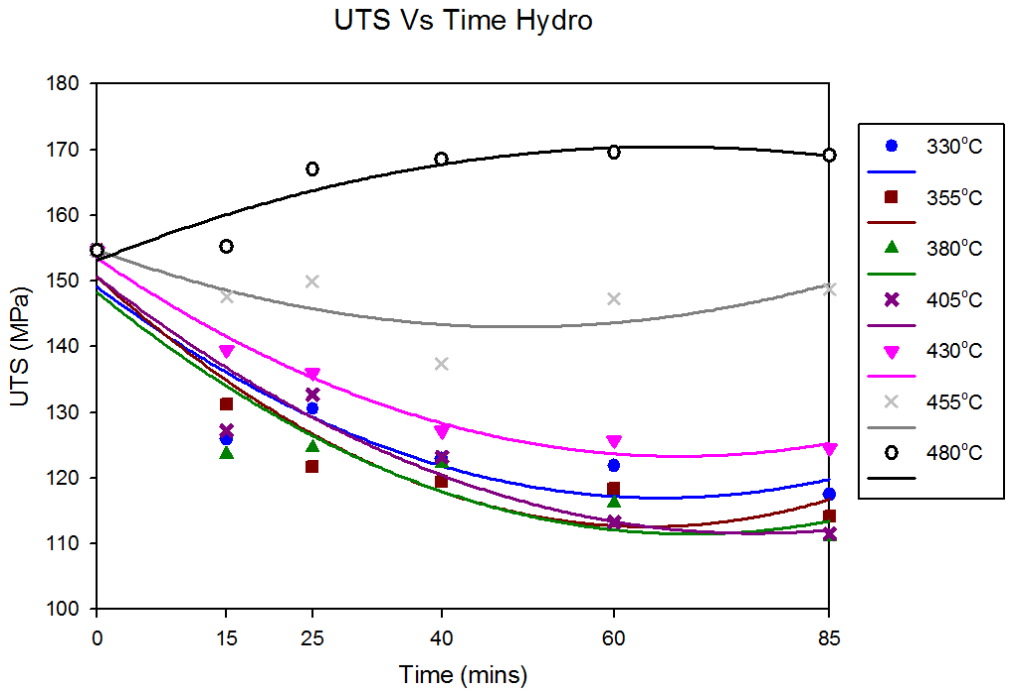

Figure 5.11: UTS versus heating time (Hydro)

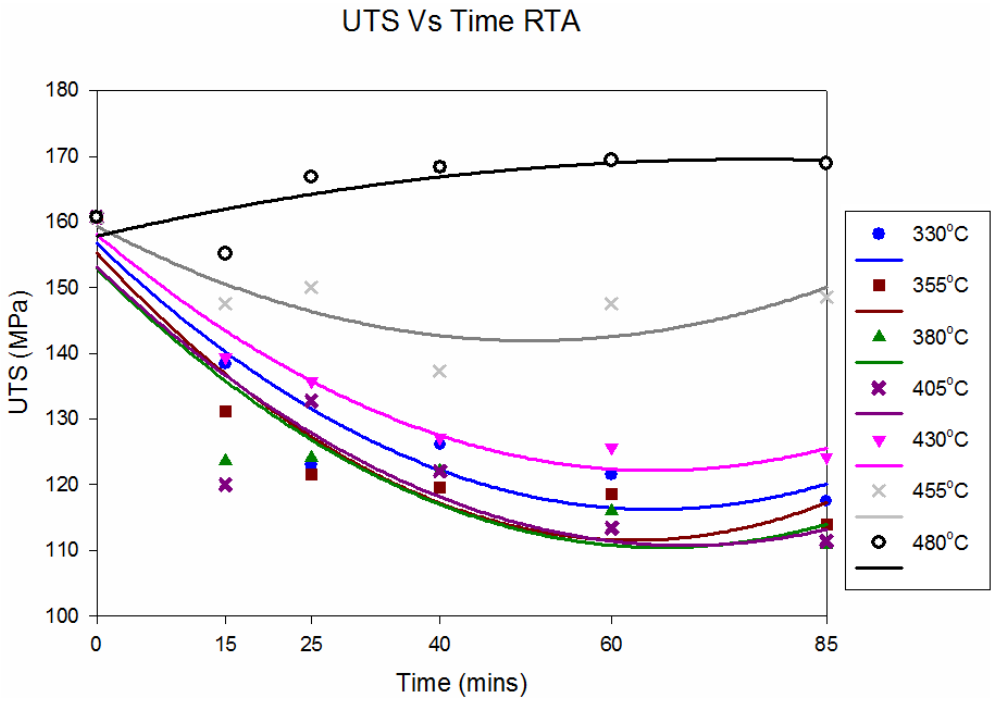

Figure 5.12: UTS versus heating time (RTA)

5.2.3 Strain Hardening Exponent (n value)

The strain hardening exponent is plotted with heating temperature in Figure **5.13** and Figure **5.14**, where the strain hardening exponent data is presented in Appendix H.

The strain hardening exponent is expected to be constant when the shape of the ultimate tensile strength as a function of temperature and time is exactly the same as yield strength as a function of temperature and time. Figure **5.13** – Figure **5.16** show an increase in strain hardening exponent and therefore confirm an increase in the significance of strain hardening, when the temperature is increased.

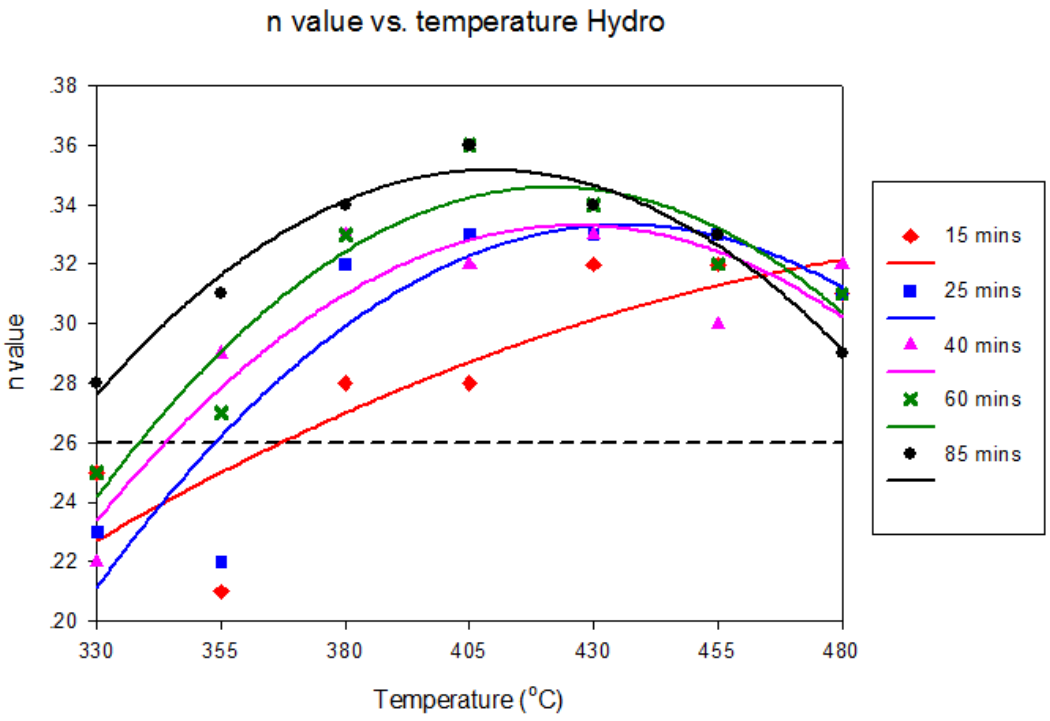

Figure 5.13: n value versus heating temperature (Hydro)

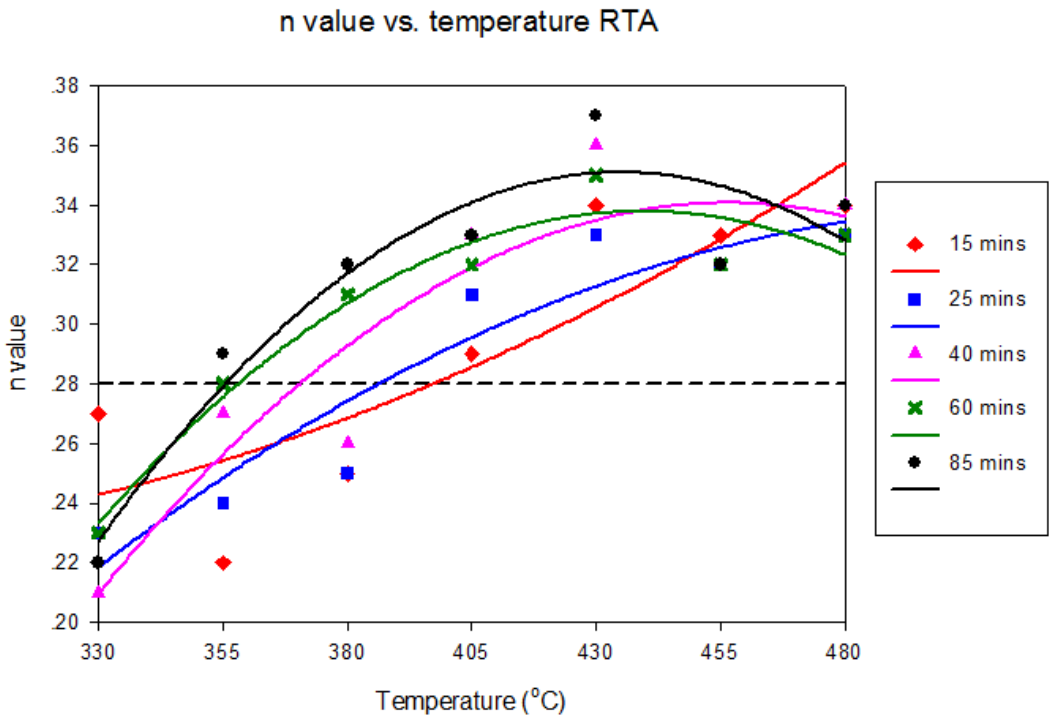

Figure 5.14: n value versus heating temperature (RTA)

The data for the n value at a 15 minute heating time is significantly scattered from its trend line as data for this region is susceptible to measurement errors. The variation in

the true stress and strain data has been influenced by the selection of the linear region used to calculate the n value. The linear region is difficult to determine consistently though this variation is characteristic of the acquisition of n value, and is due to variation in the strain at the beginning of the linear region and breaking strain.

At temperatures between 330°C and 380°C, the n values obtained for the Hydro samples are larger than those for RTA samples.

At heating times greater than and equal to 25 minutes, a negative parabolic relationship is observed where the local maximums for each heating time are observed at temperatures between 405°C and 430°C. Absolute maximum n values are observed at a heating time of 85 minutes, and heating temperature near 430°C.

Strain hardening exponent (n value) for the two materials are plotted against heating time at various heating temperatures in Figure **5.15** and Figure **5.16**. The results show that an increase in the heating time is observed to cause a small but detectable change in the n value, and a large variation of n value from the presented trend lines.

The plots of RTA and Hydro are similar although the shape of the 380°C heating time n value profile shifts position and shape.

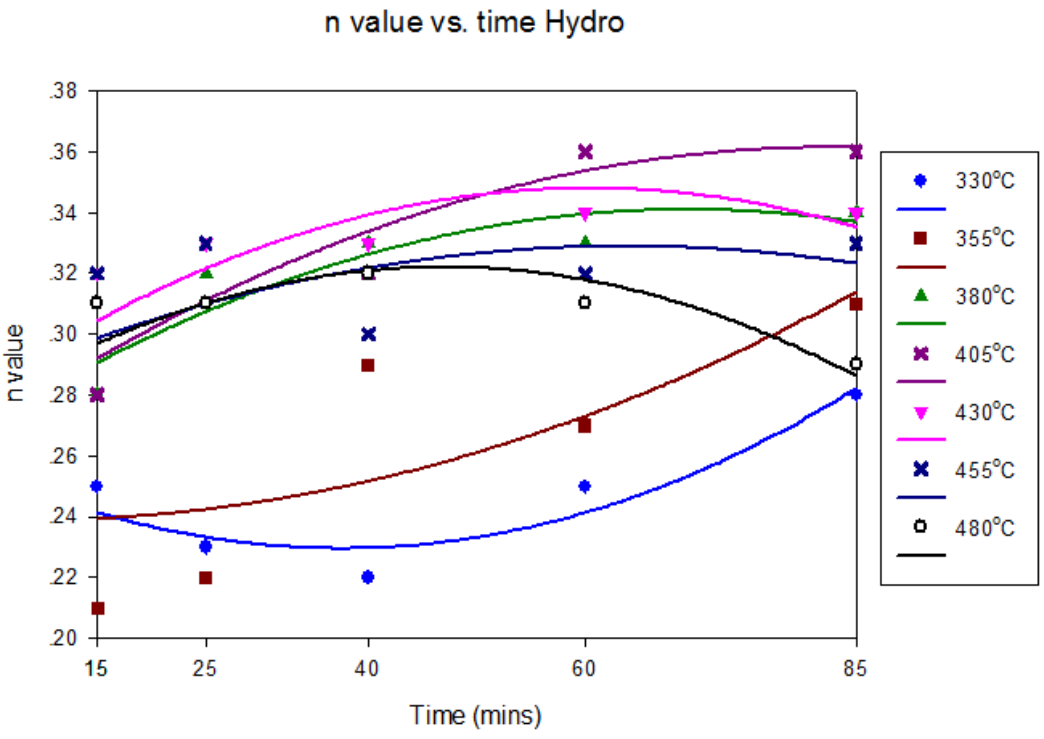

Figure 5.15: n value versus heating time (Hydro)

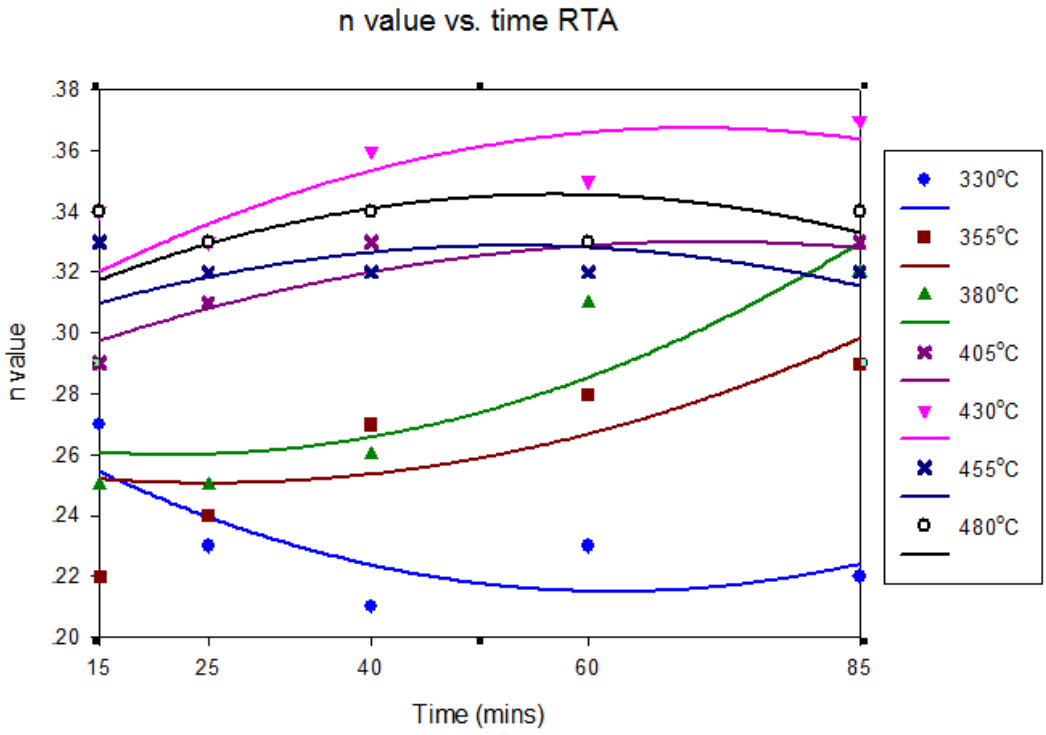

Figure 5.16: n value versus heating time (RTA)

5.3 Evaluation of Hot Deformation Performance (Gleeble Test)

The data obtained for all hot deformation samples are presented in Appendix I. Initial flow stress (similar to yield stress) and peak flow stress (similar to ultimate tensile stress) was then calculated from the flow stress curves. The Zener-Hollomon value is then calculated from testing parameters and the flow stress. The results are presented in the following section.

5.3.1 Initial Flow Stress

Initial flow stresses for the RTA material are plotted as a function of heating temperature in Figure **5.17**. A linear decrease in the initial flow stress is observed as heating/testing temperature increases. However, there is significant variation around the linear trend. There are challenges associated with accurate measurement of the stress and uncertainty in these measurements may be significant. A challenge is the oscillation of flow stress due to the switching dominance of work hardening and softening behaviours. The maximum n value is 53 MPa at 330°C for 25 minutes and the minimum n value is 18 MPa at 480°C for 25 mins.

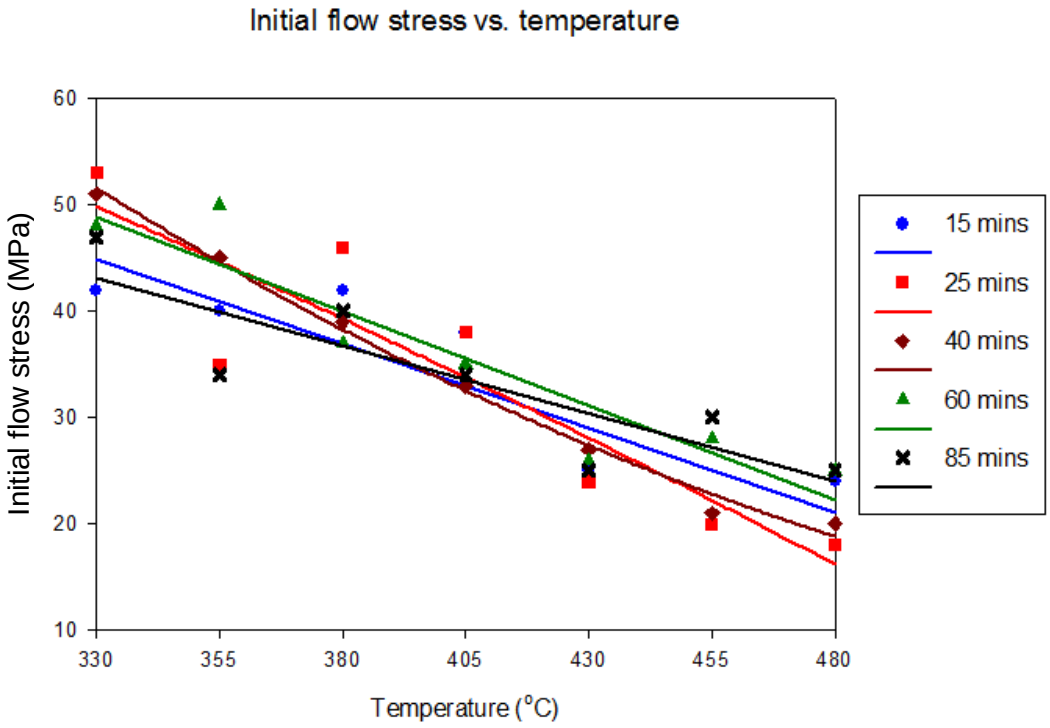

Figure 5.17: Initial flow stress versus heating temperature (RTA)

Figure **5.18** illustrates the initial flow stress versus the heating time at various heating temperatures. The initial flow stress is constant for changes in heating time (disregarding large measurement variations).

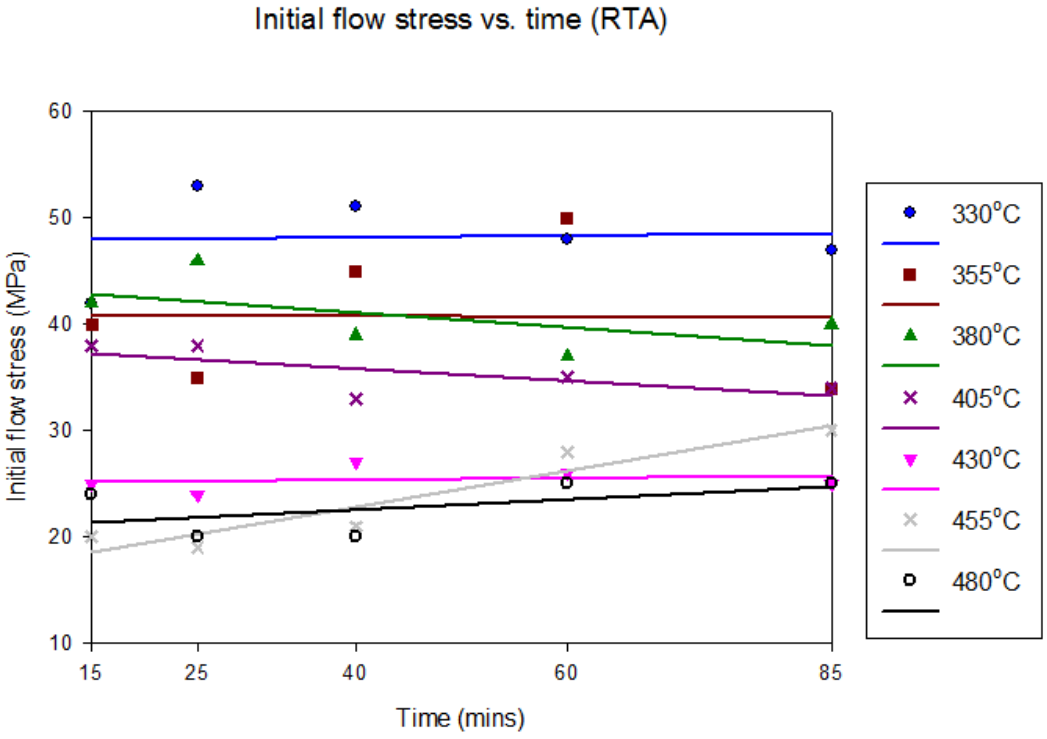

Figure 5.18: Initial flow stress versus heating time (RTA)

5.3.2 Peak Flow Stress

Peak flow stress is obtained from the true flow stress – true strain curve, and is the maximum true flow stress encountered during flow stress measurement. The following content will present the effect of heating/testing temperature on peak flow stress.

The peak stresses for the alloy are shown in Figure **5.19** as a function of deformation temperature at 2 s^{-1} where the flow stress is observed to decrease as heating temperature is increased. The absolute maximum flow stress is 86 MPa at 330°C for 15 minutes and the absolute minimum flow stress is 37 MPa at 480°C for 85 minutes.

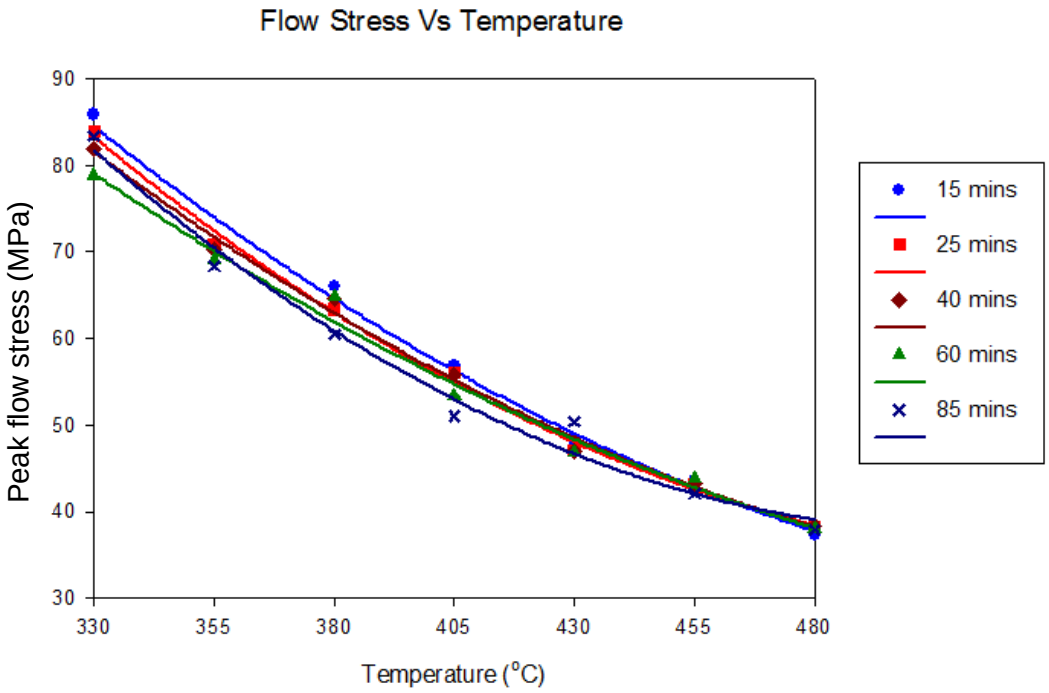

Figure 5.19: Flow stress versus heating temperature (RTA)

Peak flow stress values for RTA material have been plotted against the heating time as illustrated in Figure **5.20**. It is observed that there is negligible effect of heating time on flow stress.

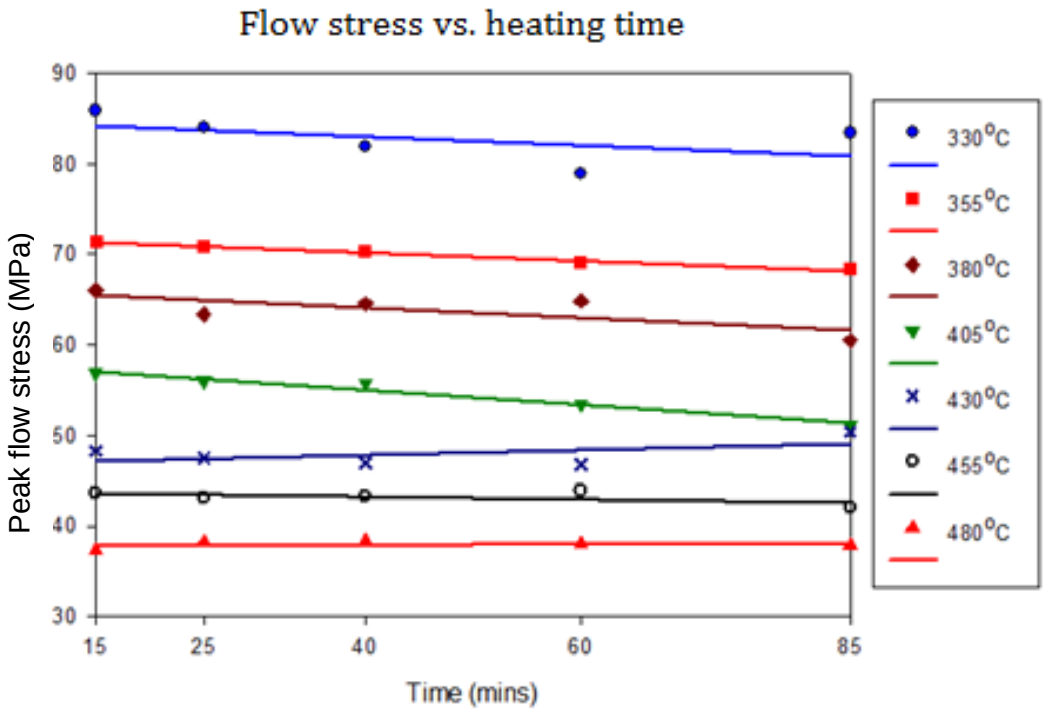

Figure 5.20: Flow stress versus heating time (RTA)

5.3.3 Zener-Hollomon Value

Section 3.4 provides a brief review of the Zener-Hollomon value (Z-value). Matlab software, presented in Appendix J, begins with assumed Q, A and n values. Flow stress data obtained at various deformation temperatures (except for 40 minute heating time) is then used to determine the final Q, A, n values that optimize the accuracy of Eq. 3.6.

The calculated Q, A, n values are shown in Table **5.2**.

Table 5.2: Calculated Q, A, n values

	***Q* (J/mol)**	***A* (s^{-1})**	***n***
Estimated value	145000	2.409×10^{8}	3.55
Calculated value	132593.02	2.89×10^{8}	2.60

The *Z* value is determined using calculated values of Q, A and n and measured values of temperature and flow stress obtained at a heating time of 40 minutes, as shown in Table **5.3**.

The validity of the calculated A, n, and Q values is tested by the comparison of Z_1 and Z_2. There is a small percentage difference between Z values.

$$Z_1 = \dot{\varepsilon}\, exp\left(\frac{Q}{R\,T}\right) \qquad (5.1)$$

$$Z_2 = A\left(sinh(\alpha\,\sigma)\right)^n \qquad (5.2)$$

Log Z value can be used to compare the extrudability of the test material in each heating and testing condition. Heating time has previously been shown to have negligible effect on the flow stress. Therefore, values of Z are calculated for a range of temperatures only.

Hence, the RTA materials after the average heating time 40 minutes are used to compare each other.

Table 5.3: Ln Z values under different deformation temperatures for 40 minutes heating time, (Unit: s^{-1})

T (°C)	σ (Mpa)	Z_1	ln Z_1	Z_2	ln Z_2
330	**81.89**	6.13 X 10^{11}	27.14	6.90 X 10^{11}	27.26
355	**70.30**	2.14 X 10^{11}	26.09	1.77 X 10^{11}	25.90
380	**64.56**	8.09 X 10^{10}	25.12	9.02 X 10^{10}	25.23
405	**55.84**	3.29 X 10^{10}	24.22	3.22 X 10^{10}	24.20
430	**46.98**	1.42 X 10^{10}	23.38	1.12 X 10^{10}	23.14
455	**43.15**	6.53 X 10^{9}	22.60	7.04 X 10^{9}	22.67
480	**38.38**	3.16 X 10^{9}	21.87	3.91 X 10^{9}	22.09

The natural log of Z is plotted against heating temperature in a continuous decrease is observed as the heating temperature increases. The maximum Ln Z value is 27 s^{-1} at 330°C and the minimum Ln Z value is 22 s^{-1} at 480°C.

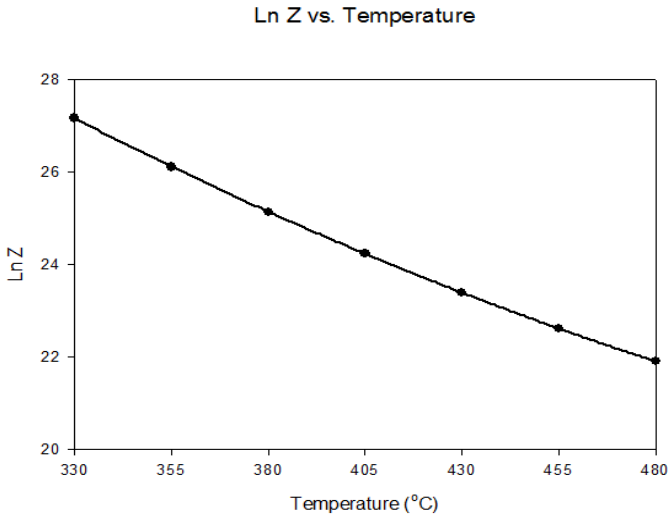

Figure 5.21: Ln Z versus Temperature (heating time of 40 minutes)

Chapter 6 Discussion

The results presented in Chapter 5 will be analysed to determine the correlation between hardness and tensile results. Overall, all the test samples have different thermal histories, and thus have different precipitate sizes and distributions (i.e. Mg_2Si). Therefore, depending on its specific heat treatment, each test sample can behave differently during experimentation.

Additionally, several strengthening mechanisms are analysed with reference to the results and phase transformation literature where an adjustment to the phase transformation diagram is suggested in response to the yield and ultimate tensile strength data. Gleeble test results will also be analysed to determine hardening and softening behaviour during billet deformation at elevated temperatures. The flow stress parameters are then analysed to provide the parameters which are expected to minimise extrusion force in context with limitations to ensure product quality.

6.1 Relationship between Hardness and Tensile Test Results

The Vickers hardness value, yield strength (YS) and ultimate tensile strength (UTS) were plotted against heating temperature and time in Figure **5.1** to Figure **5.12** where the profiles for Hydro and RTA billet materials are similar. Additionally, hardness and tensile strength measurements are expected to have a high degree of correlation as already discussed in literature review (Section 3.3). The correlation is investigated further in this research by plotting: YS versus hardness, UTS versus hardness (Figure 6.1 – Figure **6.6**) and determining the correlation coefficient.

6.1.1 Correlations between Hardness and Tensile Test Results

A good correlation was observed between hardness and YS ($R^2 \approx 0.82$ and 0.81 for Hydro and RTA respectively) and a lesser correlation was observed between hardness and ultimate tensile strength ($R^2 \approx 0.75$ and 0.67 for Hydro and RTA respectively) as shown in Figure 6.1 to Figure 6.4. The relationships of hardness with YS and UTS are shown in Eq. 6.1 – Eq. 6.4 below.

$$\sigma_Y = 2.1 \times hardness\ value - 32.8\ (Hydro) \quad (6.1)$$

$$\sigma_Y = 2.5 \times hardness\ value - 54.3\ (RTA) \quad (6.2)$$

$$\sigma_{UTS} = 3.5 \times hardness\ value - 6.6\ (Hydro) \quad (6.3)$$

$$\sigma_{UTS} = 4.1 \times hardness\ value - 35.7\ (RTA) \quad (6.4)$$

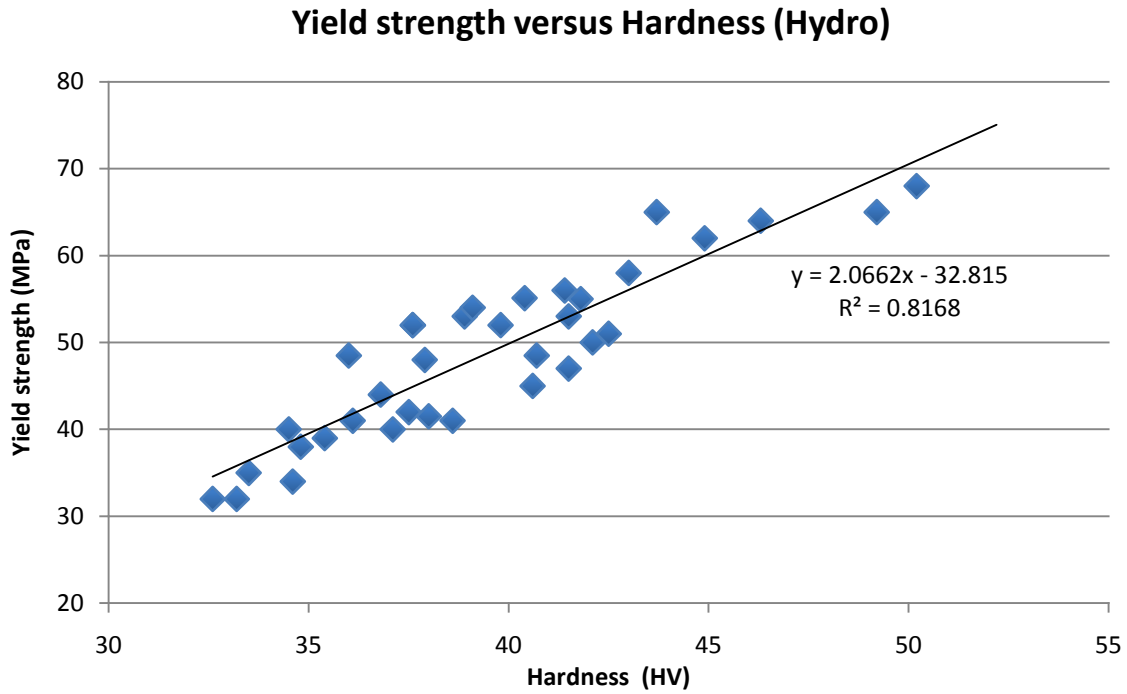

Figure 6.1: Yield strength versus hardness (Hydro)

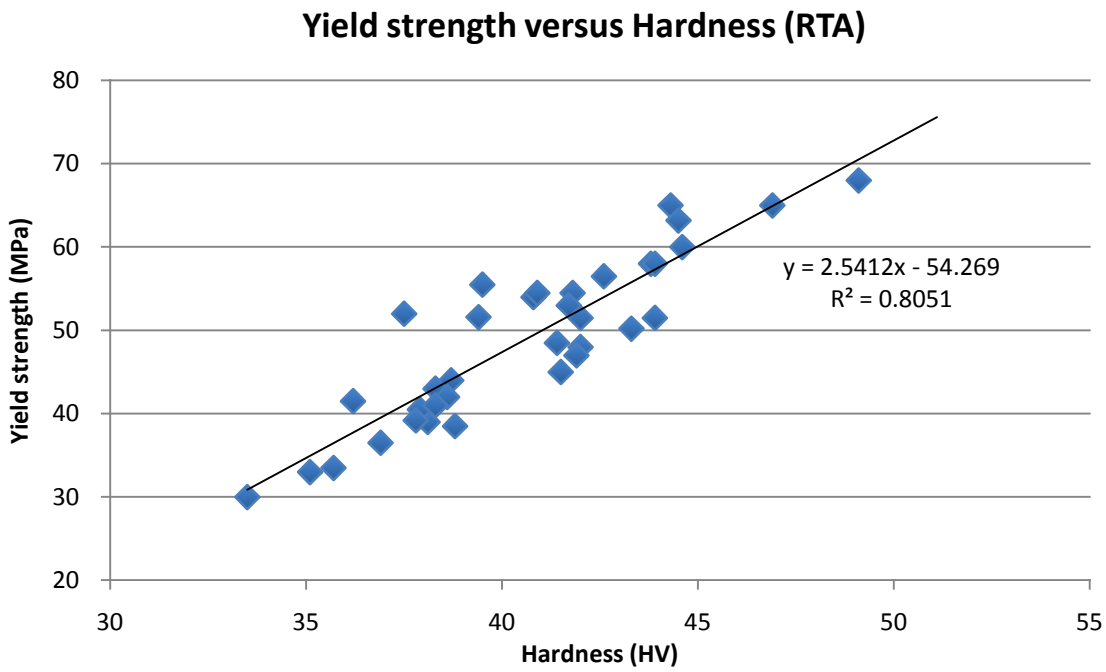

Figure 6.2: Yield strength versus hardness (RTA)

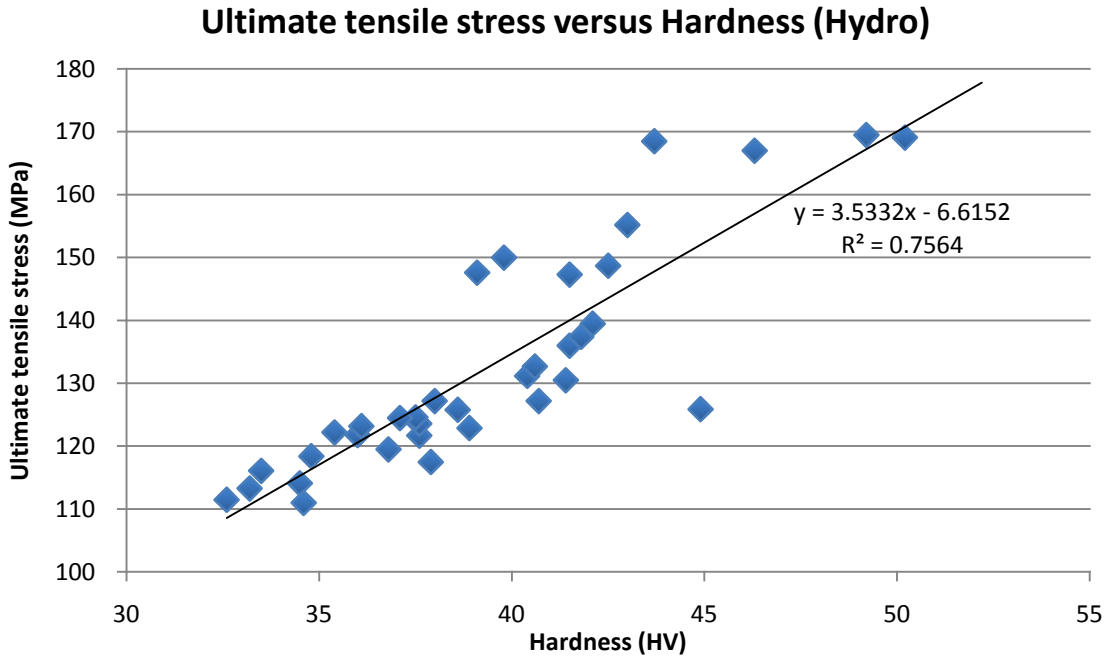

Figure 6.3: Ultimate tensile stress versus hardness (Hydro)

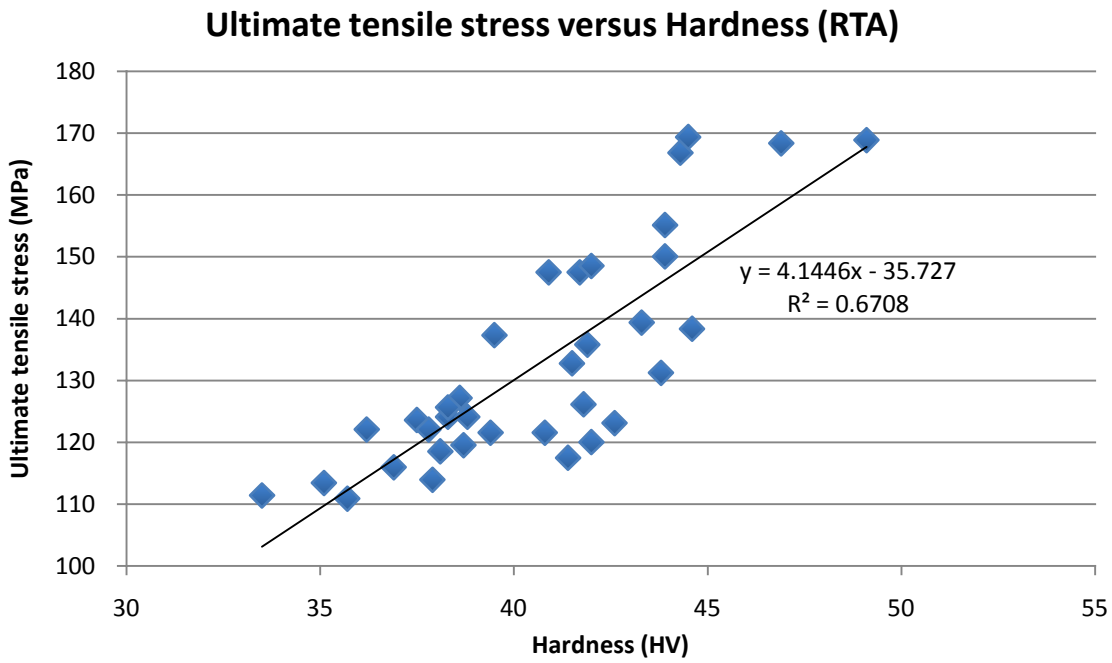

Figure 6.4: Ultimate tensile stress versus hardness (RTA)

The relationship between the hardness and YS or UTS is not simple. The constants for the relationships in Eq. 6.1 and Eq. 6.2 are different, where these tests used different samples materials, but the same test sample geometries, heat treatment histories, sampling rates and testing procedures. The different constants in Eq. 6.1 – Eq. 6.2 are only attributable to differences in material composition of Hydro and RTA materials due to the constancy of all other parameters. Additionally, the material composition is the only difference between Eq. 6.3 and Eq. 6.4 and therefore influences the UTS against hardness relationship.

The deformation process during tensile testing differs to the hardness testing deformation process. During a tensile or compressive test, the material within the gauge section undergoes nominally uniform deformation. Hardness testing involves plastic flow concentrated in the region below the indentation vertex, combined with elastic deformation outside of this region. It also can accommodate a part of the volume loss caused by the indentation. Directly below the indentation, the density of particles is forced to increase, compared to regions away from the indentation. The complexity of the deformation process during hardness testing means that the hardness cannot simply translate to tensile test values (YS or UTS).

Variation in hardness measurements can contribute to the inconsistency, and hence reduce the correlation coefficient of the relationship between hardness and yield

strength. Hardness measurement variations similarly contribute to reductions in the correlation with ultimate tensile strength. Section 3.1 shows errors which may influence hardness where the precautions taken to minimize these errors include controlling the sample surface roughness and minimizing vibrations. Despite the accuracy of the measuring process, deviations from average hardness measurements can occur due to variations in microstructure across the sample surface.

6.1.2 Prediction of YS (8% Engineering Strain) from Hardness

Direct correlations between YS and hardness contain a significant amount of scatter, as shown in Figure 6.1 and Figure 6.2. An improvement upon the correlation is expected when stress is measured for pre-defined strains because Rometsch and Schaffer [47] obtained a good correlation between YS and hardness when they compared stress at an engineering strain of 8% to Vickers hardness. They selected values of stress at 8% strain because this strain level was associated with Vickers hardness testing for a variety of strain hardening alloys [82, 83]. Given that strain associated with a Vickers indentation is about 8% for a variety of strain hardening alloys [47, 82] and that the tensile stress at a strain of 8% correlates well with the Vickers hardness [83], it is likely that the hardness may correlate well with the stress at a certain large strain.

Figure 6.5 and Figure 6.6 show a plot of stress at a true strain of 15.43% (engineering strain of 8%) versus Vickers hardness for Hydro and RTA materials. The R^2 value, and therefore the correlation between stress and Vickers hardness, shows negligible correlation improvement on comparison of Figure 6.1 with Figure 6.5 for Hydro. The correlation is significantly worse for the RTA material as shown in Figure 6.6 as compared with Figure 6.2.

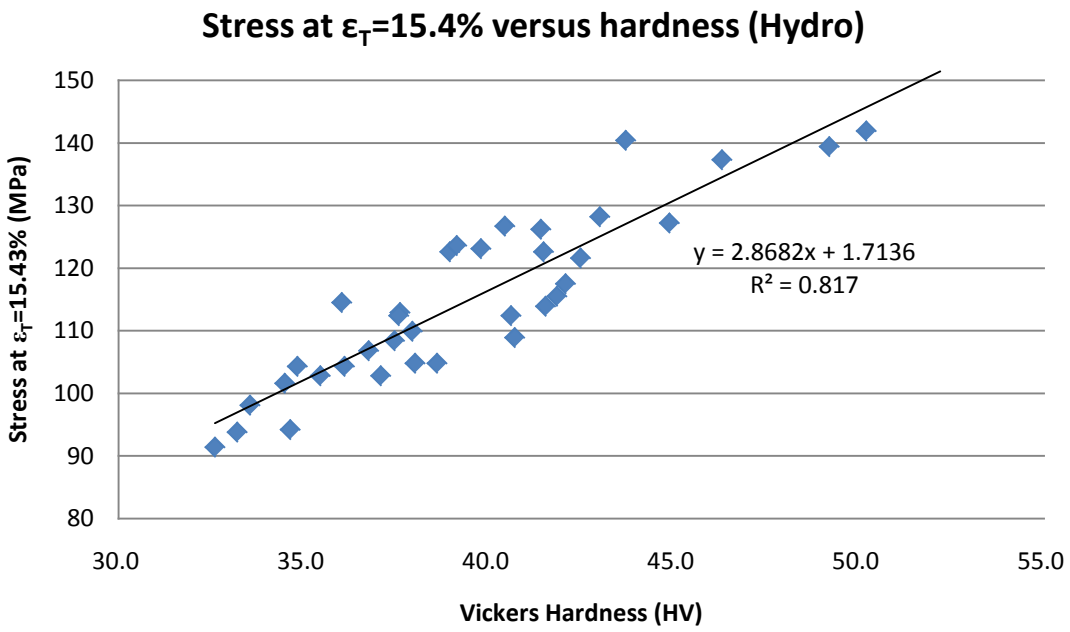

Figure 6.5: Stress at a true strain of 15.43% (engineering strain of 8%) versus Vickers Hardness (Hydro)

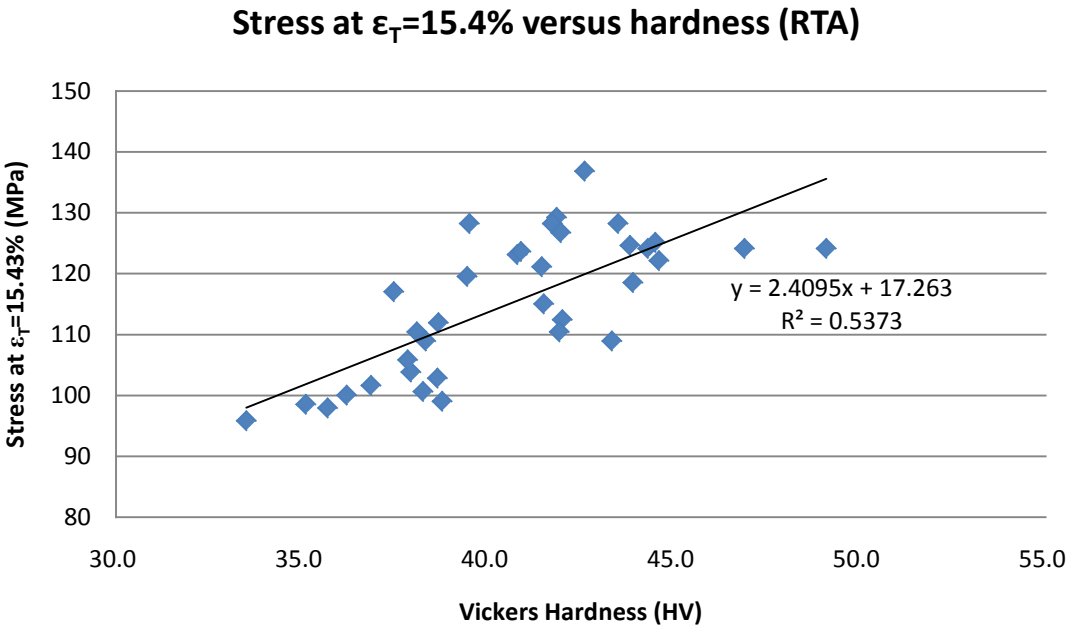

Figure 6.6: Stress at a true strain of 15.43% (engineering strain of 8%) versus Vickers Hardness (RTA)

6.1.3 Integration of Hardness and Tensile Tests

A hardness indentation is schematically shown in Figure **6.7** which can be analyzed by referring to the stress – strain curve shown in Figure **6.8**. The points U, C, A, E in

Figure **6**.**7**, start from the tip to the edge of the indentation, and indicate different locations which experience different deformation changes during hardness testing. Each point has an associated stress value as indicated in Figure **6**.**8**.

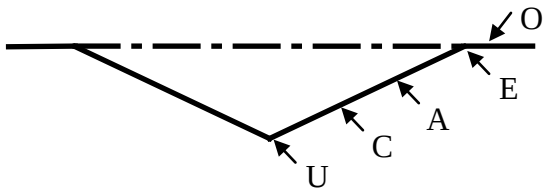

Figure 6.7: Schematic drawing of hardness indentation indicating

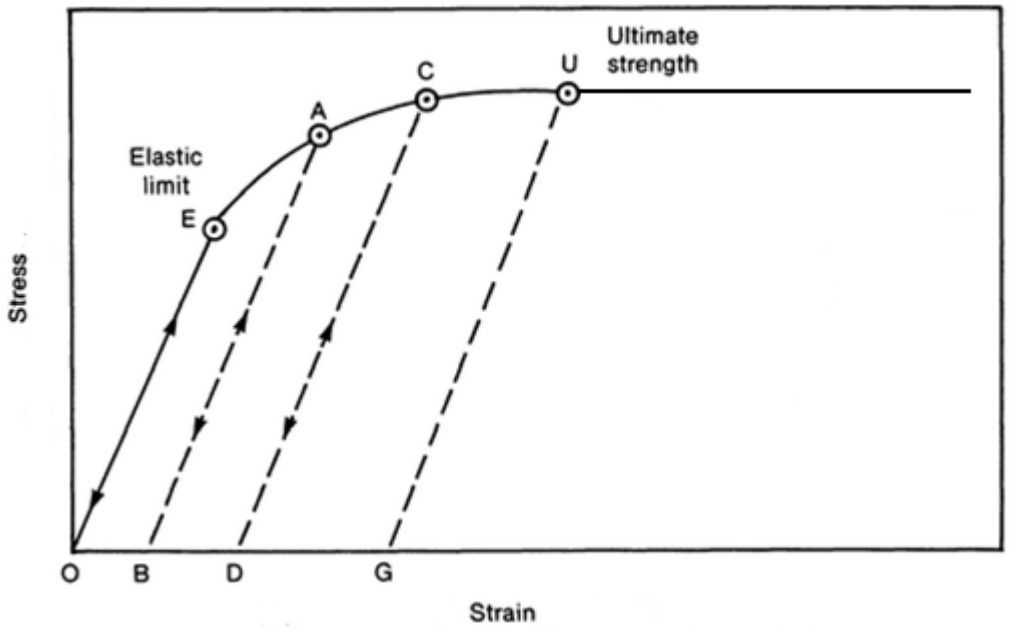

Figure 6.8: Hardness indentation correlates to a typical stress – strain curve

Maximum deformation is expected at point U where the stress magnitude is at least the value of UTS due to the observed plastic deformation. It may be larger due to an increase in particle density caused by severe and non-uniform plastic deformation in the vicinity of the indentation site (Figure **3**.**2**).

Point E is the point where the stress applied during hardness testing becomes sufficient to cause permanent deformation. The position of point E depends on the composition of the material and its historical heat treatment.

Points A and C are located on the edge of the indentation and should have a stress magnitude between YS and UTS. Therefore, the combination of the hardness indentation is a value which is higher than at point E and lower than at point U.

Considering the tensile results of 405°C @ 85mins and 480°C @ 85mins for Hydro material, the strain at UTS is 0.38 s^{-1} and 0.30 s^{-1} respectively. Figure **6.9** shows a schematic drawing of stress – strain curves for two test materials. The stresses at 8% of engineering strain are indicated on two curves (X: 480°C, Y: 405°C). Point X shows a dramatic increment from YS as compared to point Y. This is due to a larger strain hardening effect for a 480°C sample during deformation due to work hardening from dissolution of precipitates (Section 6.1.1). The results show that stress at an engineering strain of 8% does not correlate with the Vickers hardness for every test sample. However, there may be an alternative engineering strain that will provide stress values that correlate better with Vickers hardness.

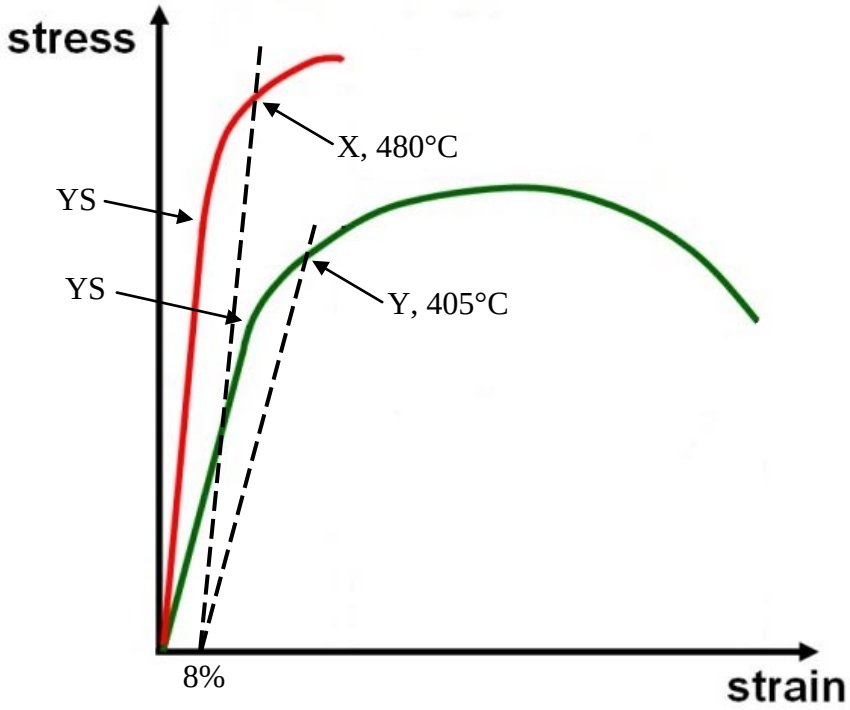

Figure 6.9: Stress – strain curves for different materials

6.2 Analysis of Material State using Room Temperature Tests

Billet material hardness and strength are dependent on its chemical composition and heat treatment history. The Al-Mg-Si alloy phase diagram (Figure 2.2) provides a picture of the dependence of phase on temperature and chemical composition, where excess magnesium or excess silicon change the phase diagram [19] (Figure 2.3). Therefore, the phase diagram varies between material suppliers as its form is dependent on the chemical composition of the original material. However, this variation may be

attributed to a composition of Mg_2Si that is different to the supplier's nominal composition.

The percentage of Mg_2Si in the supplied billet is calculated to be 0.56 % Mg_2Si (Section 4.1) and therefore, using Figure 2.2, the solvus and solidus temperatures are 400°C and 620°C respectively. Figure 6.10 shows a suggested eutectic phase diagram for AA6060 alloy. However, the material used for our experiments possess excess silicon, which will reduce the solvus temperature [84].

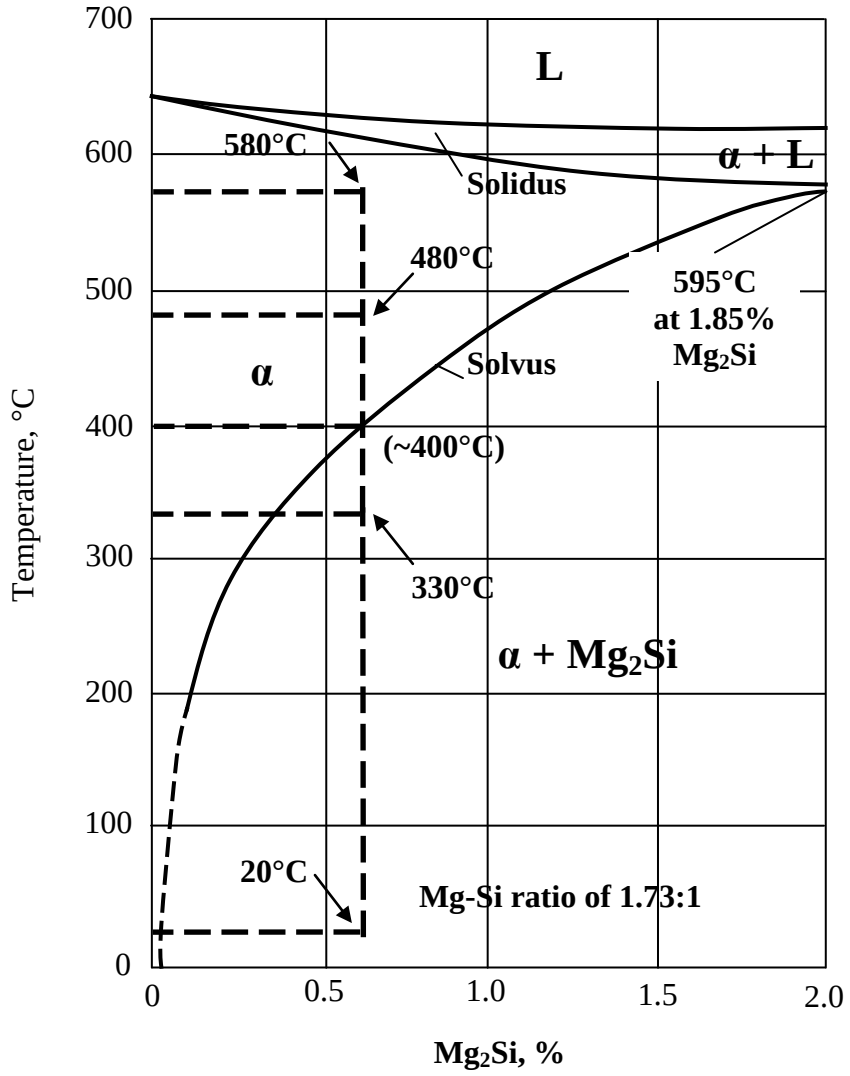

Figure 6.10: Phase diagram for Al-Mg-Si alloy indicating important transition zones [redrawn from Rashid's diagram [16]]

Figure **6.10** can be improved to better match the billet material by determining the solvus temperature for each billet material. The minimum (330°C) and maximum (480°C) testing temperatures are respectively shown to be above (within the 'α + Mg_2Si' region) and below (within the 'α' region) the solvus line. Therefore, using information

about the hardening behaviour, the solvus line on Figure **6.10** can be used a reference to determine the solvus temperature for the Hydro and RTA billet material.

At temperatures above the solvus line, and for sufficient heating periods, magnesium silicide dissolves completely into the matrix. If the temperature is maintained at a single temperature within α region (above the solvus line), the grain structure will attain grain stability and precipitation hardening due to Mg_2Si precipitates will approach zero. The time required for the complete dissolution of Mg_2Si precipitates reduces as the temperature increases. Therefore, measurement of the temperature at which Mg_2Si precipitate strengthening is zero, will allow the acquisition of the solvus temperature for the billet material.

The influence of temperature and heating duration on material phase (and therefore yield strength) is discussed in the following section.

6.2.1 Effect of Heating Temperature on Total Yield Strength

The strengthening mechanisms of work hardening, solid solution strengthening, and precipitation hardening each contribute to the total yield strength of AA6060 alloys. Rometsch has analyzed the yield strength assuming independent contributions of solid solution hardening, precipitation hardening, and intrinsic strength [47]. Figure **6.11** shows total yield strength data at the longest heating time (85 mins). Additionally, it presents typical curves for each hardening mechanism, assuming independent yield strength contributions for each hardening mechanism. Yield strength stabilizes as duration increases (as seen in Figure **5.7** and Figure **5.8**), therefore total yield strength at 85 minutes is used for the analysis as there is less opportunity for outlier measurements.

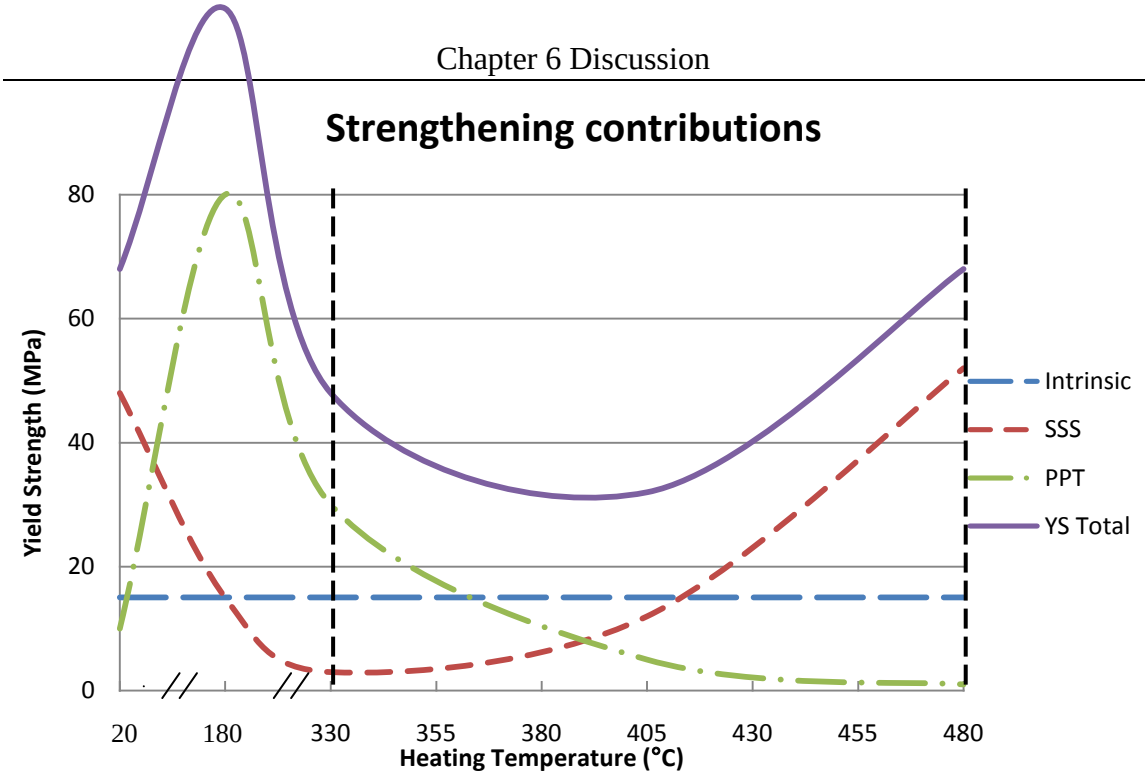

Figure 6.11: Representation of strengthening contributions to total yield strength

A dominating large increase in strength is observed at 180°C (Figure **6.11**) due to a high density of fine and needle-shaped β'' particles uniformly dispersed in the matrix [22]. The peak tensile properties for the aged AA6060 can be up to 215 MPa for yield strength and 240 MPa for ultimate tensile strength [85-87]. Since these precipitates are thermodynamically unstable, the smallest ones will start to dissolve as the heating temperature increases, while the larger ones will continue to grow. At the same time, coarse rod-shaped β' precipitates may form in the temperature range between 250 and 480°C [85].

The contributions to yield strength due to temperature and time for temperatures between 330°C and 480°C are analyzed using Eq. 2.4 which was presented in page 28. The analysis assumes independent contributions of solid solution hardening, precipitation hardening, and intrinsic strength. The remaining discussion will investigate the various hardening contributions at room temperature, the minimum and maximum test temperatures, and minimum yield strength value (405°C). It will then attempt to improve the phase diagram (Figure 6.10) to a better representation of the 6060 Aluminium provided to Fletcher Aluminium.

6.2.2 As-receive at Room Temperature

The homogenized air-cooled billet is cooled for a significant duration as indicated in Figure 2.13 and at below the solvus line indicated in Figure **6.10**. As compared to heat treated samples, the YS of the as-received samples are higher due to the solutionized Mg and Si during the homogenization process and the presence of a small volume fraction of fine second phase (Mg_2Si) particles formed by the forced air cooling process after homogenization.

Substituting values of yield strength at room temperature into Eq. 2.4, the material state of the as-received material can be analyzed.

$$\sigma_{YS} = \sigma_{sss} + \sigma_{ppt} + \sigma_{intrinsic} \quad (2.4)$$

$$\sigma_{YS} = 66\ MPa, \sigma_{intrinsic} = 15\ MPa \quad (6.5)$$

$$\sigma_{sss} + \sigma_{ppt} = 51\ MPa \quad (6.6)$$

The relatively high yield strength is provided by the combination of both solution and precipitation strengthening. The air cooled billet material retains the majority of the magnesium and silicon in the matrix which contributes to solution strengthening. Additionally, during cooling from 405°C, precipitates growing in the homogenized matrix contribute to precipitation strengthening. The two strengthening effects are noticeable but accurate values for σ_{sss} and σ_{ppt} require the precipitate volume fraction and particle size which may be obtained using a TEM [47].

The cooling rate of the air cooled billet is relatively small which theoretically will result in a low quantity of Mg_2Si precipitate growth in the matrix. Additionally, the large amount of dissolved Mg and Si particles has a greater solution strengthening effect on yield strength. Therefore σ_{sss} will be much larger than σ_{ppt} for as received billet material.

$$\sigma_{sss,asrecieved} \gg \sigma_{ppt,asreceived} \quad (6.7)$$

6.2.3 Minimum Yield Strength (405°C)

The yield strength of test material reaches a minimum value of 30MPa when it is heat treated at 405°C. The overall yield strength and intrinsic yield strength are substituted into Eq. 2.4 (page 85).

$$\sigma_{YS} = \sigma_{sss} + \sigma_{ppt} + \sigma_{intrinsic} \quad (2.4)$$

$$\sigma_{YS} = 30\ MPa,\ \sigma_{intrinsic} = 15\ MPa \quad (6.8)$$

$$\sigma_{sss} + \sigma_{ppt} = 15\ MPa \quad (6.9)$$

Consequently, the yield strength improvement provided by the combination of solid solution strengthening and precipitation hardening is 15 MPa. Therefore, at 405°C, there is a low contribution of σ_{sss} and σ_{ppt} to total yield strength. The low degree of solid solution hardening is attributed to none or part dissolution of precipitates. The low degree of precipitation hardening is attributed to coarsening of precipitates. The presence of coarse precipitates would reduce the mechanical properties of the materials due to the reduction of inter-particle spacing and increase of precipitate size due to the presence of coarse precipitate in the heat treated samples. This results in a reduction of yield strength as compared to states at other temperatures.

The minimum yield strength obtained at 405°C, is similar to the results of Langkruis et al. whom observed a minimum at 400°C [28]. The minimization of strengthening effects is provided by a range of solution and precipitation hardening factors. At 405°C, there is no β'' precipitation strengthening as all β'' precipitates are fully dissolved. Approximately 40 – 50% of the initial volume fraction of β' is left after heating to 405°C, where β' is a large contributor to precipitation strengthening of the material [28]. It results in a reduction of precipitation strengthening and an increase in solution strengthening by the dissolution of β'.

6.2.4 Yield Strength at the Lowest Heating Temperature (330°C)

Yield strength for the test sample produced at 330°C (~ 48 MPa) is lower than the yield strength of the as-received sample and higher than the lowest yield strength at 405°C. The strengthening contributions of the precipitates and dissolved solution are analysed at 300°C by substitution of yield strength values into Eq. 2.4.

$$\sigma_{YS} = \sigma_{sss} + \sigma_{ppt} + \sigma_{intrinsic} \quad (2.4)$$

$$\sigma_{YS} = 48\ MPa,\ \sigma_{intrinsic} = 15\ MPa \quad (6.10)$$

$$\sigma_{sss} + \sigma_{ppt} = 33MPa \quad (6.11)$$

Two important factors are the amount of Mg and Si in solid solution and the amount of coarse β and β' phase precipitates in the structure. At temperatures higher than 300°C, there is a small volume fraction of the β'' precipitate present in the samples, and its hardening effect on the flow stress is negligible [28]. The non-dissolved β and β' phase precipitates become more coarse at this temperature because at temperatures above 250°C, more β' phase precipitates grow in the matrix [28]. The transformations at this temperature reduce σ_{sss} and increase σ_{ppt} by the formation of the new β' phase. However, β' phase has a reduced hardening effect relative to β'' phase. Overall, σ_{sss} and σ_{ppt} at 330°C are all reduced as compared to the material state of as-received alloys; but are still larger than σ_{sss} and σ_{ppt} at 405°C.

6.2.5 Yield Strength at the Highest Heating Temperature (480°C)

The yield strength of test Aluminium reaches a value of 68 MPa when it is heat treated at 480°C. At temperatures above 465°C, the effect of precipitation strengthening is negligible as the majority of alloying constituents are dissolved in the material matrix; therefore it is assumed that $\sigma_{ppt} \approx 0$ MPa. Using Eq. 2.4 and substituting experimental tensile values for $\sigma_{YS} = 68$ MPa, we obtain the following expression for σ_{sss}.

$$\sigma_{YS} = \sigma_{sss} + \sigma_{ppt} + \sigma_{intrinsic} \qquad (2.4)$$

$$\sigma_{YS} = 68MPa, \sigma_{ppt} = 0\ MPa,\ \sigma_{intrinsic} = 15\ MPa \qquad (6.12)$$

$$\sigma_{sss} = 53\ MPa \qquad (6.13)$$

The primary cause of the increase in hardness is the heating temperature exceeding the solvus temperature; this causes the precipitates to re-dissolve and results in solute solution hardening as presented in Figure **6.11**. At 480°C, β'' and β' should be fully dissolved. There is a large amount of Mg and Si dissolved into the matrix which increases the σ_{sss} significantly and reduces σ_{ppt}.

During solutionizing, these solute atoms were dissolved in the Al matrix and retained in meta-stable state. These materials were cooled to room temperature, which causes the clustering of meta-stable solutes within the vacancies. These fine clusters (precipitates) act as a barrier for dislocation movement, causing an enhancement of initial strength.

The value of σ_{ppt} at 480°C is expected to be much less than σ_{ppt} at 330°C. At high temperatures, solid solution strengthening is expected to have a major effect. At 330°C,

a greater contribution is provided by precipitation hardening. An interaction between solution strengthening and precipitation hardening means that the extrudability of the material is optimised at 405°C. Although, the temperature must not exceed 405°C as the occurrence of surface defects increases. This is close to the current extrusion parameters used at Fletcher Aluminium.

6.2.6 Effect of Heating Parameters on Strain Hardening Exponent and Ultimate Tensile Strength

A range of strengthening effects were discussed in Section 2.3 including solid solution strengthening, dislocation strengthening (strain hardening), precipitation hardening and grain boundary strengthening. The tensile tests confirmed the occurrence of significant hardening, caused by severe plastic strain induced in the samples, in all the deformed states [88, 89].

Variations of yield strength and ultimate tensile strength from flow stress are caused by strengthening in the structure of the Aluminium alloy through strain hardening. The trend in work hardening rates of test alloys, subjected to different processing states and a large strain, is determined from the results and shown below:

$$n_{330°C} < n_{355°C} < n_{380°C} < n_{405°C \sim 480°C} \qquad (6.14)$$

The solid solution treated samples at high temperature (405 – 480°C) are observed to work harden better than lower temperature (330 – 405°C) treated samples. The improved work hardening behaviour is provided by a high content of solute (Mg and Si) which increases the strength by partially pinning dislocations and impeding dislocation motion which results in enhanced dislocation density and dislocation-dislocation interactions [90]. Results of n value for both materials are the evidence as presented in Section 5.2.3.

Figure **6.12** shows the stress versus strain curves of 330°C and 455°C heat treated samples. Both samples have similar values of yield strength (48 MPa for 330°C and 51 MPa for 455°C), however the difference of two ultimate tensile strength values are up to 31 MPa. An increase in resistance to dislocation motion caused by an expected improvement in the quantity of dissolved solution shows that the hardening rates of solid solution treated aluminium alloys are higher than those of precipitation alloys.

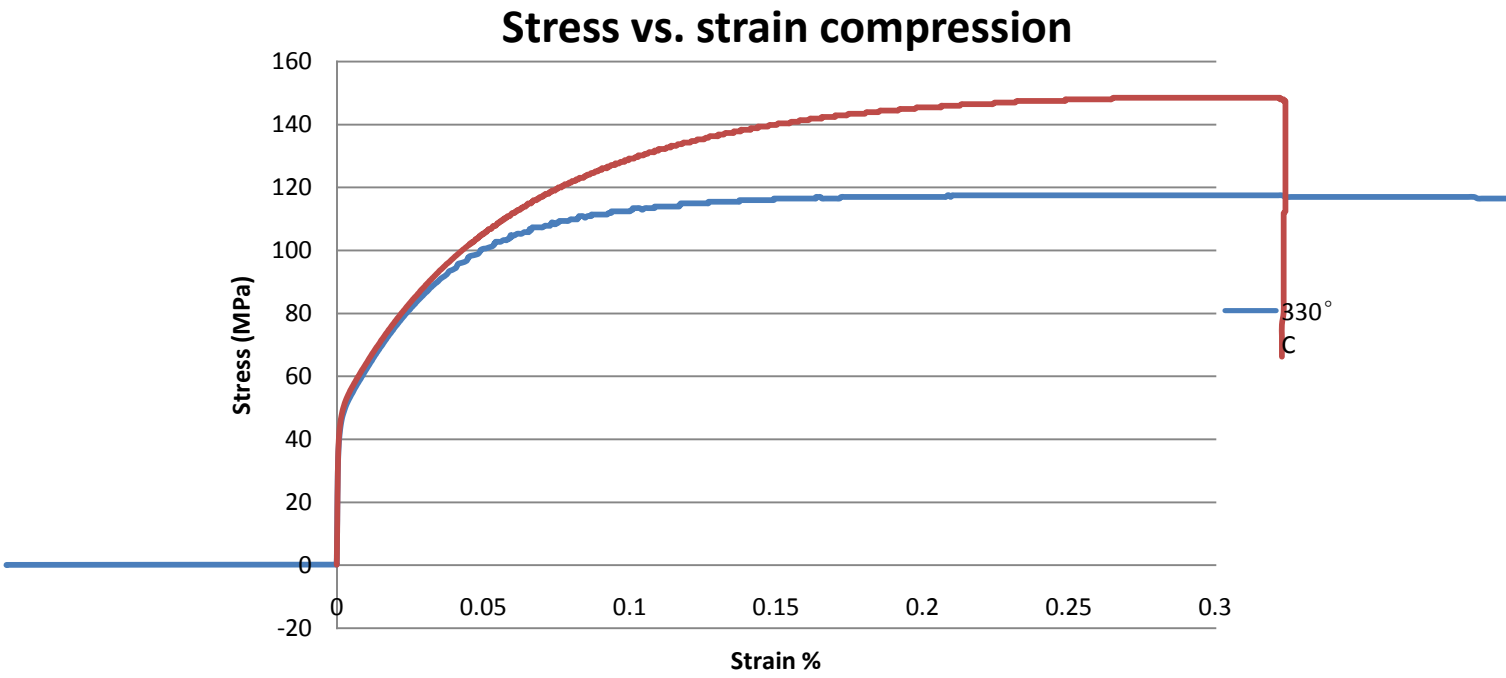

Figure 6.12: Stress vs. strain curves (Hydro 330°C and 455°C)

6.3 Analysis of Material State using Elevated Temperature Tests

The following section will discuss peak flow stress. It will discuss the constants obtained, from the peak flow stress values, and for and from the Zener Holloman equation. The various constants obtained from and for the Zener Holloman equation will then be used to establish a relationship between the temperature and the extrusion velocity.

6.3.1 Deformation at Elevated Temperature

The peak flow stress is analogous to ultimate tensile strength for elevated temperatures. Similarities in the stress values are shown by the comparison of Figure **4.20**, which shows a typical tensile test curve for AA6xxx, and Figure **6.14**, which shows the Gleeble test results.

The peak flow stress was found by calculating the maximum stress for each Gleeble test. An inverse linear relationship was obtained between peak flow stress and temperature as shown in Figure **5.17** and Figure **5.19**.

Previous analysis at room temperature assumed that the total yield strength could be determined from independent contributions of solid solution strengthening, precipitation strengthening and intrinsic strength. The inverse linear relationships of Figure **5.17** and Figure **5.19** mean that the contributions of each hardening mechanism must total to a linear relationship with temperature. Alternatively, there is no hardening effect due to precipitation or solid solution. It is shown in Section 2.3 that solid solution strengthening and precipitation hardening must exist due to the effect of changes in impurities.

A representation of the hardening contributions of solid solution hardening and precipitation hardening; and the resultant linear sum, is shown in Figure 6.13. The flow stress of the material is observed to reduce at elevated temperatures. The lower peak flow stresses is observed at higher temperatures in Figure 6.13 which is due to further dynamic recovery and local dynamic recrystallization than that at lower temperatures [66, 71, 72]. It also can be explained by the Eq. 2.4. The intrinsic strength is constant at the elevated temperature. The strengthening of precipitation strengthening reduces due to the dissolution of precipitates into the matrix. Microstructurally, higher temperatures facilitate recrystallization which results in the decrease of dislocation density and increases in subgrain size. Therefore, higher temperature reduces the effect of solution strengthening effect during hot deformation.

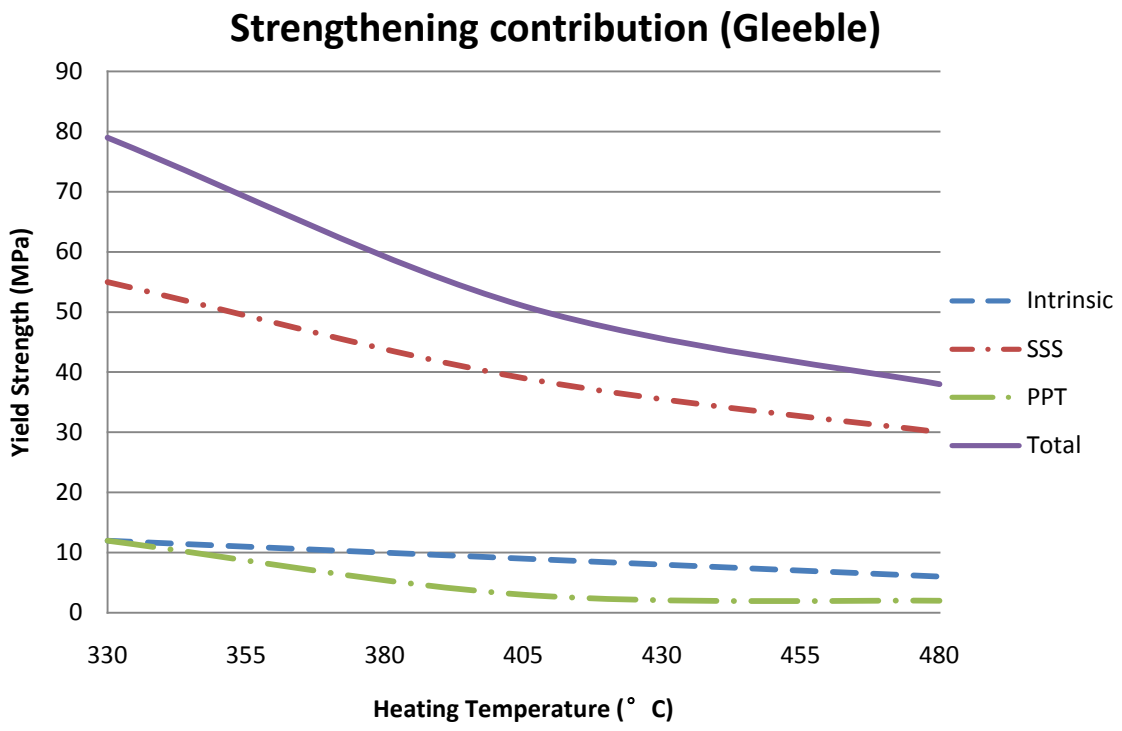

Figure 6.13: Representation of strengthening contributions to peak flow stress

The relationship between peak flow stress and heating time was presented in Figure **5.18** and Figure **5.20**. In majority, there is observed to be no variation in flow stress with heating time.

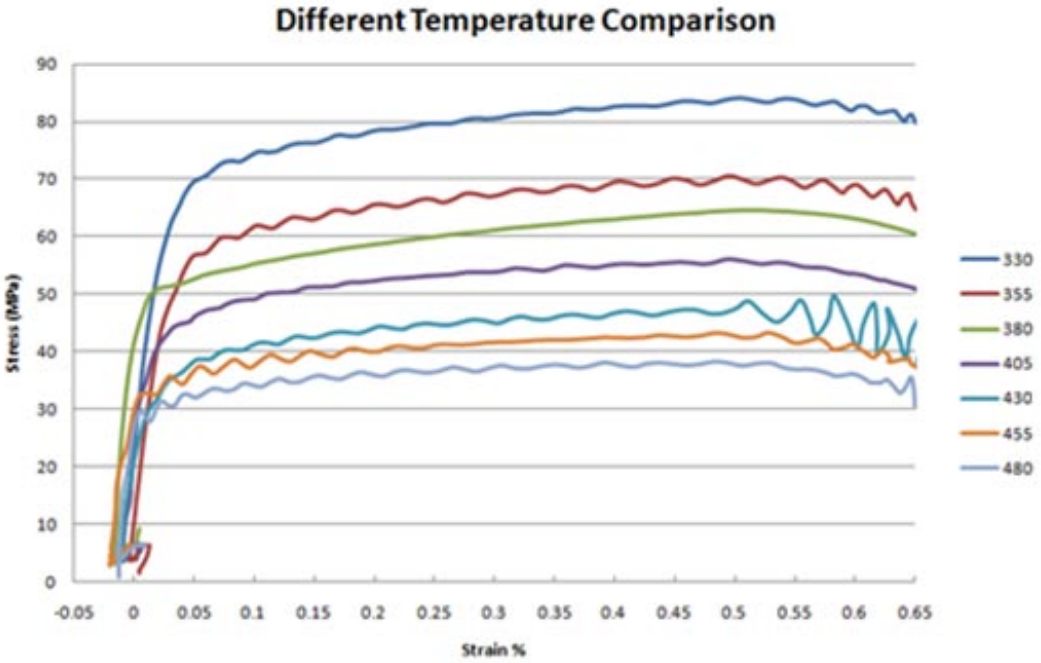

Figure 6.14: Representative compression stress-strain curves at 330 – 480°C for RTA (strain rate 2 s^{-1})

The tensile test stress-strain curves show very high hardening behaviour at room temperature. A reduction in hardening behaviour for an increase in heating temperature is observed during Gleeble testing as seen by the difference between yield and ultimate flow stress in Figure **6.14**. Additionally, the strain corresponding to the peak flow stress (PFS) decreases with deformation temperature increases, and is caused by high hardening rates at initial deformation stages. The flow softening experienced with temperature increments is associated with dynamic recovery and recrystallization, as well as dynamic coarsening of precipitates, during hot deformation of aluminium alloy [66, 72, 91].

The work hardening characteristics of aluminium alloys at elevated temperature vary both with temperature and with strain rate. Strain hardening decreases progressively as testing temperature increases and no efficient strain hardening occurs.

6.3.2 Constants for Zener Hollomon Equation

The peak flow stress was used to determine several constants within the Zener-Hollomon equation including A, n and Q. The values obtained compare well with current literature for AA6xxx materials as shown in Table **5.2**. These constants are useful for describing material transformation at elevated temperatures. The following discussion will focus on the significance of the values obtained for activation energy (Q) and the Zener Hollomon parameter (Z).

The Zener-Hollomon parameter will then be shown to be constant to provide a foundation for Section 6.3.3.

Activation Energy, Q

Activation energy is a parameter within the Zener Holloman equation which is used to define the energy required for material deformation. A review of activation energy is provided in Section 3.4, which provides that the Q value for AA6060 alloys is primarily dependent on the quantity of Mg and Si solutes in the matrix.

A range of expected activation energy values for AA6xxx series alloys, including AA6060, was presented in Table **3.3**. These values correspond well with activation energy calculated from the results where the activation energy for RTA aluminium alloy is 132.6 kJ/mol.

The activation energy of pure aluminium (143~158 kJ/mol) [5, 92], is higher than the activation energy for RTA aluminium alloy where pure aluminium is known to be more extrudable that most Aluminium alloys. Figure **3.10** shows the flow stress for a range of AA6xxx series alloys, where it is shown that AA6060 has a lower activation energy than pure aluminium (15 MPa).

Observation of Figure **3.10** shows that variances in chemical composition have an effect on flow stress, and therefore have an effect on the activation energy (Table **3.3**). An example was presented by Zhang et. al. and He et. al. whom observed higher deformation activation energy for increments in impurities during hot deformation of solution treated aluminium alloys [66, 73]. Nengping et. al. also found that the apparent activation energy reduces when the solute content of the alloy increases as a function of temperature [72]. Solid solution strengthening and precipitation hardening therefore must exist due to the dependence of flow stress on material composition.

Zener Hollomon Parameter

The empirical Zener Hollomon equation has been tested by several researchers [5, 65, 66]. Therefore the Z-values obtained in Table **5.3** compare well with literature providing Gleeble testing results and Z values as shown in Table **3.2**.

$$Z = \dot{\varepsilon}\, exp\left(\frac{Q}{R\,T}\right) = A\big(sinh(\alpha\,\sigma)\big)^{n} \qquad (3.6)$$

The situation encountered for the Gleeble test is a special case where the Z value is observed to remain relatively constant. It remains relatively constant because the strain rate is maintained at a constant value, and the temperature is does not change significantly during tests.

The Zener Hollomon equation can be related to the extrusion process, where the extrusion pressure is related to the flow stress, strain rate is related to the extrusion velocity, and the Zener temperature is the temperature during extrusion.

The following section discusses the low speed period of the Fletcher Aluminium AA6060 extrusion process indicated in Figure **1.12**. The flow stress is assumed to be constant because the machine has reached its maximum power capacity, and the extrusion pressure is constant. It can therefore be assumed that the flow stress is also constant. Observation of Eq. 3.6 shows that right hand side of the equation also becomes a constant value when the flow stress is maintained at a constant value (dependent on A, α, and n). Therefore, the Z value is also assumed to be constant.

$$constant = \dot{\varepsilon}\, exp\left(\frac{Q}{R\,T}\right) \qquad (6.15)$$

A new expression can be generated which relates strain rate to temperature as shown in Eq. 6.16 below;

$$\dot{\varepsilon} = constant \times e^{\left(-\frac{Q}{R\,T}\right)} \qquad (6.16)$$

6.3.3 Relationship Between Temperature and Extrusion Velocity

Felthams equation (Eq. 4.2) is used in combination with the modified Zener-Hollomon equation (Eq. 3.6) to present the relationship between extrusion temperature and velocity.

$$\frac{6*V_R*D_B^2*(0.171+1.86\,lnR)*tan\,(38.7+6.9\,lnR)}{D_B^3-D_E^3} = constant \times e^{\left(-\frac{Q}{R\,T}\right)} \qquad (6.17)$$

$$V_R = constant \times e^{\left(-\frac{Q}{RT}\right)} \times \frac{(D_B^3 - D_E^3)}{6 \times D_B^2 \times (0.171 + 1.86\ lnR) \times tan\ (38.7 + 6.9\ lnR)} \quad (6.18)$$

Where the constants V_R, R, D_E D_B are described in Section 4.5.1.

Figure 6.15 uses typical Fletcher Aluminium extrusion parameters as presented in Table 1.2 and a constant Ln Z value of 24.2 (405°C) to plot temperature against expected extrusion speed. Observation of the ideal relationship shows a significant increment in extrusion speed as the extrusion temperature increases. For instance, increasing the production preheating temperature from ~405°C to 480°C will provide an extrusion speed that is more than 10 times faster than the speed at 405°C. However, reduction of the product quality at higher extrusion temperatures must be considered in conjunction with speed improvements.

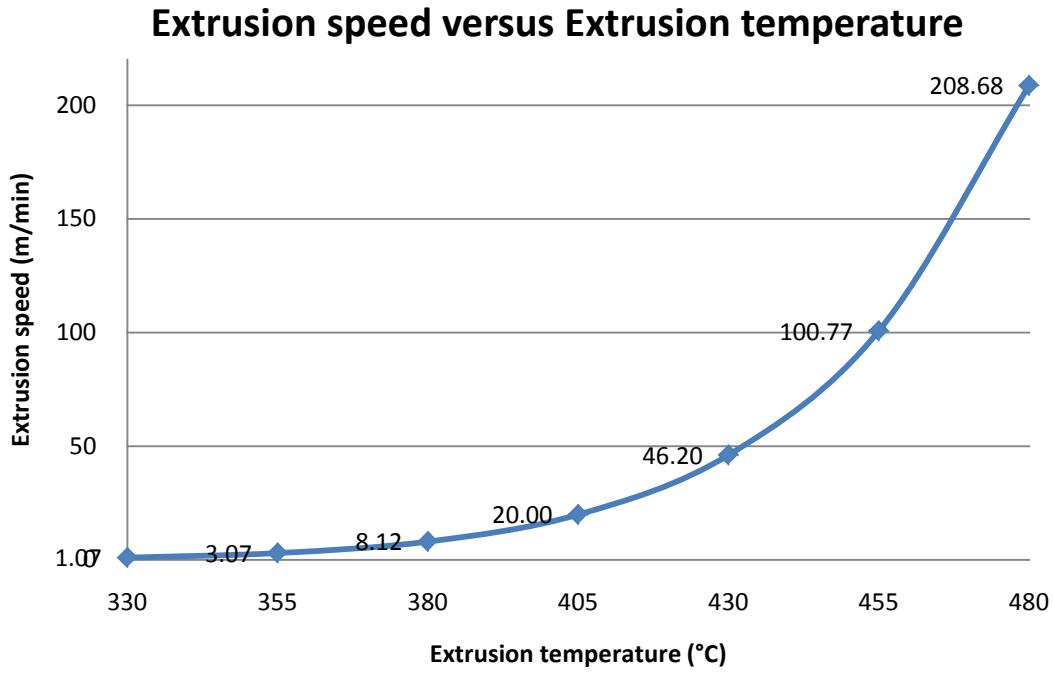

Figure 6.15: Simulation of changing extrusion temperature

Chapter 7 Conclusion and Recommendations

Based on the results discussed in the precious chapter the following conclusions and recommendations have been drawn.

- For the room temperature tests, the strength of the material is dependent on the combination of solution, precipitation and intrinsic strengthening effects. Solid solution strengthening is dominant at high temperatures (405 – 480°C), and precipitation strengthening is dominant at low temperatures (330 – 405°C). The hardness and tensile test results indicate the lowest hardness and YS at approximately 405°C.

- Precipitation strengthening is reduced significantly by increasing the heating temperature for temperatures between 330 and 405°C. Above 405°C, reduction of precipitation strengthening can be ignored.

- Strengthening due to dissolution of Mg_2Si precipitates is significant at temperatures above approximately 405°C. The amount of solution strengthening above 405°C increases as temperature increases. The amount of Mg_2Si dissolution therefore increases as temperature increases.

- According to the phase analysis with hardness and tensile results, the solvus temperature of Hydro and RTA material is approximately 405°C. The best preheating temperature for extrusion is probably a temperature just below 405°C.

- The tensile test results indicate the lowest UTS at approximately 380°C. As the preheating temperature exceeds the T_{solvus} (~405°C), higher UTS values are obtained due to strain hardening effects from solutionized Mg and Si during the deformation test. Resultantly, solutionized test samples have a larger n value than precipitation strengthened samples which means strain hardening is more significant for solutionized samples than precipitation strengthened samples.

- Correlations between hardness and YS/UTS were identified to be that hardness versus YS ($R^2 \approx 0.82$/ 0.81 Hydro and RTA respectively) has a stronger correlation

than hardness versus UTS ($R^2 \approx 0.75$ / 0.67 Hydro and RTA respectively). Hardness cannot simply translate to tensile test values (YS and UTS) due to the complexity of the deformation process during hardness testing. Correlations between hardness and tensile stress at engineering strain of 8% were identified to have negligible correlation improvement on comparison with hardness and YS Hydro.

- Flow stress is inversely proportional to temperature for RTA materials and temperatures between 330°C and 480°C.

- Zener-Hollomon equation and Felthams equation were used to determine the relationship between the extrusion temperature and extrusion speed by varying the extrusion flow stress. The following relationship was obtained for Fletchers process;

$$V_R = constant \times e^{\left(-\frac{Q}{RT}\right)} \times \frac{(D_B^3 - D_E^3)}{6 \times D_B^2 \times (0.171 + 1.86\ lnR) \times tan\ (38.7 + 6.9\ lnR)}$$

- Increasing the production preheating temperature from ~405°C to 480°C will improve the extrusion speed 10 times. However, reduction of the product quality at higher extrusion temperatures must be considered in conjunction with speed improvements.

Recommendations

- Industrial trial tests are recommended at 330°C, 405°C and 480°C in order to test the Gleeble test results. This is required because ideal testing conditions are used during the Gleeble test.

- Trials are also required to test the accuracy of the Gleeble – Holomon – Felthams equation, a corrected version of this equation will allow estimation of extrusion speed based on extrusion temperature.

- Increase operating temperature and measure the amount of power required to maintain the increased operating temperature. Use this to determine the payback period for a new compressor.

APPENDICES

Appendix A: Billet Sample

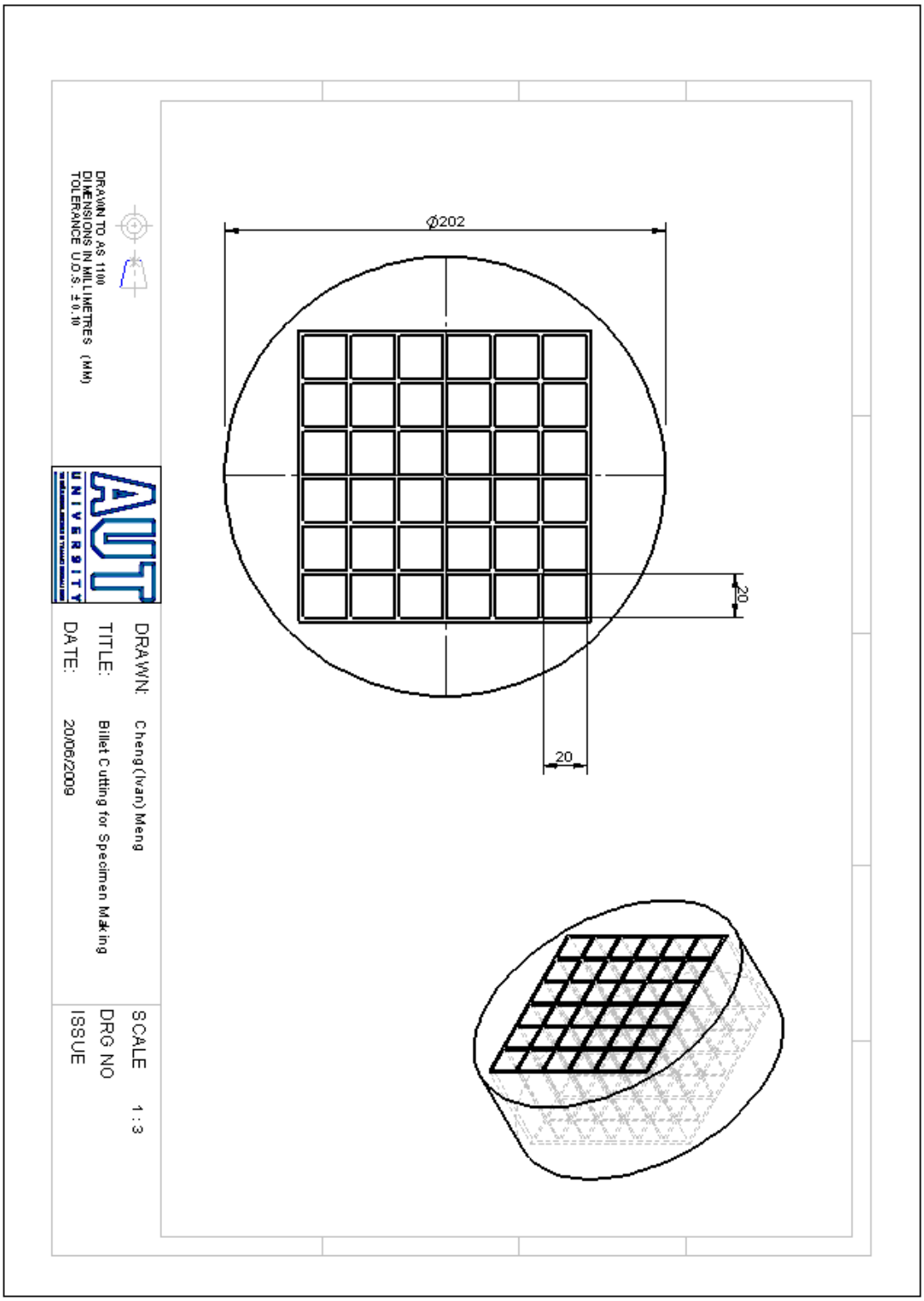

Appendix B: Test Sample Details

Table 7.1: Overall dimensions and quantities of test samples

Test method	Supplier	Dimension* (mm)	Quantity
Hardness	RTA	10x10x10	35
	Hydro	10x10x10	35
Tensile	RTA	Ø11x48.4	35
	Hydro	Ø11x48.4	35
Gleeble	RTA	Ø10x15	35
	Hydro	-	0

*Dimensions for tensile samples denote overall dimensions

Table 7.2: Hydro identification codes for combinations of temperature and time used for sample heat treatment

Temperature ºC	Time (minutes)				
	15	25	40	60	85
330	H 330 15	H 330 25	H 330 40	H 330 60	H 330 85
355	H 355 15	H 355 25	H 355 40	H 355 60	H 355 85
380	H 380 15	H 380 25	H 380 40	H 380 60	H 380 85
405	H 405 15	H 405 25	H 405 40	H 405 60	H 405 85
430	H 430 15	H 430 25	H 430 40	H 430 60	H 430 85
455	H 455 15	H 455 25	H 455 40	H 455 60	H 455 85
480	H 480 15	H 480 25	H 480 40	H 480 60	H 480 85

Table 7.3: RTA identification codes for combinations of temperature and time used for sample heat treatment

Temperature ºC	Time (minutes)				
	15	25	40	60	85
330	R 330 15	R 330 25	R 330 40	R 330 60	R 330 85
355	R 355 15	R 355 25	R 355 40	R 355 60	R 355 85
380	R 380 15	R 380 25	R 380 40	R 380 60	R 380 85
405	R 405 15	R 405 25	R 405 40	R 405 60	R 405 85
430	R 430 15	R 430 25	R 430 40	R 430 60	R 430 85
455	R 455 15	R 455 25	R 455 40	R 455 60	R 455 85
480	R 480 15	R 480 25	R 480 40	R 480 60	R 480 85

Appendix C: Drawing of Sample Container

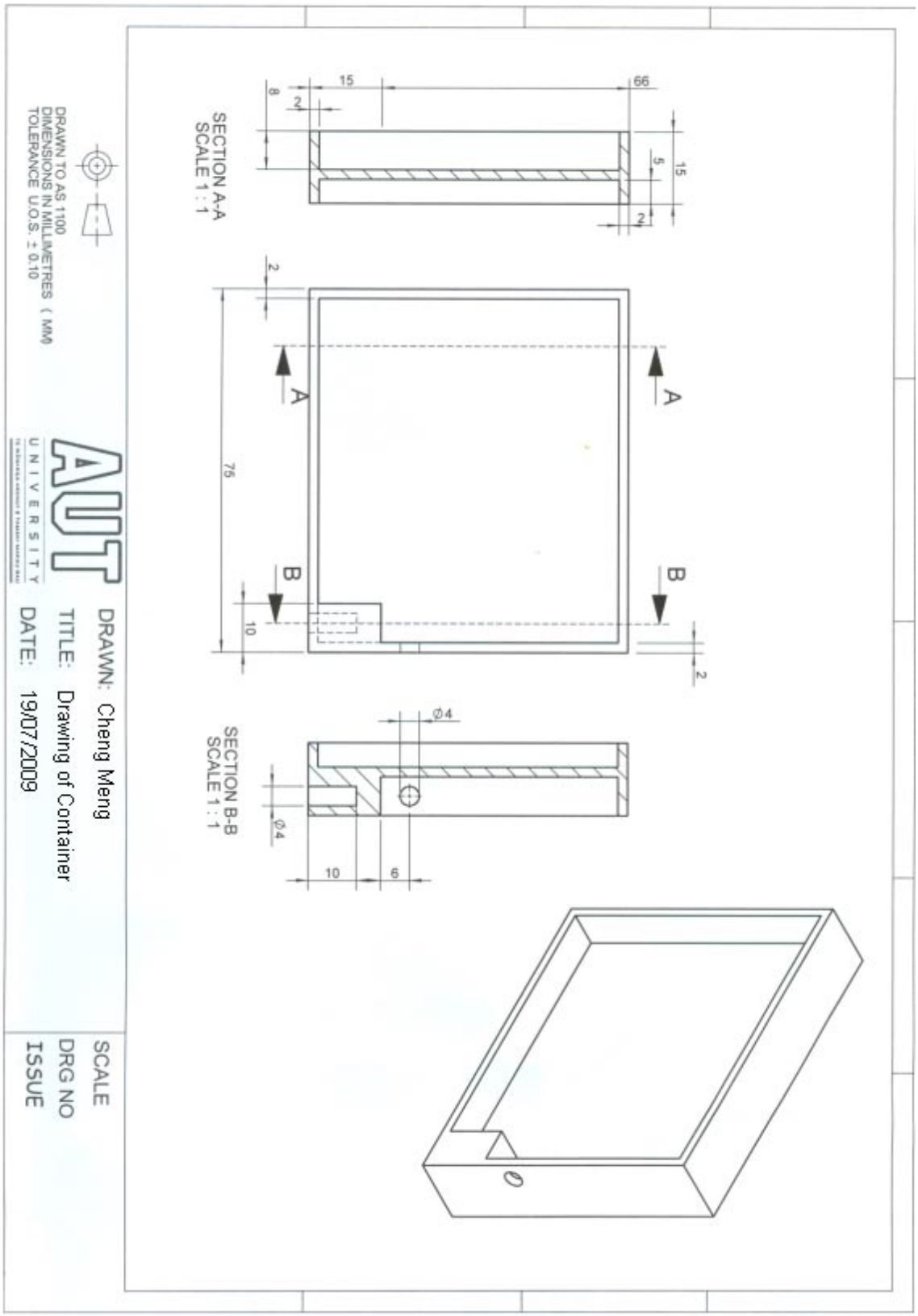

Appendix D: Drawing of Tensile Test Sample

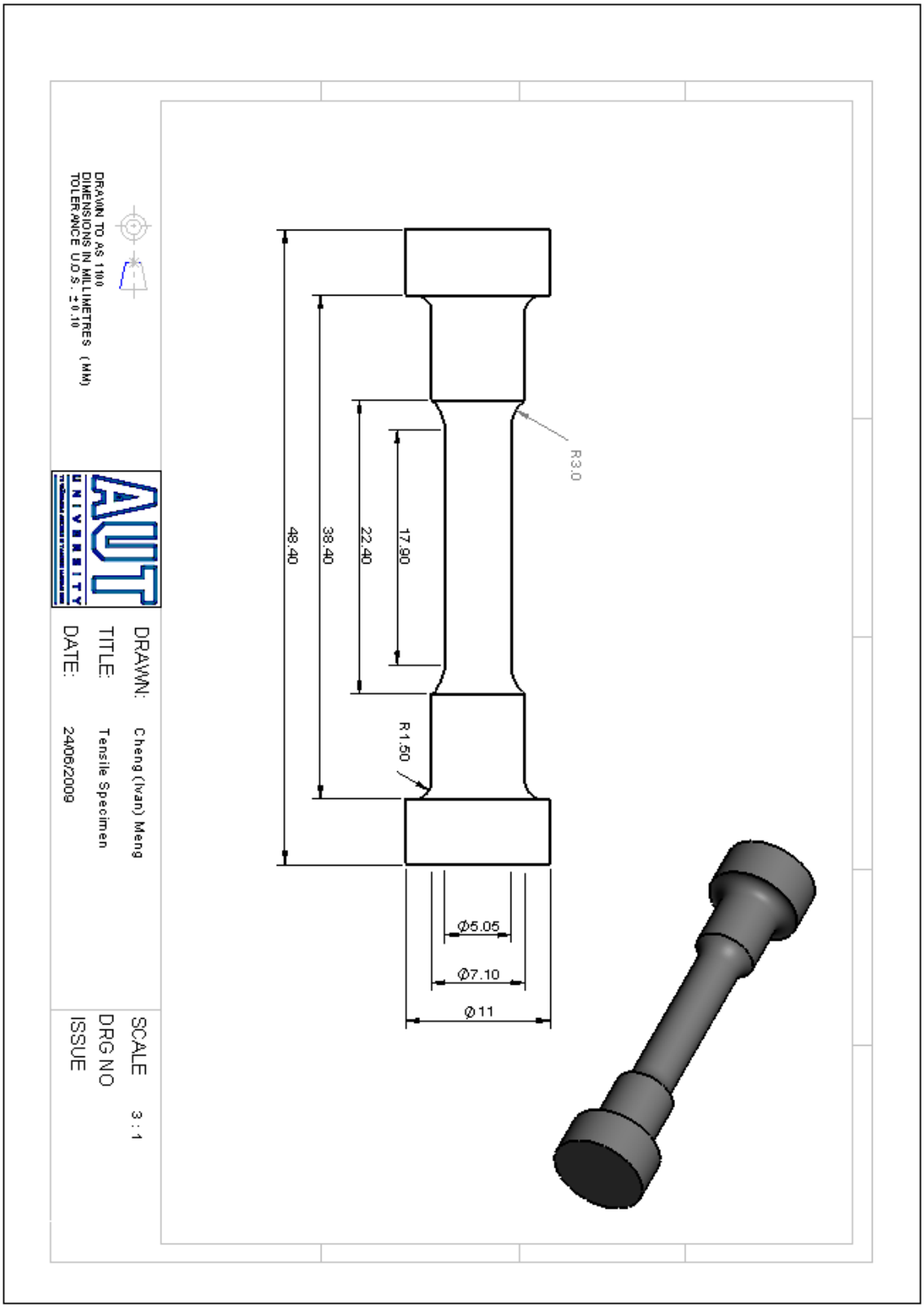

Appendix E: Drawing of Gleeble Test Sample

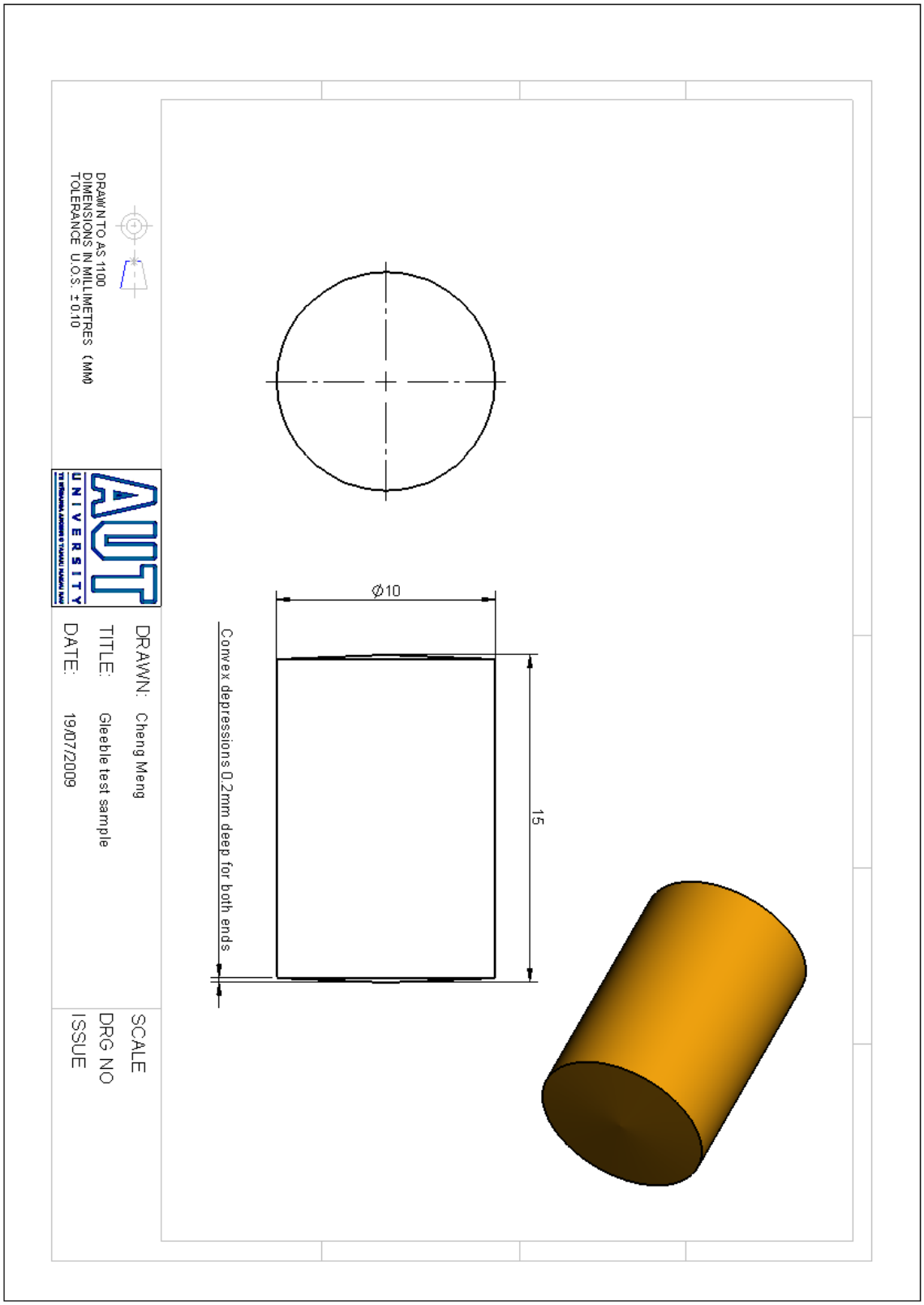

Appendix F: Heating Profiles

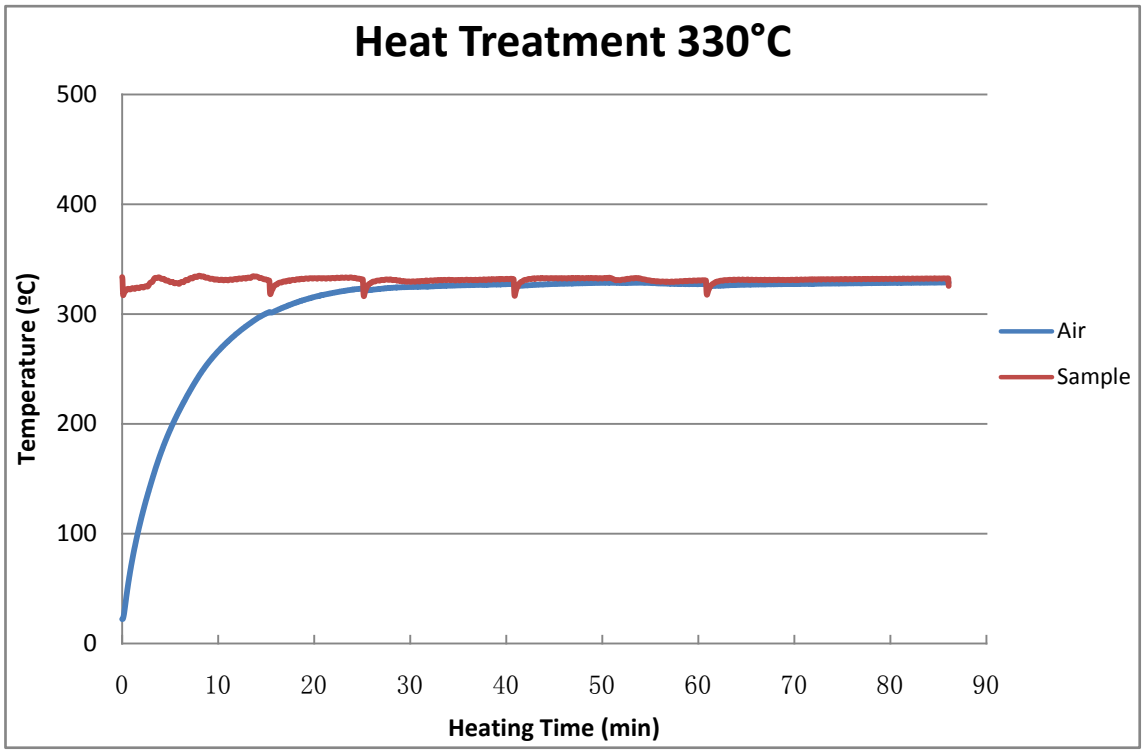

Figure 7.1: Heating Profiles of 330°C

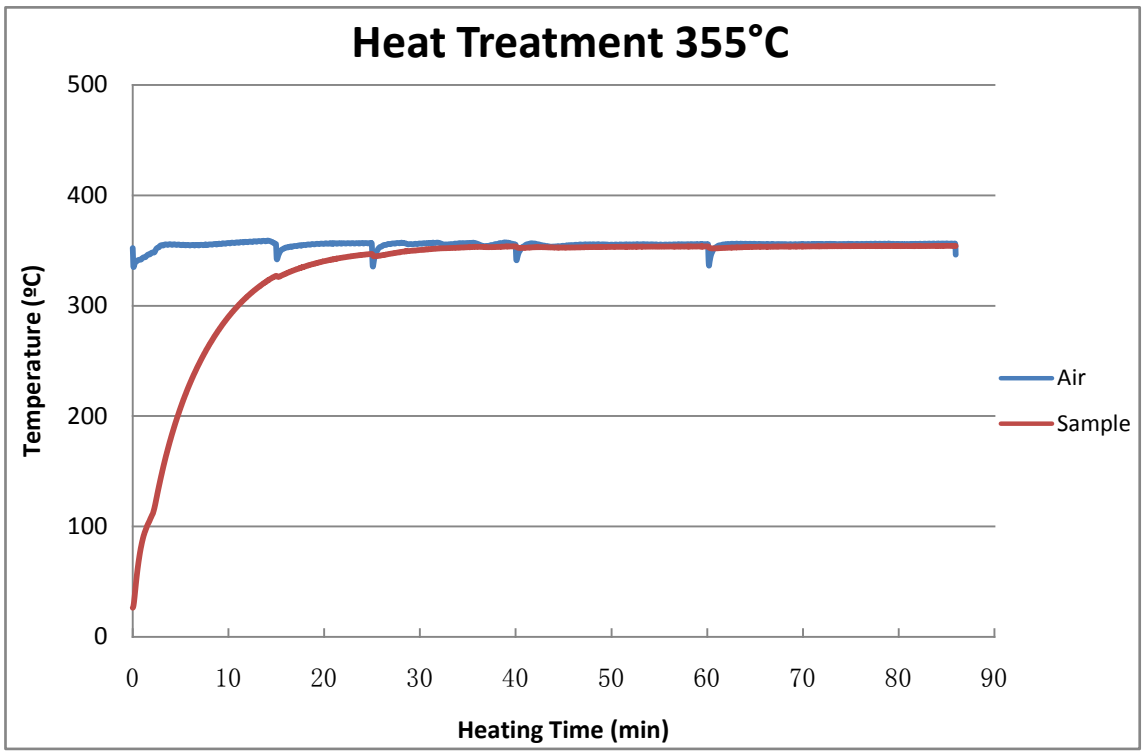

Figure 7.2: Heating profiles of 355°C

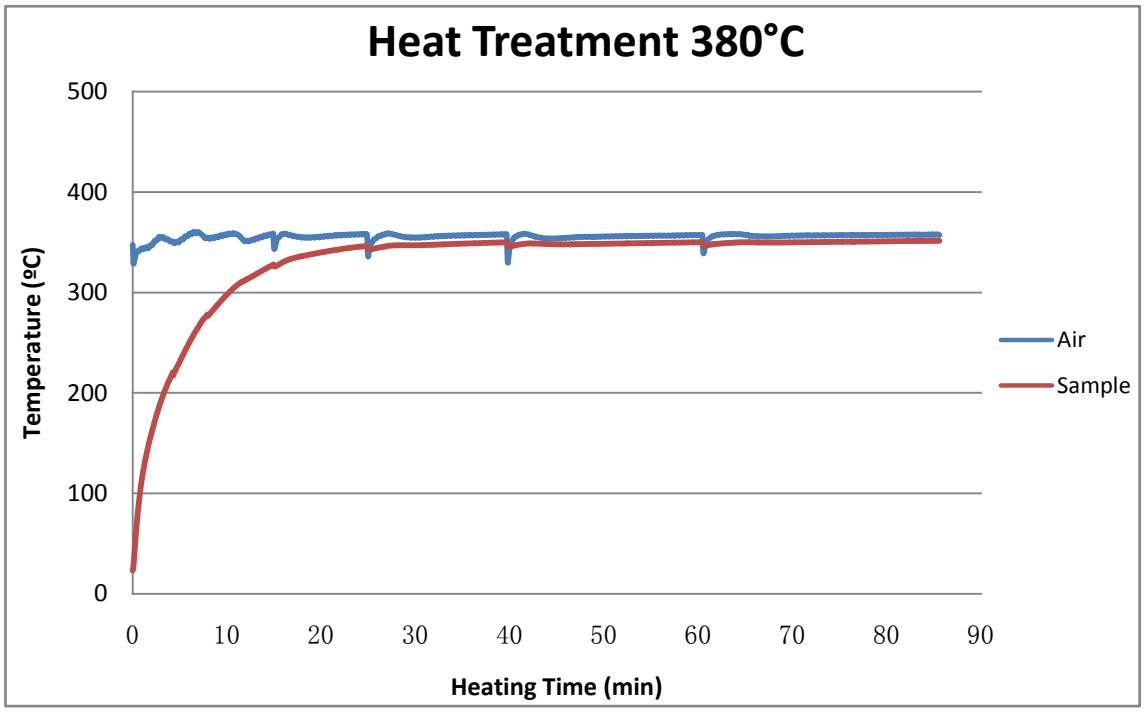

Figure 7.3: Heating profiles of 380°C

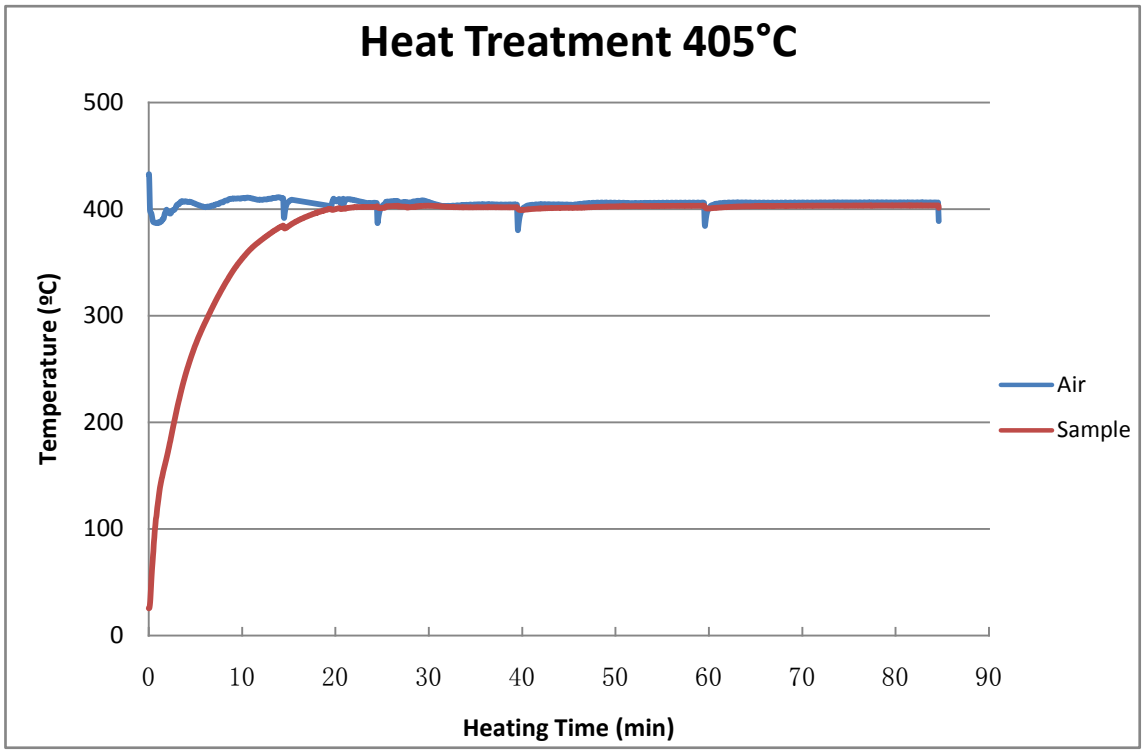

Figure 7.4: Heating profiles of 405°C

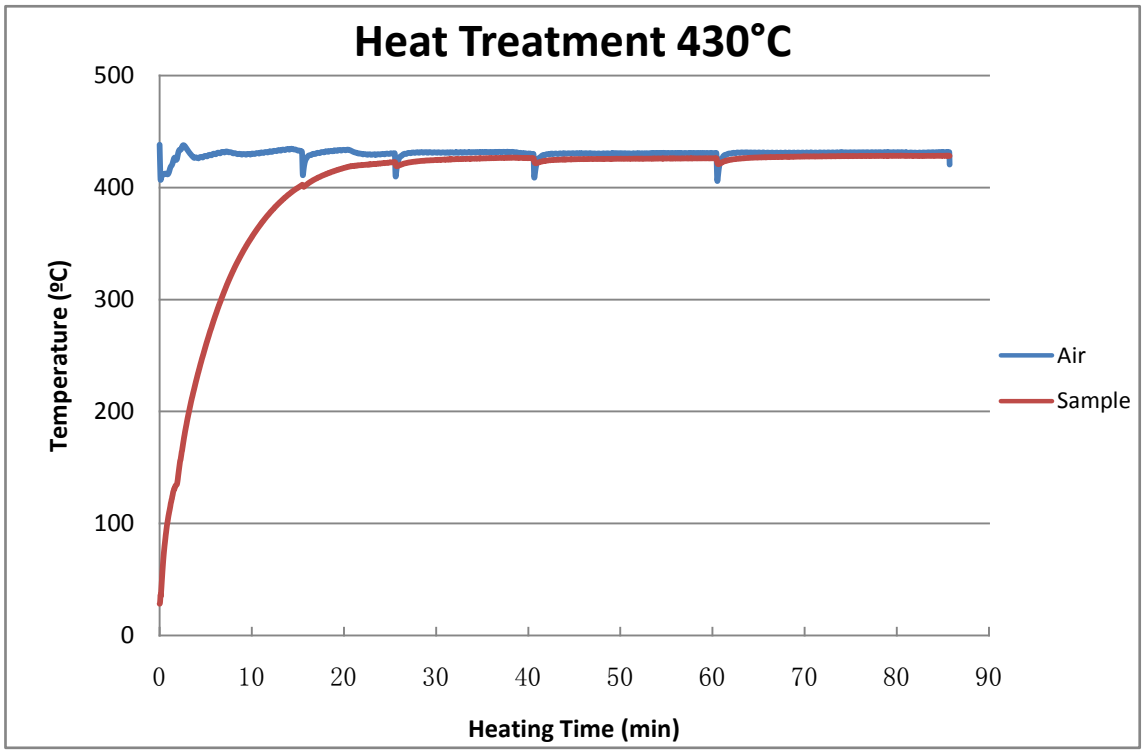

Figure 7.5: Heating profiles of 430°C

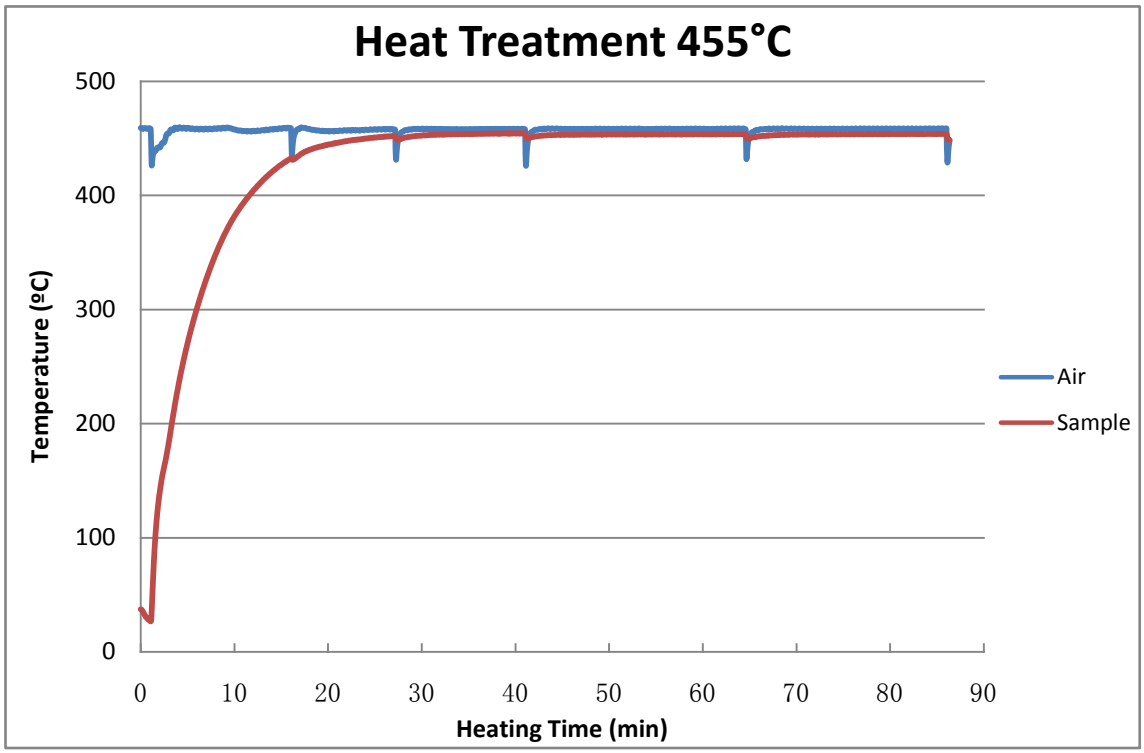

Figure 7.6: Heating profiles of 455°C

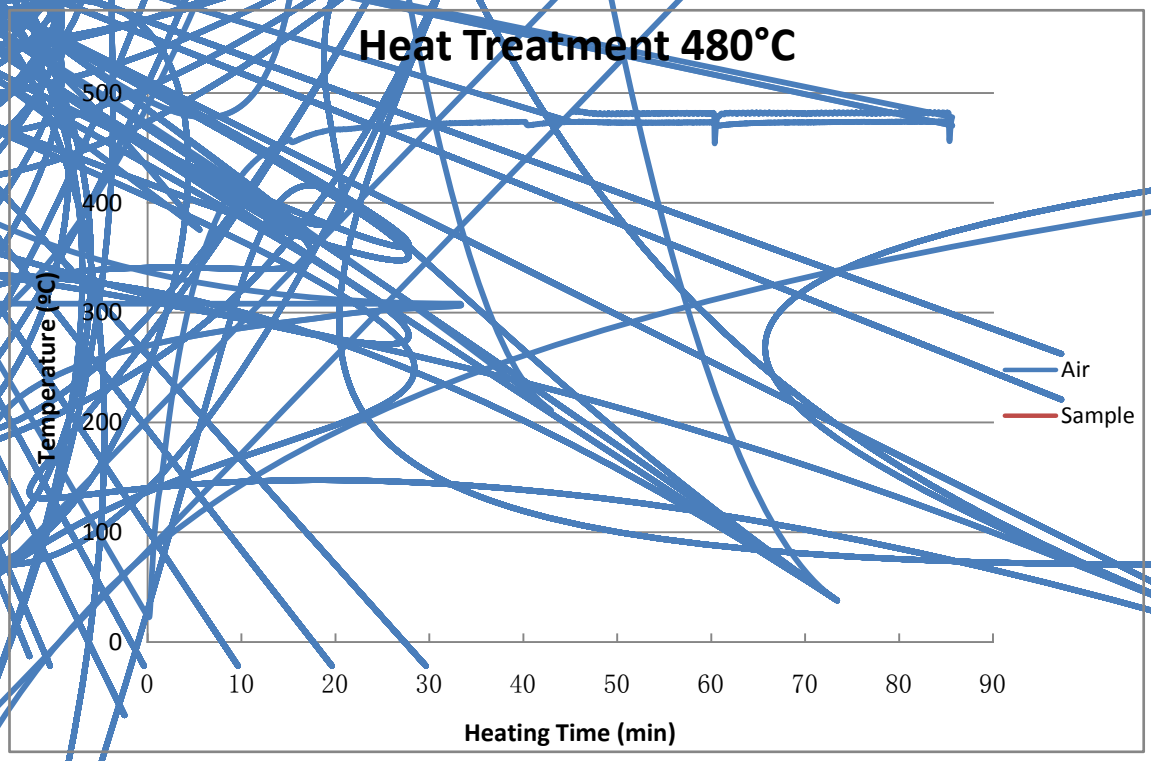

Figure 7.7: Heating profiles of 480°C

Appendix G: Hardness Test Result

Table 7.4: Hardness Test for AA6060 Hydro (Unit: HV)

Temperature	15 mins	25 mins	40 mins	60 mins	85 mins
330°C	44.88	41.41	38.95	36.03	37.93
355°C	40.43	37.60	36.75	34.83	34.49
380°C	37.57	37.45	35.45	33.55	34.63
405°C	40.70	40.60	36.10	33.20	32.60
430°C	42.07	41.53	38.01	38.60	37.08
455°C	39.13	39.79	41.84	41.48	42.48
480°C	43.00	46.30	43.70	49.20	50.20

Table 7.5: Hardness Test for AA6060 RTA (Unit: HV)

Temperature	15 mins	25 mins	40 mins	60 mins	85 mins
330°C	44.60	42.60	41.85	40.79	41.45
355°C	43.82	39.44	38.67	38.09	37.93
380°C	37.47	38.33	37.84	36.85	35.69
405°C	42.00	41.50	36.20	35.10	33.50
430°C	43.33	41.92	38.64	38.25	38.77
455°C	40.89	39.50	43.50	41.73	41.96
480°C	43.90	44.30	46.90	44.50	49.10

Appendix H: Tensile Test Result

Table 7.6: Yield strength for AA6060 Hydro (Unit: MPa)

Temperature	15 mins	25 mins	40 mins	60 mins	85 mins
330°C	62	56	53	48.5	48
355°C	55	52	44	38	40
380°C	52	42	39	35	34
405°C	49	45	41	32	32
430°C	50	47	42	41	40
455°C	54	52	55	53	51
480°C	58	64	65	65	68

Table 7.7: Yield strength for AA6060 RTA (Unit: MPa)

Temperature	15 mins	25 mins	40 mins	60 mins	85 mins
330°C	60	57	55	54	49
355°C	58	52	44	39	41
380°C	52	43	39	37	34
405°C	48	45	42	33	30
430°C	50	47	42	41	39
455°C	55	52	56	53	52
480°C	58	65	65	63	68

Table 7.8: Ultimate tensile strength for AA6060 Hydro (Unit: MPa)

Temperature	15 mins	25 mins	40 mins	60 mins	85 mins
330°C	126	131	123	122	118
355°C	131	122	120	118	114
380°C	124	125	122	116	111
405°C	127	133	123	113	112
430°C	140	136	127	126	125
455°C	148	150	137	147	149
480°C	155	167	169	170	169

Table 7.9: Ultimate tensile strength for AA6060 RTA (Unit: MPa)

Temperature	15 mins	25 mins	40 mins	60 mins	85 mins
330°C	138	123	126	122	118
355°C	131	122	120	119	114
380°C	124	124	122	116	111
405°C	120	133	122	113	111
430°C	139	136	127	126	124
455°C	148	150	137	148	149
480°C	155	167	168	169	169

Table 7.10: n value for AA6060 Hydro

Temperature	15 mins	25 mins	40 mins	60 mins	85 mins
330°C	0.25	0.23	0.22	0.25	0.28
355°C	0.21	0.22	0.29	0.27	0.31
380°C	0.28	0.32	0.33	0.33	0.34
405°C	0.28	0.33	0.32	0.36	0.36
430°C	0.32	0.33	0.33	0.34	0.34
455°C	0.32	0.33	0.3	0.32	0.33
480°C	0.31	0.31	0.32	0.31	0.29

Table 7.11: n value for AA6060 RTA

Temperature	15 mins	25 mins	40 mins	60 mins	85 mins
330°C	0.27	0.23	0.21	0.23	0.22
355°C	0.22	0.24	0.27	0.28	0.29
380°C	0.25	0.25	0.26	0.31	0.32
405°C	0.29	0.31	0.33	0.32	0.33
430°C	0.34	0.33	0.36	0.35	0.37
455°C	0.33	0.32	0.32	0.32	0.32
480°C	0.34	0.33	0.34	0.33	0.34

Appendix I: Hot Compression (Gleeble)Test Result

Table 7.12: Initial flow stress for AA6060 RTA (Unit: MPa)

Temperature	15 mins	25 mins	40 mins	60 mins	85 mins
330	39	38	48	42	45
355	38	34	40	41	32
380	40	38	36	35	37
405	35	36	34	35	33
430	25	25	25	26	25
455	20	20	20	22	25
480	25	20	18	24	22

Table 7.13: Peak flow stress for AA6060 RTA (Unit: MPa)

Temperature	15 mins	25 mins	40 mins	60 mins	85 mins
330°C	81	85	84	82	79
355°C	71	70	70	69	68
380°C	65	65	65	63	61
405°C	57	56	56	53	51
430°C	49	49	49	47	47
455°C	42	44	43	43	44
480°C	38	38	38	38	38

Table 7.14: Ln Z for AA6060 RTA

Temperature	15 mins	25 mins	40 mins	60 mins	85 mins
330°C	27	28	27	27	27
355°C	26	26	26	26	26
380°C	25	25	25	25	25
405°C	24	24	24	24	24
430°C	23	23	23	23	23
455°C	23	23	23	23	23
480°C	22	22	22	22	22

Appendix J: Matlab Code for Q, A and n Values Calculation

Iterative software code written by Joseph Robson [81] that uses the Nelder-Mead method to find constants (Q A n) which minimized error between the data and the Zener Hollomon equation is presented below.

```
Q A n = 132717.521541689      290105986.278240  2.61183792337889
```

```
clear all
clc
% Z = sr * exp(Q/RT) = A(sinh(alpha * s))^n
% where T is temperature (K), R is the gas constant (8.314), sr is the
strain rate, s is the strain. Q (activation energy), alpha, and n are
all constants and the instructions here describe how to find these by
fitting to your data.
% The instructions below show how to use the built in Matlab function
fminsearch to find the best fit for the constants for your data. Each
test you have done will have produced a flow curve (of stress vs.
strain) for one temperature and strain rate. You first need to
determine the flow stress of the material - this is the average stress
when the stress/strain curve flattens out (after the initial increase
in flow stress with strain). The temperature should be the average
thermocouple measurement (in Kelvin!) and you also need the strain
rate.
% Define the temperature for each test. For example, for 12 tests,
there would be 12 temperature values in "xdata"
xdata = [603 628 653 678 703 728 753];  %Temperature (K)
% Define the strain rates for each of the test, which must be in the
same order as the temperature data. If all your strain rates are the
same (which I think they may be) then the fitting might not work, but
it is still worth trying.
ydata = [2 2 2 2 2 2 2];                %Strain-rate (/s)
% Define the flow stress for each test, which must also be in the same
order.  This  flow  stress  you  must  work  out  from  plotting  the
stress/strain curves for each test as explained above.
zdata = [82.824 69.99   63.86   54.664  47.992  43.164  37.97]; %Flow
stress (MPa)
% Once you have defined the data, type the
data=[xdata;ydata];                         %Merges x and y data sets.
a0 = [145000 2.409e8 3.55];                  %Initialises values of the
constants.
options=optimset('Display','iter');             %Sets the options for
fminsearch
a = fminsearch(@stress,a0,options,data,zdata);  %Finds the new values
of the constants.
```

stress equation

```
function sse = stress(a,data,Actual_Data)
T=data(1,:);
sr=data(2,:);
Q = a(1);
R = 8.314;
A = a(2);
n = a(3);
Alpha = 0.045; %This is fixed for this analysis.
Z = sr.*exp(Q./(R.*T));
x = ((Z/A).^(1/n));
```

```
F = (1/Alpha)*log(x+sqrt(x.^2 + 1));
Error_Vector = F - Actual_Data;
% When curvefitting, a typical quantity to
% minimize is the sum of squares error
sse=sum(Error_Vector.^2);
```

Appendix K: Extrusion Processing

Please see the following page

Table 7.15: Profile Billet Transactions

REFERENCES

1. Lassance, D., Modeling of damage mechanisms in AlMgSi alloys - Understanding the role of homogenization on the extrudability. 2006, University Catholique De Louvain.
2. Schikorra, M., et al., Microstructure analysis of aluminum extrusion: Prediction of microstructure on AA6060 alloy. Journal of Materials Processing Technology, 2007. 201(1-3): p. 156-162.
3. Cai, M., D.P. Field, and G.W. Lorimer, A systematic comparison of static and dunamic aging of two Al-Mg-Si alloys. Mater Sci Eng, 2004: p. 64-71.
4. Marioara, C.D., et al., The influence of temperature and storage time at RT on nucleation of the β'' phase in a 6085 Al-Mg-Si alloy. Acta Materialia, 2001. 51(3): p. 798.
5. Sheppard, T., Extrusion of Aluminum Alloys. 1999: Kluwer Academic Publishers.
6. Traenker, F.O. Proc.2nd Int. Aluminum Extrusion Technology Seminar. 1. 1977.
7. Al-Marahleh, G., Effect of Heat Treatment Parameters on Distribution and Volume Fraction of Mg_2Si in the Structural Al 6063 Alloy. American Journal of Applied Sciences 3, 2006. 5: p. 1819-1823.
8. Joly, P., Y. Meyzaud, and A. Pineau, In advances in local fracture/damage models for the analysis of engineering problem. AMD, 1999. 137(ASME): p. 151.
9. Usta, M., The influence of thermal treatment on the cast structure of 6xxx aluminium alloys. 2001, Rensselaer Polytechnic Institute: Troy, New York.
10. Peris, R.G., Effects of extrusion conditions on :Die Pick-up" formed during extrusion of aluminium alloy AA6060. 2007, Auckland University of Technology: Auckland.
11. Sheppard, T., Structural changes occurring during thermal treatments during extrusion of Al-Cu-Mg-Mn-Si (AA2014) alloys. Metals Technology, 1982. 9: p. 398-399.
12. Resio, O., The effect of billet pre-heating practice on extrudability of AlMgSi alloys. 1988.
13. Nowotnik, G.M., J. Sieniawski, and M. Wierzbinska, Analysis of intermetallic particles in AlSi1MgMn aluminium alloys. Journal of achievements in materials and manufacturing engineering, 2007. 20: p. 155-158.
14. Lassance, D., et al., Micromechanics of room and high temperature fracture in 6xxx Al alloys. Progress in materials science, 2007. 52: p. 62-129.
15. Urreta, S.E., F. Louchet, and A. Ghilarducci, Fracture behaviour of an Al-Mg-Si alloy. Materials Science and Engineering, 2001. A302: p. 300-307.
16. Rashid, M., Mathematical Modeling and Opimization of Precipitation Hardening of Extrudable Aluminum Alloys. 1997, King Fahd University of Petroleum & Minerals: Dhahran, Saudi Arabia.
17. Kwon, Y.N., Y.S.L., and J.H. Lee, Deformation bahavior of Al-Mg-Si alloy at the elevated temperature. Journal of Materials Processing Technology, 2007: p. 533-536.

18. Wright, R.N., Practical Engineering for Aluminum Extrusion Note. 1992, Rensselaer Ploytechnic Institute: Troy, New York.
19. Wade, K.D., Physical meallurgy of aluminium alloys. Engineering Fundamentals of Aluminium Extrusion, 1993.
20. Altenpohl, D., Aluminium and aluminium alloys. 1982: Aluminium-Verlag GmbH, Konigsallee 30, P.O.B. 1207, D-4000 Dusseldorf 1, FRG. 223.
21. Dieter, G.E., Mechanical metallurgy. 3rd edn ed. 1986: McGraw-Hill, New York. 325.
22. Huis, M.A.v., et al., Phase stability and structural relations of nanometer-sized, matrix-embedded precipitate phases in Al-Mg-Si alloys in the late stages of evolution. Acta Materialia, 2006. 54: p. 2945-2955.
23. Hulley, S.I. and G.W. Lorimer. The effect of dispersoids on the recrystallization behavior of a series of Al-Mg-Si alloy. in The 3rd International Conference on Aluminium Alloys. 1992.
24. Edwards, G.A., et al., The precipitation sequence in Al–Mg–Si alloys. Acta Materialia, 1998. 46: p. 3893-3904.
25. Murayama, M. and K. Hono, Pre-precipitate clusters and precipitation processes in Al–Mg–Si alloys. Acta Materialia, 1999. 47(5): p. 1537-1549.
26. Derlet, P.M., et al., A first-principles study of the β''-phase in Al-Mg-Si alloys. Condens, Matter, 2002. 14: p. 4011-4024.
27. Andersen, S.J. and R. Hoier, Overview of the precipitation sequence in a 6082 aluminium alloy, A TEM study of the precipitates in a 6082 Al-Mg-Si alloy system. 2001, NTNU.
28. Langkruis, J.V.d., et al., The effect of β, β', β'' precipitates in a homogenised AA6063 alloy on the hot deformability and the peak hardness. 2001. A299: p. 105 - 115.
29. Zajac, S., et al., Optimisation of Mg_2Si phase for extrudability of AA6063 and AA6005 alloys. Materials Science Forum, 1996. 217-222: p. 397-402.
30. Myhr, O.R., et al., Modelling of the microstructure and strength evolution in Al-Mg-Si alloys during multistage thermal processing. Acta Materialia, 2004. 52: p. 4997-5008.
31. William, D. and J.R. Callister, Materials Science and Engineering An Introduction. Sixth ed. 2003.
32. Garrett, R.P., J. Lin, and T.A. Dean, An investigation of the effects of solution heat treatment on mechanical properties for AA6xxx alloys: experimentation and modelling. International Journal of Plasticity, 2004. 21: p. 1640-1657.
33. Courtney, T.H., Mechanical behavior of materials McGraw-Hill Series in materials science and engineering, 1990. 18: p. 710.
34. Yassar, R.S., Characterization and modeling of dislocation-precipitation interactions in aluminium alloys, in School of Mechanical & Materials Engineering. 2005, Washington State University: Washington DC.
35. Honeycombe, R.W.K., The plastic deformation of meatals. Edward Arnold, 1984.
36. Glicksman, M., Diffusion in solids. John Wiley & Sons, Inc. New York, 2000.
37. McLean, M., Microstructural instabilities in metallurgical systems - a review. Metal Science, 1978. 12: p. 489-497.
38. Lyman, T., Metals Handbook. 1948: ASM International, Materials Park, Ohio. 1246.

39. Ricks, R.A., et al. Microstructural optimisation for extrusion of 6063 alloys. in Proceedings of the fifth international aluminium extrusion technology seminar. 1992. Chicago, Illinois, U.S.A.
40. Zajac, S., B. Bengtsson, and C. Jonsson, Influence of cooling after homogenization and reheating to extrusion on extrudability and final properties of AA6063 and AA6082 alloys. Materials Science Forum, 2002. 396-402: p. 399-404.
41. Nowotnik, G.M. and J. Sieniawski, Influence of heat treatment on the microstructure and mechanical properties of 6005 and 6082 aluminium alloys. J. Maer. Process. Technol, 2005. 162-163: p. 367-372.
42. Shercliff, H.R. and M.F. Ashby, A process model for age-hardening aluminium alloys: Part II: Applications. Acta metall. mater., 1990. 38(10): p. 1789-1802.
43. Cáceres, C.H., I.L. Svensson, and J.A. Taylor. Microstructural Factors and the Mechanical Performance of Al-Si-Mg and Al-Si-Cu-Mg Casting Alloys. in Invited Presentation to the 2nd International Aluminum Casting Technology Symposium ASM's Materials Solutions Conference 2002. Columbus, Ohio, Oct.
44. Polmear, I.J., Light alloys - Metallurgy of the lighe metals. Third ed. 1995, Arnold, London. 26.
45. Zhang, D.L. and L. Zheng, The quench sensitivity of cast Al-7 wt pct Si-0.4 wt pct Mg alloy. Met. Mater. Trans., 1996. A(27): p. 3983-3991.
46. Cáceres, C.H., et al., Hypoeutectic Al-Si-Mg foundry alloys. Materials Forum, 1997. 21: p. 27-43.
47. Rometsch, P.A. and G.B. Schaffer, An age hardening model for Al-7Si-Mg casting alloys. Materials Science and Engineering, 2001. A(325): p. 424-434.
48. Burger, G.B., et al., Microstructural control of aluminum sheet used in automotive applications. Materials Characterization, 1995. 35(1): p. 23-29.
49. Lloyd, A.J. Precipitation metals. in Proceeding of the 7th Int Conf on the Strength of Metal and Alloys. 1985. I.C.S.M.A. -7, Montreal, Canada: Oxford: Pergamon Press.
50. Esmaeili, S., D.J. Lloyd, and W.J. Poole, A yield strength model for the Al-Mg-Si-Cu alloy AA6111. Acta metall, 2003. 51: p. 2243-2257.
51. Shen, Y.L. and N. Chawla, On the correlation between hardness and tensile strength in particle reinforced metal matrix composites. Materials Science and Engineering, 2001. A(297): p. 44-47.
52. Meyers, M.A. and K.K. Chawla, Mechanical behavior of materials. 1999. 160.
53. George, E. and J.R. Dieter, Mechanical Metallurgy. Metallurgy and Metallurgical Engineering. 1961, Philadelphia: McGRAW-HILL Book Company, INC.
54. Cai, X. and P.N. Zhou, Influence of elastic recovery on microindentation hardness - a finite element analysis. Scripta Metallurgica et Materialia, 1992. 27: p. 347-352.
55. Oliver, W.C. and G.M. Pharr, An improved technique for determining hardness and elastic modulus using load and displacement sensing indentation experiments. Materials Research Society, 1992. 7(6): p. 1564-1583.
56. Hong, S.I., G.T.G. Ill, and Z. Wang, Microstructure and stress-strain responses of Al-Mg-Si alloy matrix composites reinforced with 10vol% Al_2O_3 particulates. Mater Sci Eng, 1996. A(221): p. 38-47.
57. 646-78, A.E., Standard test method for tensile strain-hardening exponent (n value) of metallic sheet materials. Annual book of ASTM standards. Vol. 03. 1989, Philadelphia.

58. Hatch, E.J., Aluminum: Properties and Physical Metallurgy. 1984: American Society For Metals.
59. Zajac, S., B. Hutchinson, and L.-O. Gullman, Microstructure control and extrudability of Al-Mg-Si alloys microalloyed with manganese Materials science and Technology, 1994(10): p. 323-333.
60. Arentoft, M., et al., Physical and mathematical modelling of extrusion processes. Journal of Materials Processing Technology, 2000. 106: p. 2-7.
61. Friis, J., et al., Work hardening behaviour of heat treatable Al-Mg-Si alloys. Materials Science Forum, 2006. 519-521: p. 1901-1906.
62. ASM Handbook. 1, 2, 8, 10th edn. ed: ASM Interinational, Materials Park, OH.
63. Tiryakioglu, M., J. Campbell, and J.T. Staley, On macrohardness testing of Al–7 wt.% Si–Mg alloys II. An evaluation of models for hardness–yield strength relationships. Materials Science and Engineering A361, 2003(A361): p. 240–248.
64. Herba, E.M., Influence of particulate reinforcements on 6061 materials inextrusion modeling. Materials Science and Engineering, 2002. A(372).
65. Sellars, C.M., Thermomechanical processing of aluminium alloys, in International summer school on aluminium alloy technology. 1991: Trondheim.
66. Zhang, H., et al., Hot deformation behavior of the new Al-Mg-Si-Cu aluminium alloy during compression at elevated temperature. Mater Charact, 2007. A(379): p. 321-326.
67. Sellars, C.M., W.J. Tegart, and G. MC, Hot Workability Metall. Rev, 1972. 17(158): p. 1-24.
68. McQueen, H.J. and M.J. Lee, Light metals 2000 In: J. Kazadi et al. (Eds.). Met. Soc. CIM, Montreal, 2000: p. 529-538.
69. Velay, X., Prediction and control of subgrain size in the hot extrusion of aluminium alloys with feeder plates. Journal of Materials Processing Technology, 2008.
70. Verlinden, B., A. Suhadi, and L. Delaey, Effect of the heat treatment on the hot deformation behaviour of an AA6060. Scr. Met. Mat, 1993. 28: p. 1441-1446.
71. Xiaoxin, X., et al., Hot deformation mechanisms in a 1- vol% Al2O3 particle reinforced 6061 Al matrix composite. Scripta Metallurgical et Materialia, 1995. 32(8): p. 1195-1190.
72. Nengping, J., et al., Hot deformation behavior of 7150 aluminium alloy during compression at elevated temperature. Materials Characterization, 2008. 60: p. 530-536.
73. He, H., et al., Deformation behavior and microstructure evolution of 7050 aluminium alloy during high temperature deformation. Mater Sci Eng, 2008. A(488): p. 64-71.
74. Yu, D. and T. Chandra, TMS, Warrendale, PA. in Advanced Composites ’93, T. Chandra, A.K. Dhingra, eds. 1993: p. 1070-1077.
75. Langkruis, J.V.d., W.H. Kool, and S.V.d. Zwaag, Assessment of constitutive equations in modeling the hot deformability of some averaged Al - Mg - Si alloys with varying solute contents. Mater Sci Eng, A struct Mater: Prop Microstruct Process. 1999(266): p. 135-145.
76. Clode, M.P. and T. Sheppard, Formation of die lines during extrusion of AA6063. Materials Science and Technology, 1990. 6(8): p. 755-763.
77. Feltham, P., Metal treatment. Vol. 23. 1956. 440.

78. Tutcher, M.G., Deformation processing applied to the Al-Mg alloy system. 1979, University of London.
79. Völkl, I.R. Werkstoffprüfung. [cited; Available from: http://www.metalle.uni-bayreuth.de/de/research/material_testing/index.html.
80. Spigarelli, S., E. Evangelista, and H.J. McQueen, Study of hot workability of a heat treated AA6082 aluminum alloy. Scr Mater. 2003(49): p. 179-183.
81. Robson, J., Microstructural Evolution in Aluminium Alloy 7050 During Processing. Materials Science and Engineering A, 2004. 382: p. 112.
82. Tabor, D. and P.R. Soc, A simple theory of static and dynamic hardness. London Sect., 1948. A(192): p. 247.
83. J. R. Cahoon, W.H.B., A. R. Kutzak, The determination of yield strength from hardness measurements Metallurgical and Materials Transactions B, 1970. 2(7): p. 1979-1983.
84. Roger, N.W., A modern view of the thermodynamics and kinetics of the magnusium silicide presence in 6xxx alloys. Matin Usta, 2000: p. 67-75.
85. Myhr OR, G.O., Andersen SJ, Modelling of the age hardening behaviour of Al-Mg-Si alloys. Acta Materialia, 2001. 49(1): p. 65-75.
86. L.P. Borrego, L.M.A., J.M. Costa, J.M. Ferreira, Analysis of low cycle fatigue in AlMgSi aluminium alloys. Engineering Failure Analysis, 2004. 11: p. 715-725.
87. Chen, X., The effect of extrusion conditions on yield strength of AA6060 aluminium alloys. 2008, Auckland University of Technology: Auckland, New Zealand.
88. Jesper Friis, B.H., Oyvind Ryen, Erik Nes, Ole R. Myhr, Work hardening behaviour of heat treatable Al-Mg-Si alloys. Materials Science Forum, 2006. 519-521: p. 1901-1906.
89. Langkruis, J.v.d., et al., Modelling Mg_2Si dissolution in an AA6063 alloy dring pre-heating to the extrusion temperature. Lab. for Materials Science, 2000.
90. Gubicza, J., et al., The effect of severe plastic deformation on precipitation in supersaturated Al-Zn-Mg alloys. Mater Sci Eng, 2007. A(461): p. 77-85.
91. Sakai, T. and C. Takahashi, Flow softening of 7075 aluminium alloy under hot compression. Mater Trans JIM, 1991. 32(375-382).
92. Nengping Jin, H.Z., Yi Han, Wenxiang Wu, Jianghua Chen, Hot deformation behavior of 7150 aluminium alloy during compression at elevated temperature. Materials Characterization, 2008. 60: p. 530-536.